Multiphase Fountains

Martin Conrad Lippert

University of Cambridge
BP Institute for Multiphase Flow
Department of Earth Sciences

This dissertation is submitted for the degree of

Doctor of Philosophy

Supervisor: Prof. A.W. Woods

St. John's College April 2020

Declaration

This thesis is the result of my own work and includes nothing which is the outcome of work done in collaboration except as declared in the Preface and specified in the text. It is not substantially the same as any that I have submitted, or, is being concurrently submitted for a degree or diploma or other qualification at the University of Cambridge or any other University or similar institution except as declared in the Preface and specified in the text. I further state that no substantial part of my thesis has already been submitted, or, is being concurrently submitted for any such degree, diploma or other qualification at the University of Cambridge or any other University or similar institution except as declared in the Preface and specified in the text. It does not exceed the prescribed word limit for the relevant Degree Committee.

Martin Conrad Lippert

April 2020

Multiphase Fountains

Martin Conrad Lippert

In this thesis we present experimental studies and theoretical models on the rise height and entrainment of axisymmetric multiphase fountains. The aim of this thesis is to improve our understanding of these fundamental flows frequently observed in industry and nature.

In each chapter we present a series of laboratory experiments and we employ various dye visualisations and imaging techniques to extract experimental data. This data is compared with theoretical models based on the conservation of volume, momentum and buoyancy fluxes. We focus our attention on the bulk dynamics of the flow rather than on the motion of individual bubbles or particles.

In chapters 2 and 3 we consider unconfined bubble fountains. We begin by investigating the maximum depth reached by bubbles in turbulent water jets issuing downwards into a reservoir. We compare the experimental data with a theoretical model based on the conservation of volume, momentum and buoyancy fluxes. We proceed in chapter 3 by investigating the depth reached by bubbles in low Reynolds number bubble fountains and we present a scaling for the maximum depth reached by bubbles in such flows. In the experiments we observed bubbles accumulating at the surface, forming a filling-box flow. This observation encouraged a subsequent investigation of filling-box flows of bubbles and particles in confined reservoirs.

In chapters 4 and 5 we consider turbulent fountains in confined environments. In chapter 4 we investigate the fate of particles carried into a confined space by a turbulent particle-laden fountain. We identify four distinct regimes by comparing the particle settling velocity with three characteristic velocities in the system. In the fifth chapter we focus our attention on extremely confined turbulent fountains. We measure the rise height and entrainment of fountains in very narrow tanks and identify the regime in which the fountain is affected by the confinement. We present a scaling argument for the entrainment of such flows.

In chapter 6 we consider the run-out length and entrainment of particle-driven gravity currents, fed by turbulent particle-laden fountains. We present a theoretical model accounting for the presence of a sedimentation front.

The thesis concludes with a summary and discussion of the findings in chapter 7.

Acknowledgements

It is with immense gratitude that I acknowledge the continuous support of my supervisor, Professor Andrew W. Woods, throughout this project. It has been a fantastic experience to undertake my PhD at the BP Institute and I would not hesitate to do it again.

I would also like to extend my appreciation to Dr. Charlotte Gladstone for her guidance, which has provided invaluable input into this project, as well as to Andrew Pluck for his support in setting up the experiments.

I am very grateful for the funding provided by the BP Institute for Multiphase Flow, an EPSRC Industrial Case award and the Benefactors' Scholarship of St. John's College Cambridge.

I have really enjoyed my four years at the BPI. It is a brilliant place, full of great people. In particular, I would like to make mention of Edward Hinton for his advice and for the many great discussions we have had.

Special thanks, of course, goes to Neeraja Bhamidipati. This PhD would not have been the same without her. I would like to thank her for her friendship and for the many great moments we have shared.

A big thank you also goes to the St. John's Crew, some of the best friends and house mates I could have hoped for: thank you to Iva Jugovic, Ryan Limbocker, J.R. Lalancette, Yehia Amar and Joseph McAbee. Even though never a house mate, this list would not be complete without mentioning Marc Oeller. All these people made Cambridge a very special place.

Finally, I would like to thank my parents, my brother, my girlfriend Kari Jackson, and my best friend Lukas Schmitz for their incredible support!

Abstract

In this thesis we present experimental studies and theoretical models on the rise height and entrainment of axisymmetric multiphase fountains. The aim of this thesis is to improve our understanding of these fundamental flows frequently observed in industry and nature.

In each chapter we present a series of laboratory experiments and we employ various dye visualisations and imaging techniques to extract experimental data. This data is compared with theoretical models based on the conservation of volume, momentum and buoyancy fluxes. We focus our attention on the bulk dynamics of the flow rather than on the motion of individual bubbles or particles.

In chapters 2 and 3 we consider unconfined bubble fountains. We begin by investigating the maximum depth reached by bubbles in turbulent water jets issuing downwards into a reservoir. We compare the experimental data with a theoretical model based on the conservation of volume, momentum and buoyancy fluxes. We proceed in chapter 3 by investigating the depth reached by bubbles in low Reynolds number bubble fountains and we present a scaling for the maximum depth reached by bubbles in such flows. In the experiments we observed bubbles accumulating at the surface, forming a filling-box flow. This observation encouraged a subsequent investigation of filling-box flows of bubbles and particles in confined reservoirs.

In chapters 4 and 5 we consider turbulent fountains in confined environments. In chapter 4 we investigate the fate of particles carried into a confined space by a turbulent particle-laden fountain. We identify four distinct regimes by comparing the particle settling velocity with three characteristic velocities in the system. In the fifth chapter we focus our attention on extremely confined turbulent fountains. We measure the rise height and entrainment of fountains in very narrow tanks and identify the regime in which the fountain is affected

by the confinement. We present a scaling argument for the entrainment of such flows.

In chapter 6 we consider the run-out length and entrainment of particle-driven gravity currents, fed by turbulent particle-laden fountains. We present a theoretical model accounting for the presence of a sedimentation front.

The thesis concludes with a summary and discussion of the findings in chapter 7.

Table of contents

Chapter 1

Introduction

1.1 Definition

A fountain is a localised fluid flow in which the momentum flux at the source is opposed by the buoyancy flux (Hunt and Burridge (2015)).

The most common association with the term *fountain* is a water feature in which a water jet is ejected upwards into air. The water is more dense compared to the air, so some initial momentum is required to overcome the negative buoyancy force associated with this density difference. In this specific example, the density difference between the fountain fluid (water) and the ambient fluid (air) is very large and the two fluids do not mix. The fountain fluid decelerates owing to its larger density until it eventually comes to rest at some height before collapsing and falling back down under the influence of gravity.

In many other examples of fountains, however, the fountain fluid and the ambient fluid are miscible and the density difference between the two fluids is small. An example of such a flow is often noticed in the entrance area of shopping centres where a hot jet of air is forced downwards to distribute warm air and provide heating. The warm air is less dense compared to the colder ambient air, so some initial momentum is required to overcome the buoyancy force associated with this density difference. In this example, both the fluid inside and outside the fountain is air and the relative density difference at the source is only a few percent, so that the fountain is free to entrain fluid from its environment. Owing to this entrainment, the volume flux within the

fountain increases several fold before the flow is arrested. Such a fountain flow decelerates owing to (i) the density difference between the fountain and the environment, and (ii) the entrainment of ambient fluid which has to be accelerated from rest.

The term *localised* in the definition of a fountain above refers to the fact that a fountain requires a well-defined, spatially confined source. This localisation is commonly expressed in terms of the source Froude number of the fountain, Fr_0, which corresponds to the ratio of inertial to gravitational forces,

$$Fr_0 = \frac{u_0}{\sqrt{g_0' b_0}}, \tag{1.1}$$

where u_0 is the velocity of the fountain fluid at the source, g_0' is the reduced gravitational acceleration at the source and b_0 is the radius of the source. For $Fr_0 > 1$ the flow may be referred to as localised. Fountains issuing from a round nozzle, as implied by the source radius b_0, are axisymmetric.

If the fountain fluid contains a second phase, it is commonly referred to as a multiphase fountain. This second phase could be bubbles, droplets, particles or other contaminants. These contaminants can be passive, in which case the buoyancy is provided solely by the interstitial fluid, or the contaminants provide or contribute to the density difference between the fountain and the environment. Bubbles, particles or other contaminants in the fountain may exhibit a slip velocity relative to the fountain fluid. If this slip velocity is small compared to the fluid velocity in the fountain, then the fountain behaves as an analogous single-phase fountain with the same source fluxes of buoyancy and momentum. If the slip velocity is comparable to, or even exceeds the fountain fluid velocity, the second phase separates from the fountain before the fountain fluid comes to rest (Mingotti and Woods, 2016).

The goal of this thesis is to improve our understanding of the rise height and the mixing of axisymmetric multiphase fountains.

1.2 Motivation and structure of thesis

Axisymmetric multiphase fountains are frequently observed in industry and nature. Improving our understanding of such flows can enable the optimisation

of industrial process equipment and the prediction of the effects of natural occurrences.

Figure 1.1 provides a high-level overview of the content covered in this thesis: Chapters 2 and 3 consider the rise height and entrainment of bubble fountains in unconfined environments. Chapters 4 and 5 consider the rise height and mixing of turbulent fountains in confined environments. Chapter 6 considers the mixing and transport of particles in sustained particle-driven gravity currents fed by particle-laden fountains.

Chapter 2: Turbulent bubble-laden fountains are frequently employed to aerate oxygen-scarce water in lakes or water treatment facilities (Biń, 1993; Neto et al., 2016). A good understanding of the depth reached by the bubbles and the entrainment of ambient fluid guides the development of such systems. To this end, the second chapter contains an experimental and theoretical investigation of the penetration depth of bubbles in turbulent bubble fountains in water. The model, based on a single entrainment parameter and a constant bubble rise speed, is in good agreement with the experimental data. This work has been published in the *Journal of Fluid Mechanics* in 2018.

Chapter 3: Bubbles introduced by bubble-laden fountains may also be highly undesirable when a contamination of the fluid is to be avoided. This effect is especially pronounced in viscous fluids as more time is required for bubbles to escape. The lubrication capabilities of engine oil for example deteriorate when bubbles are introduced by plunging oil jets. Aerated oil also exhibits compressibility effects which delay hydraulic activation of valves, leading to increased wear (Nemoto et al., 1997). The third chapter contains an exper-

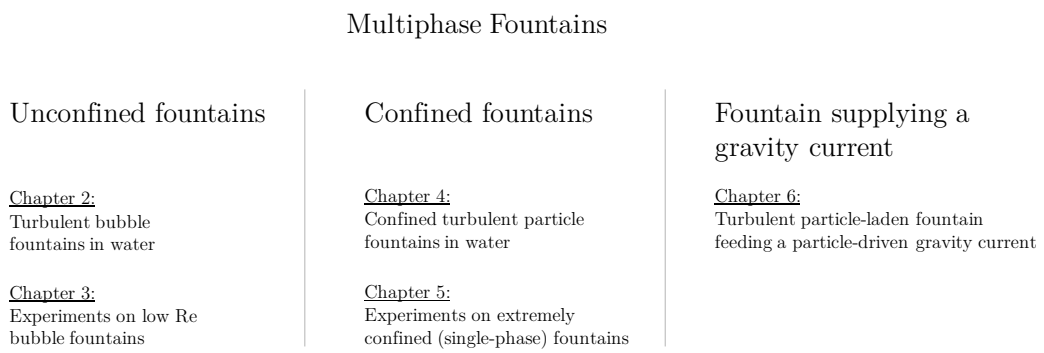

Fig. 1.1 Structure of this thesis.

imental investigation of low Reynolds number bubble fountains. We discuss experimental observations and present a scaling for the maximum penetration distance of the bubbles in oil-air fountains. Owing to the viscosity of the fluid, some bubbles do not have sufficient time to rise and escape but instead accumulate at the free surface and form a bubble-rich layer growing downwards into the tank. This observation motivated a detailed investigation of multiphase fountains in confined and contaminated environments.

Chapter 4: Particle-laden fountains are frequently generated by ventilation systems distributing pathogens and particles through a building. It is important to understand the bulk motion of contaminates in such particle-laden fountains to ensure adequate air quality especially in clean rooms and hospitals (Linden, 1999; Mingotti and Woods, 2015a,b). In fluidised bed reactors particle fountains may suspend a particle bed up to some height, and multiphase fountains are also employed in filter systems to separate particles by size and weight (Mingotti and Woods, 2016; Rowe and Nienow, 1976). The fourth chapter contains an analysis of the transport of particles supplied to a confined environment as a particle-laden fountain. By comparing the terminal particle settling velocity with three characteristic flow velocities in the system, we identify four distinct regimes that determine the height of the contaminated layer as well as the adjusted fountain height. This chapter has been published in the *Journal of Fluid Mechanics* in 2018.

Chapter 5: The fifth chapter presents an experimental investigation of the rise height and entrainment of turbulent fountains in extremely narrow tanks. We find that both the rise height and the total entrainment of ambient fluid into the fountain decrease compared to an equivalent unconfined fountain if the ratio of confinement width and fountain diameter falls below a threshold value of 2. We present a scaling argument for the entrainment of ambient fluid by very confined fountains.

Chapter 6: Particle-laden fountains feeding particle-driven gravity currents are featured in a wide range of industrial process equipment. Separators are frequently employed in water treatment facilities or the oil and gas industry to separate sand and contaminants from water or oil. At the inflow, the particle-laden flow forms a multiphase fountain, feeding a multiphase gravity

current. The properties of the initial fountain determine the overall behaviour and effectiveness of the equipment (DeRooij, 1999). In nature, particle-laden fountains are observed during volcanic eruptions when a mixture of gases, rocks, lava and dust is ejected upwards into the air (Woods, 1995). This is a highly complex flow since the hot gases may be positively buoyant, whereas the rocks and particles are more dense than the ambient air. This can cause the bulk flow to be negatively buoyant, and the entire mixture forms a multiphase fountain, or the particles separate from the up-flowing gases at some height depending on the size and weight of individual particles (Mingotti and Woods, 2016). Such particle-laden fountains may feed particle-driven gravity currents which can propagate kilometres before coming to rest (Bonnecaze et al., 1993; Simpson, 1999; Ungarish, 2009). Understanding the source conditions of such flows can help inform models of the run out and hence strategies to mitigate associated hazards. In the sixth chapter we present a detailed experimental and theoretical investigation of the particle transport in particle-driven gravity currents in water. The experiments are complemented by a novel theoretical model which accounts for particle settling at the base of the gravity current and the release of source fluid through the top of the gravity current owing to the establishment of a sedimentation front. Comparison with the experimental data confirmed that the model correctly predicts the height profile and the run-out length of the gravity current in which the height gradually reduces with distance from the source. This chapter has been published in the *Journal of Fluid Mechanics* in 2020.

In total, this thesis contains 7 chapters, including this introduction in chapter 1 and a summary and discussion of the results in chapter 7.

1.3 A brief review of single-phase jets, plumes and fountains

Our investigation of multiphase fountains presented in this thesis builds on an extensive set of previous work on single-phase fountains (Baines and Turner, 1969; Bloomfield and Kerr, 2000; Burridge and Hunt, 2013, 2016; Hunt and Burridge, 2015; Linden, 1999; Mizushina et al., 1982; Turner, 1966). Much of this work, in turn, builds on decades of research on single-phase jets and plumes (List, 1982; Morton et al., 1956; Woods, 2010). It is therefore useful to re-visit some of the fundamental work on single-phase jets, plumes and fountains here in the general introduction as this guides the work presented throughout the thesis. More detailed introductions considering the exact working fluids and the experimental set-ups are found in the relevant chapters.

1.3.1 Single-phase jets

Single-phase jets are easily produced by issuing fresh water through a submerged nozzle into a tank filled with fresh water. Dye may be added to the source liquid to visualise the flow as shown in figure 1.2 (a), where the nozzle is placed at the bottom of a tank. The flow is driven by its initial momentum at the source. Upon exiting through the nozzle, the jet decelerates by entraining ambient water and it spreads laterally, as illustrated by the cartoon in figure 1.2 (b) (List, 1982). Jets issuing through a point source are axisymmetric. The velocity distribution through a horizontal cross-section may be approximated by a Gaussian profile (Morton et al., 1956). Assuming axial symmetry, the volume flux through any infinite horizontal cross-section at height z may be written as

$$Q(z) = \int_0^\infty 2\pi r(z)\tilde{u}(z,r)dr \tag{1.2}$$

where r is the radial distance from the centre line and $\tilde{u}(z,r)$ is the fluid velocity. Similarly, the momentum flux in the jet is

$$M(z) = Q(z)\tilde{u}(z,r) = \int_0^\infty 2\pi r(z)\tilde{u}^2(z,r)dr. \tag{1.3}$$

At high Reynolds numbers (Re $>$ 1000) the flow is turbulent and the entrainment is controlled by large scale eddies, which encourage mixing (List,

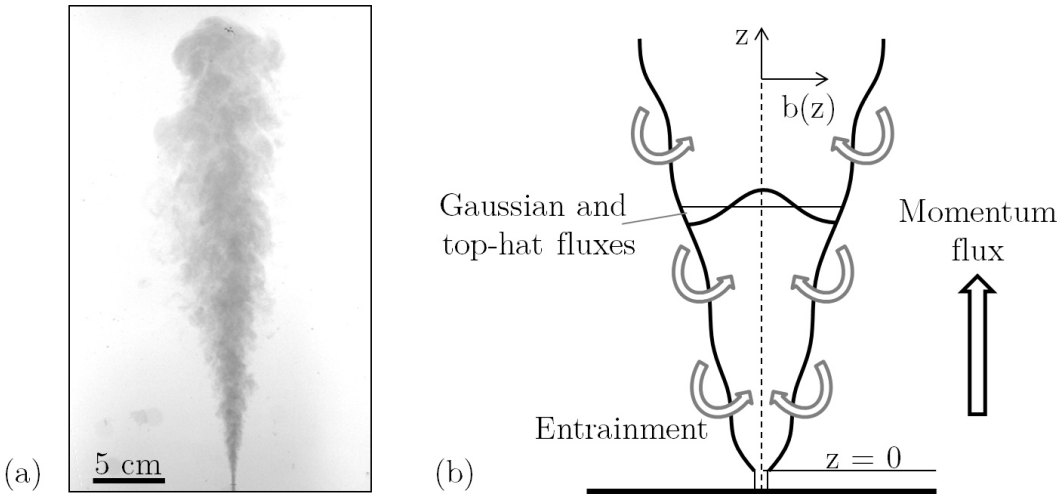

Fig. 1.2 (a) Experimental image of a turbulent single-phase jet. Dyed fresh water is injected upwards into a tank filled with fresh water. The flow decelerates and spreads laterally owing to the entrainment of ambient fluid. (b) Schematic of a turbulent single-phase jet. Illustrated are the Gaussian distribution of the fluid velocity as well as the horizontally-averaged top-hat velocity.

1982). Highly turbulent jets are commonly modelled with a *top-hat description*, which assumes a horizontally-averaged velocity and a well defined radius at each height as shown in figure 1.2 (b) (Morton et al., 1956). In this top-hat description, equation 1.2 and 1.3 reduce to

$$Q(z) = \pi q(z) = \pi b^2(z) u(z) \tag{1.4}$$

and

$$M(z) = \pi m(z) = \pi b^2(z) u(z)^2 \tag{1.5}$$

where $b(z)$ and $u(z)$, without the tilde symbol, are the top-hat radius and velocity, respectively.

The volume flux of the jet increases as it entrains ambient liquid. Morton, Taylor and Turner (1956) have developed an entrainment hypothesis which has been widely adopted in the literature. This hypothesis quantifies the entrainment of ambient liquid at some height in the jet as being proportional to the top-hat velocity of the fluid at this height,

$$\frac{dQ(z)}{dz} = \alpha\, 2\pi b(z)\, u(z) = \alpha\, 2\pi\, m(z)^{1/2}, \tag{1.6}$$

where α is the entrainment coefficient. For a single-phase jet, α is approximately 0.076 ± 0.004 (Bloomfield and Kerr, 2000). The momentum flux is independent of height, so that equation 1.6 can be integrated to obtain an expression for the volume flux as a function of z,

$$Q(z) = Q_0 + z\,\alpha\,2\pi\,m_0(z)^{1/2}, \tag{1.7}$$

where the subscript 0 denotes the source fluxes at the nozzle.

1.3.2 Single-phase plumes

Plumes are localised flows, driven by the density difference between the plume fluid and the environment (Woods, 2010). Unlike jets, they do not rely on an initial momentum flux. Plumes were first described in detail by Morton, Taylor and Turner (1956). Figure 1.3 (a) shows an experimental image of a single-phase plume. It is of interest to note that the shape of the plume and the jet (cf. figure 1.2 (a)) appear very similar, even though the mechanism behind the fluid transport is very different.

The difference in density between the plume fluid, ρ_p, and the ambient fluid, ρ_e, results in a reduced gravitational acceleration at the source,

$$g_0^{'} = g\frac{\rho_{p,0} - \rho_e}{\rho_e}, \tag{1.8}$$

where $g = 9.81\,\mathrm{m/s^2}$ is the gravitational acceleration. This density difference between the plume fluid and the ambient fluid leads to a buoyancy flux, $B(z)$, across an infinite horizontal area at height z

$$B(z) = \int_0^\infty 2\pi r\tilde{u}(z,r)g\frac{\tilde{\rho}(r,z) - \rho_e}{\rho_0}dr, \tag{1.9}$$

where $\tilde{\rho}(r,z)$ is the Gaussian distribution of density in the plume fluid. In the top-hat description, the buoyancy flux simplifies to

$$B(z) = \pi f(z) = g^{'}(z)\pi b^2(z)u(z) = g^{'}(z)Q(z). \tag{1.10}$$

Equations 1.4 and 1.5 remain valid, so that the plume is defined in terms of the conservation equations for the fluxes of volume, momentum and buoyancy. In an environment of uniform density the changes of these three fluxes with height are

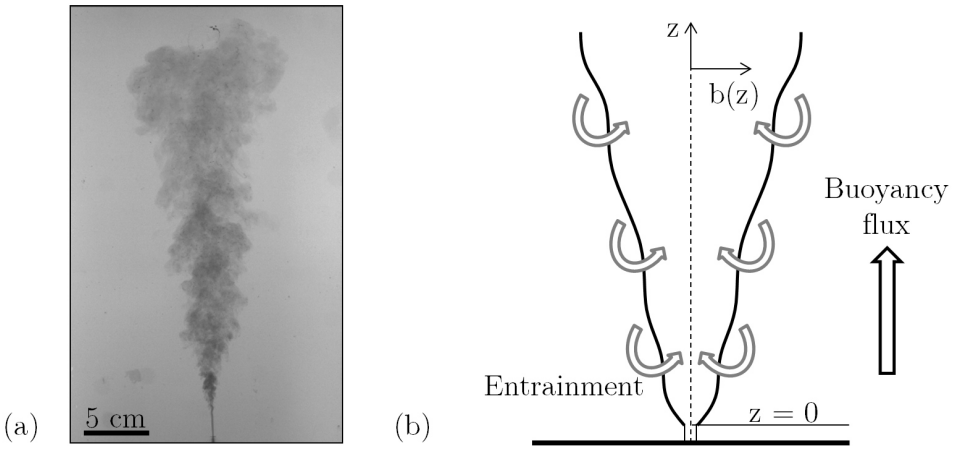

Fig. 1.3 (a) Experimental image of a turbulent single-phase plume. Dyed fresh water is injected upwards into a tank filled with more dense salt water. The flow is driven by its density deficiency compared to the environment and it spreads laterally owing to the entrainment of ambient liquid. (b) Schematic of a turbulent single-phase plume. The vertical co-ordinate z is taken as positive upwards.

$$\frac{dQ(z)}{dz} = \alpha\, 2\pi b(z)\, u(z) = \alpha\, 2\pi\, m(z)^{1/2}, \tag{1.11}$$

$$\frac{dM(z)}{dz} = \pi b^2(z) g^{'}(z), \tag{1.12}$$

$$\frac{dB(z)}{dz} = 0. \tag{1.13}$$

These conservation equations for the volume, momentum and buoyancy fluxes can be integrated to obtain analytic expressions for the plume radius, the top-hat fluid velocity and the reduced gravity as a function of the vertical co-ordinate z, as shown by Morton et al. (1956):

$$b(z) = \frac{6\alpha}{5} z, \tag{1.14}$$

$$u(z) = \frac{5}{6\alpha}\left(\frac{9}{10}\alpha f_0\right)^{1/3} z^{-1/3}, \tag{1.15}$$

$$g^{'}(z) = \frac{5 f_0}{6\alpha}\left(\frac{9}{10}\alpha f_0\right)^{-1/3} z^{-5/3}. \tag{1.16}$$

1.3.3 Single-phase fountains

Fountains are localised flows in which, at the source, the direction of the momentum flux opposes the direction of the buoyancy flux (Hunt and Burridge, 2015). A jet-like core develops which decelerates owing to gravitational effects and the entrainment of ambient liquid until the fountain reaches a maximum height at which the fluid comes to rest. At the top of the fountain, the fluid reverses its motion and falls back in a collar around the fountain core. A complicated exchange of fluid between the core, the collar and the ambient develops (Bloomfield and Kerr, 2000). With the return flow fully established, the fountain core entrains some of the return flow so that the overall fountain height reduces to a new steady value (Turner, 1966). An image of a single-phase fountain is shown in figure 1.4 (a) and a schematic of the fountain dynamics is shown in panel (b).

Bloomfield and Kerr (2000) have developed a full model of axisymmetric fountains based on conservation equations of the fluxes of volume, momentum and buoyancy. Burridge and Hunt (2015) reviewed turbulent single-phase fountains, combining multiple sets of experiments and classifying the fountains based on their source Froude number,

$$Fr_0 = \frac{u_0}{\sqrt{b_0 g_0'}} = \frac{m_0^{5/4}}{q_0 f_0^{1/2}} \tag{1.17}$$

where the subscript "$_0$" specifies source conditions. Extensive sets of experimental data (Hunt and Burridge, 2015; Turner, 1966) have shown that for turbulent fountains and $Fr_0 > 1$ the steady height of a single-phase fountain scales as

$$H_{SPF} \propto Fr_0 b_0 = m_0^{3/4} f_0^{-1/2} \tag{1.18}$$

where $m^{3/4} f_0^{-1/2}$ is a characteristic length scale of the fountain. The constant of proportionality for such fountains is 2.46.

In a similar fashion, we can compose a characteristic fountain velocity based on the source fluxes of buoyancy and momentum

$$u_F = f_0^{1/2} m_0^{-1/4}. \tag{1.19}$$

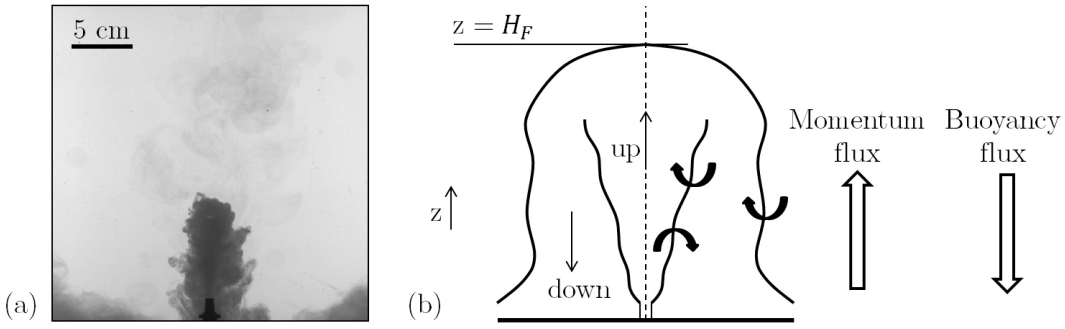

Fig. 1.4 (a) Experimental image of a turbulent single-phase fountain. Dyed salt water is injected upwards into a tank filled with less dense fresh water. The flow decelerates owing to its negative buoyancy and the entrainment of ambient water. (b) Schematic of a turbulent single-phase fountain. Illustrated are the jet-like fountain core in which fluid travels upwards, as well as the collapsing return flow around this core. At the source, the direction of the buoyancy flux opposes the direction of the momentum flux.

In multiphase fountains, the ratio of this characteristic velocity and the fall speed (or rise speed) of the second phase determines if the fountain behaves like an analogous single-phase fountain with the same source fluxes of buoyancy and momentum, or whether the particles separate from the flow before the fountain fluid runs out of momentum (Mingotti and Woods, 2016).

Chapter 2

Turbulent bubble fountains in water

2.1 Abstract

We explore the dynamics of turbulent bubble fountains produced when a descending stream of fresh water and air bubbles issues from a nozzle submerged in a tank of water. The bubbles have diameters of 2 to 5 mm and the fountains have source Froude numbers ranging from 10 to 240. The Reynolds numbers of the bubbly fountains range from 4,000 to 24,000. The bubbles, carried into the tank by the downward jet of water, lead to a buoyancy force which reduces the downward momentum of the jet, thus producing a fountain. We find that H_F, the downward penetration distance of the bubbles into the water reservoir, may be characterised by two parameters: Λ, the ratio of the bubble rise speed to the characteristic fountain velocity, $u_F = f_0^{1/2}/m_0^{1/4}$, and Fr_0, the source Froude number, given by $m_0^{5/4}/(q_{W_0} f_0^{1/2})$, where q_{W_0}, m_0 and f_0 are the source volume, momentum and buoyancy fluxes. As Λ increases, H_F decreases, a result which is directly analogous to the height of rise of particles in a particle-laden fountain (Mingotti and Woods, 2016). Also, we find that H_F increases as Fr_0 increases, a result directly analogous to single-phase fountains (Turner, 1966).

We present a model for the conservation of volume, momentum and buoyancy fluxes and use this to predict the penetration distance of the bubbles corresponding to the point at which the fountain liquid velocity equals the bubble rise speed. Using the best-fit value for the entrainment coefficient, $\alpha = 0.04 \pm 0.004$, we find that our experimental measurements of the bub-

ble penetration distance are in good accord with the model predictions for $10 < Fr_0 < 240$ and $2 < \Lambda < 15$. In our experiments the bubble rise speed, u_{slip}, is large compared to the entrainment velocity of the descending fountain. Thus, only a small fraction of the rising bubbles are re-entrained, and so the buoyancy flux of the fountain is approximately independent of depth. Flow-visualisation experiments also show that the liquid momentum flux is not exhausted at the point of bubble separation and so the liquid in the fountain continues to travel downward, separated from the bubbles. We use the new theoretical model to estimate the flux of air entrained into plunging water jets.

2.2 Introduction

Turbulent bubble fountains form when gas bubbles are carried into a liquid by a downward jet of water. They frequently arise in industrial processes, most commonly in the form of air bubbles entering a liquid reservoir. Two-phase fountains can be highly desirable when aerating oxygen-scarce water (Biń, 1993; McDougall, 1978), or highly undesirable when contamination of the liquid with bubbles is to be avoided. Examples of the latter case include the foaming induced when refuelling a petrol tank and the entrainment of air into oil as it refills the sump of an engine. In particular connecting-rod bearings in car engines show increased wear when the lubricant is laden with bubbles (Nemoto et al., 1997). The purpose of this work is to broaden our understanding of bubble fountains and in particular the controls on the penetration depth of the bubbles.

We present a new set of systematic experiments in which we generate turbulent bubble fountains via a co-flow of air and fresh water issuing through a submerged nozzle. This set-up allows for a precise control of both the air and water flow rates at the source. We explore scalings for our experimental measurements of bubble penetration depth in terms of the initial fluxes of volume, momentum and buoyancy, and we present an integral model which describes how these horizontally-averaged fluxes develop in the vertical direction. The model quantifies the effect of the bubble slip velocity, u_{slip} (the terminal rise speed of an individual air bubble in water), on the fountain dynamics and quantifies the mixing with ambient liquid. Comparison of the model with experimental data yields a best-fit entrainment coefficient, α. The model

predictions for bubble penetration distance are in good accord with the new experimental data.

Our experiments build on existing literature about bubble fountains generated by plunging water jets (Bińi, 1993), for which a constant bubble slip velocity has been observed (Clanet and Lasheras, 1997). In contrast to those experiments, using a co-flow of air and water issuing from a submerged nozzle, we are able to vary the source buoyancy flux independently of the source momentum flux.

The dimensional analysis presented in this chapter is inspired by previous investigations of single-phase fountains in which the properties of the flow have been shown to depend on the Froude number at the source, $Fr_{0_{SPF}} = u_0/\sqrt{g^{'}\, b_0}$, where u_0 is the initial velocity and b_0 the nozzle radius (Burridge and Hunt, 2013; Hunt and Burridge, 2015; Turner, 1966). The reduced gravity is given by $g^{'} = g\,(\rho_a - \rho_F)/\rho_a$, with ρ_a the density of the ambient liquid and ρ_F the bulk density of the fountain fluid. The Froude number may also be expressed in terms of the initial volume, momentum and buoyancy fluxes, $q_{W_0} = Q_{W_0}/\pi = b_0^2 u_0$, $m_0 = M_0/\pi = b_0^2 u_0^2$ and $f_0 = B_0/\pi = g^{'} b_0^2 u_0$, giving the expression

$$Fr_0 = \frac{m_0^{5/4}}{q_{W_0} f_0^{1/2}}. \tag{2.1}$$

We have combined these classical results (Hunt and Burridge, 2015; Turner, 1966) with recent experiments on particle-laden fountains produced from a negatively buoyant jet of fresh water laden with particles (Mingotti and Woods, 2016). In this latter study, it was shown that if the fall speed of the particles, u_{fall}, exceeds the characteristic speed of the fountain, given by

$$u_F = \frac{f_0^{1/2}}{m_0^{1/4}}, \tag{2.2}$$

then the particles fall out below the height of the equivalent single-phase fountain. By analogy with heavy particles falling from a particle-laden fountain, we introduce the dimensionless parameter

$$\Lambda = \frac{u_{slip}}{u_F} \tag{2.3}$$

where u_{slip} is the terminal rise speed of the bubbles. In the present experiments, the bubbles with diameters of 2 to 5 mm have a terminal rise speed of 0.28 m/s

(Clift et al., 2005, p.172). If the dimensionless parameter Λ is small ($\Lambda < 0.5$), multiphase fountains resemble classical single-phase fountains (Mingotti and Woods, 2016). For a given set of source conditions, this requires the terminal velocity (terminal rise speed for bubbles or terminal fall speed for heavy particles) to be very small, which is most commonly observed if the contaminants (bubbles or particles) are very small in diameter. We have been able to explore the range from $2 < \Lambda < 15$. This indicates that the fountains do not behave as single-phase fountains. Indeed, the bubbles separate from the fountain liquid before the liquid momentum flux is exhausted. Thus, we find that the downward penetration distance of the bubbles decreases relative to the height of a classical single-phase fountain as Λ increases.

In the integral model we propose for a bubble fountain, we work with the horizontally-averaged volume and momentum fluxes (Morton et al., 1956; Turner, 1966) but also account for the bubble slip velocity. Furthermore, as the bubble rise speed is large compared to the entrainment velocity associated with the entrainment of ambient liquid into the fountain ($u_{slip} > u_{ent}$), we expect that only a small fraction of the bubbles is re-entrained into the fountain so that the buoyancy flux remains approximately constant with height in the fountain. This differs from models of single-phase fountains for which the entrainment of the buoyant return flow leads to a variation of the fountain buoyancy flux with height (Bloomfield and Kerr, 2000; Carazzo et al., 2010; Turner, 1966). We test the model by direct comparison with our new experimental data. We then revisit observations of the bubble penetration distance in a bubble fountain produced when a downward jet of water impinges on a free surface. Combining our model with these observations, we are able to estimate the rate of entrainment of air into such impinging jets.

2.3 Experiments

Turbulent bubble fountains were generated when a co-flow of fresh water and air issued through a submerged nozzle into a tank of dimensions 40 cm x 20 cm x 20 cm as shown in the schematic in figure 2.1 (a). Panel (b) of figure 2.1 contains an image of a CAD model of the experimental apparatus and panel (c) shows a close-up of the nozzle section. The liquid was supplied from a pressurised tank and the flow rate was controlled by a *Parker liquid flow indicator* flowmeter (range: 3 to 33 ml/s). The air flux, regulated via a *Uniflux variable area*

flowmeter (range: 0.9 to 27 ml/s), was supplied from a compressed air line and fed into the centre of the liquid stream. Four round nozzles of diameter 2.9 mm, 3.84 mm, 5 mm and 6 mm, submerged 5 cm under the water surface, were used as the sources during the experiments.

A *JAI SP-5000* monochrome high-speed camera with a 1:28 *HAMA* lens was employed to record the motion of the air bubbles inside the tank. The camera was set to take 100 images per second for a period of ten seconds for each of the experiments listed in table 2.1. The lens was positioned to be at the height of the nozzle and a 400 Watt *PhotonBeam* halogen lamp was employed to illuminate the experiments. The light source was placed 30 cm away from the tank, orthogonal to the line of view of the camera to minimise reflections in the Perspex walls. A black plastic sheet was mounted to the back wall inside the tank to maximise the contrast between illuminated air bubbles and the background. A systematic set of 126 experiments was run for various source flux and nozzle diameter combinations as listed in table 2.1.

2.3.1 Experimental observations

The high-speed videos revealed that in our experiments the majority of air bubbles are spherical in shape with diameters between 2 and 5 mm. The average bubble size as well as the bubble shape remained constant for all source fluxes and nozzle sizes that we investigated. Measurement of the rise speeds confirmed the well-known experimental finding that the slip velocity of air bubbles in this size range rising through water is approximately constant (Clift et al., 2005, p.172), with a value of around 28 cm/s (± 4 cm/s).

The high-speed videos recorded for each of the 126 experiments listed in table 2.1 contain 1000 grey-scale images, covering a time span of 10 seconds. An individual frame of such a video is shown in figure 2.2 (a). In this instantaneous image, the white regions denote light reflected from the bubbles. The vertical red line marks the off-centre location at which the time-series image in figure 2.4 (c) has been computed. The variation with time of the maximum bubble penetration distance is shown in figure 2.4 (b). A *MATLAB* script was used to create a time-average by superimposing the 1000 grey-scale images from the slow-motion videos. We then use a false-colour map to illustrate the result. Figure 2.2 (b) shows such an image and represents the time-averaged intensity of the light reflected from the bubbles. In figure 2.2 (a) and (b) only the bubbles

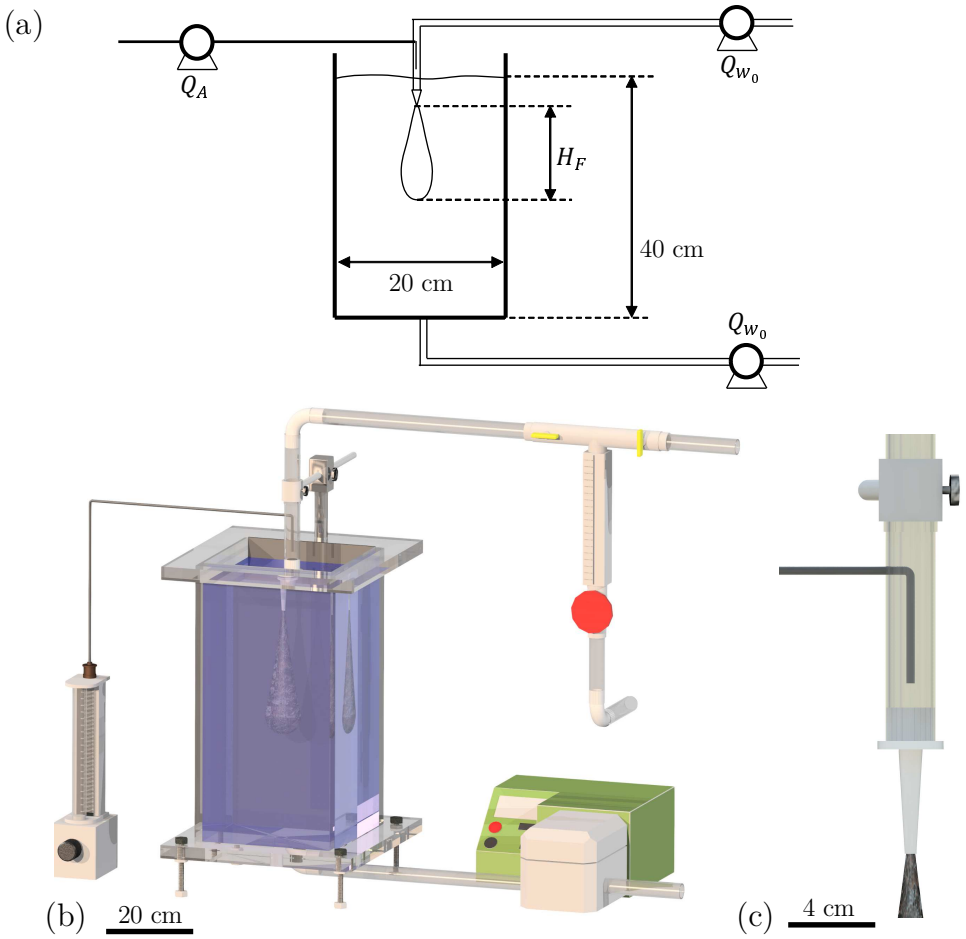

Fig. 2.1 (a) Schematic of the experimental set-up: A co-flow of air and water issues downwards through a nozzle submerged in a tank of water. The exact amount of liquid supplied through the nozzle is extracted at the bottom to ensure a steady water level. Both the water flux and the air flux through the nozzle can be controlled via valves and flowmeters. (b) CAD-model of the experimental apparatus with the air flowmeter to the left and the water flowmeter (with red control valve) to the right of the tank. (c) Close-up of the nozzle section of the CAD-model.

Exp.	d_N $[mm]$	Q_{W_0} $[ml/s]$	Q_A $[ml/s]$	H_F $[cm]$	Exp.	d_N $[mm]$	Q_{W_0} $[ml/s]$	Q_A $[ml/s]$	H_F $[cm]$
1	2.9	15	0.83	10.85	64	3.84	30	0.83	18.32
2	2.9	15	1.67	10.97	65	3.84	30	1.67	16.25
3	2.9	15	2.50	9.48	66	3.84	30	2.50	15.90
4	2.9	15	3.33	9.76	67	3.84	30	3.33	15.15
5	2.9	15	4.17	9.45	68	3.84	30	4.17	14.78
6	2.9	15	6.67	9.27	69	3.84	30	6.67	13.85
7	2.9	15	13.33	9.28	70	3.84	30	13.33	12.08
8	2.9	15	20.00	9.55	71	3.84	30	20.00	11.31
9	2.9	15	26.67	9.86	72	3.84	30	26.67	11.56
10	2.9	20	0.83	16.87	73	5	15	0.83	3.92
11	2.9	20	1.67	14.49	74	5	15	1.67	3.75
12	2.9	20	2.50	14.65	75	5	15	2.50	3.53
13	2.9	20	3.33	13.14	76	5	15	3.33	3.26
14	2.9	20	4.17	12.55	77	5	15	4.17	2.98
15	2.9	20	6.67	11.91	78	5	15	6.67	3.27
16	2.9	20	13.33	11.90	79	5	15	13.33	3.45
17	2.9	20	20.00	11.84	80	5	15	20.00	4.04
18	2.9	20	26.67	11.97	81	5	15	26.67	3.45
19	2.9	25	0.83	19.51	82	5	20	0.83	6.53
20	2.9	25	1.67	21.95	83	5	20	1.67	5.87
21	2.9	25	2.50	18.19	84	5	20	2.50	5.94
22	2.9	25	3.33	18.01	85	5	20	3.33	5.58
23	2.9	25	4.17	16.85	86	5	20	4.17	5.05
24	2.9	25	6.67	15.28	87	5	20	6.67	5.13
25	2.9	25	13.33	15.10	88	5	20	13.33	5.07
26	2.9	25	20.00	14.98	89	5	20	20.00	5.44
27	2.9	25	26.67	14.55	90	5	20	26.67	5.35
28	2.9	30	0.83	25.32	91	5	25	0.83	8.35
29	2.9	30	1.67	22.33	92	5	25	1.67	7.54
30	2.9	30	2.50	20.32	93	5	25	2.50	5.61
31	2.9	30	3.33	19.10	94	5	25	3.33	5.31
32	2.9	30	4.17	18.55	95	5	25	4.17	6.44
33	2.9	30	6.67	20.35	96	5	25	6.67	4.50
34	2.9	30	13.33	18.92	97	5	25	13.33	5.74
35	2.9	30	20.00	17.41	98	5	25	20.00	6.02
36	2.9	30	26.67	16.74	99	5	25	26.67	5.85
37	3.84	15	0.83	5.84	100	5	30	0.83	12.01
38	3.84	15	1.67	5.29	101	5	30	1.67	11.76
39	3.84	15	2.50	5.05	102	5	30	2.50	11.01
40	3.84	15	3.33	4.72	103	5	30	3.33	10.65
41	3.84	15	4.17	4.64	104	5	30	4.17	9.75
42	3.84	15	6.67	4.78	105	5	30	6.67	9.03
43	3.84	15	13.33	4.68	106	5	30	13.33	8.55
44	3.84	15	20.00	4.78	107	5	30	20.00	8.31
45	3.84	15	26.67	5.32	108	5	30	26.67	8.37
46	3.84	20	0.83	10.19	109	6	25	0.83	5.54
47	3.84	20	1.67	9.57	110	6	25	1.67	4.89
48	3.84	20	2.50	9.23	111	6	25	2.50	4.44
49	3.84	20	3.33	8.60	112	6	25	3.33	3.15
50	3.84	20	4.17	8.49	113	6	25	4.17	3.08
51	3.84	20	6.67	7.84	114	6	25	6.67	3.39
52	3.84	20	13.33	7.30	115	6	25	13.33	3.88
53	3.84	20	20.00	7.23	116	6	25	20.00	4.22
54	3.84	20	26.67	7.39	117	6	25	26.67	3.95
55	3.84	25	0.83	14.86	118	6	30	0.83	9.25
56	3.84	25	1.67	12.96	119	6	30	1.67	8.53
57	3.84	25	2.50	12.74	120	6	30	2.50	7.61
58	3.84	25	3.33	12.58	121	6	30	3.33	7.15
59	3.84	25	4.17	11.54	122	6	30	4.17	6.79
60	3.84	25	6.67	11.47	123	6	30	6.67	5.98
61	3.84	25	13.33	10.21	124	6	30	13.33	5.93
62	3.84	25	20.00	10.03	125	6	30	20.00	6.47
63	3.84	25	26.67	9.58	126	6	30	26.67	6.13

Table 2.1 Range of experimental source conditions for turbulent bubble fountains: Number of experiment (Exp.), nozzle diameter (d_N), water flux (Q_{W_0}), air flux (Q_A) and measured bubble penetration distance (H_F). The corresponding values of Fr_0 and Λ are displayed in figure 2.6.

are visible. In figure 2.2 (c), dye has been added to the source liquid to visualise the flow path of the liquid phase of the fountain fluid. This experiment shows that the majority of the source liquid continues to travel downwards after the bubbles have separated from the flow. The false-colour image highlights that the amount of fountain liquid carried upwards by the rising bubbles is negligible. For this experiment, the concentration of dye was kept very low so that it did not have a significant influence on the buoyancy of the flow. The images in figure 2.2 (a) to (c) were obtained for the source conditions of experiment 14 in table 2.1 ($Fr_0 = 70;\ \Lambda = 5.4$).

Figure 2.2 (d) contains an averaged fountain shape for a single-phase fountain with the same source buoyancy and momentum fluxes as the multiphase bubble fountains in panels (a) to (c). Comparison of the bubble fountain and the single-phase fountain shows that for a given set of source flux conditions the fluid in the single-phase fountain penetrates further into the ambient than the bubbles in the bubble fountain. Furthermore, the single-phase fountain collapses when it runs out of momentum and the dyed liquid ascends around the central down-flowing fountain. This results in a collar-like annular up-flow region that interacts with the jet-like down-flowing fountain core (Bloomfield and Kerr, 2000; Carazzo et al., 2010; Hunt and Burridge, 2015). In the present turbulent bubble fountains we did not observe such a collapsing flow around the central fountain (cf. figure 2.2 (c)). By amplifying the light intensities and changing the false colours used in the image shown in figure 2.2 (b), we can identify a cylindrical region around the fountain core in which the bubbles rise to the surface after separating from the liquid phase of the fountain fluid (cf. figure 2.3 (a)). The image intensity in this region is less pronounced as the concentration of bubbles is low compared to the fountain core and the bubbles quickly rise to the surface and escape. The cartoon in figure 2.3 (b) summarises the observations presented in figures 2.2 and 2.3 (a). The schematic shows that the bubbles are carried downwards by the water jet up to the point at which the liquid velocity in the fountain core matches the slip velocity of the bubbles. At this point the bubbles can separate from the flow and they rise upwards in the cylindrical region shown in figure 2.3 (a). The fountain liquid continues to propagate downwards owing to its residual momentum. The cartoon illustrates the definition of the maximum bubble penetration depth, H_F, the nozzle radius, b_0, and the direction of the vertical co-ordinate z.

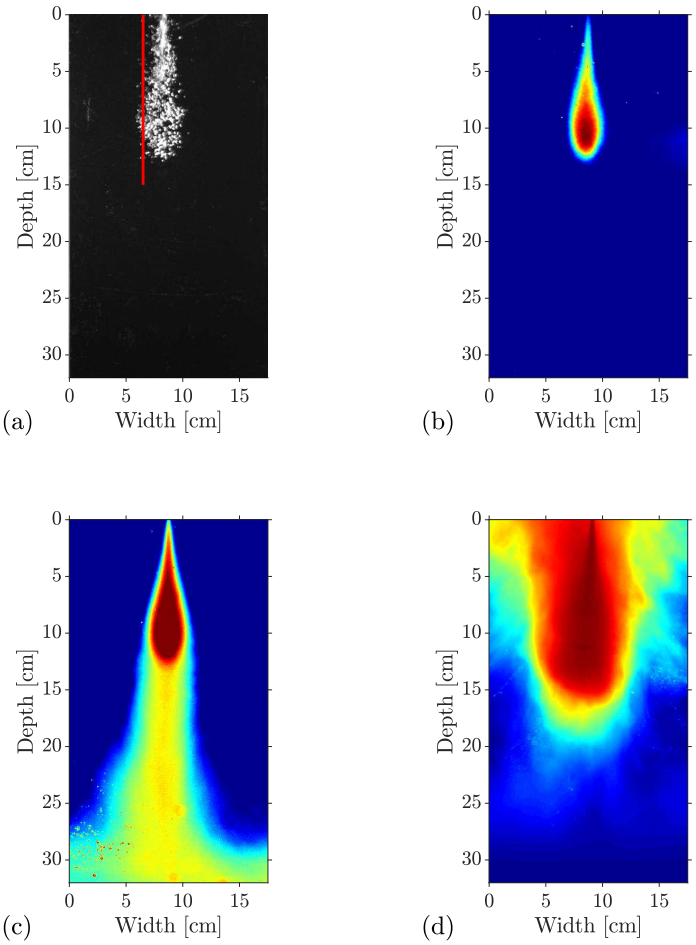

Fig. 2.2 Illustrations of instantaneous (black and white image) and averaged (false-colour images) fountain shapes. (a) Instantaneous image in which the white regions denote light reflected from the bubbles. The air bubbles reach a maximum penetration depth of around 12 cm. The vertical red line defines the off-centre location of the time-series image shown in figure 2.4 (c). (b) False-colour image in which the colour denotes a time-averaged intensity of the reflected light from the bubbles over an averaging period highlighted by the red rectangle (I) in figure 2.4. (c) False-colour image of the bubble fountain displayed in (b) with dyed source liquid. The averaging period corresponds to rectangle (II) in figure 2.4. The liquid phase of the fountain fluid continues to propagate downwards in the tank after the air bubbles have separated from the liquid. The fountains shown in panels (a) - (c) correspond to experiment 14 (table 2.1) with $Fr_0 = 70$ and $\Lambda = 5.4$. (d) False-colour image of a single-phase fountain (fresh water injected into a salt water solution) in which the initial buoyancy and momentum fluxes correspond to that of the bubble fountains shown in panels (a) to (c). The single-phase fountain reaches a maximum distance of around 18 cm below the nozzle and then all the fountain liquid rises to the top of the tank.

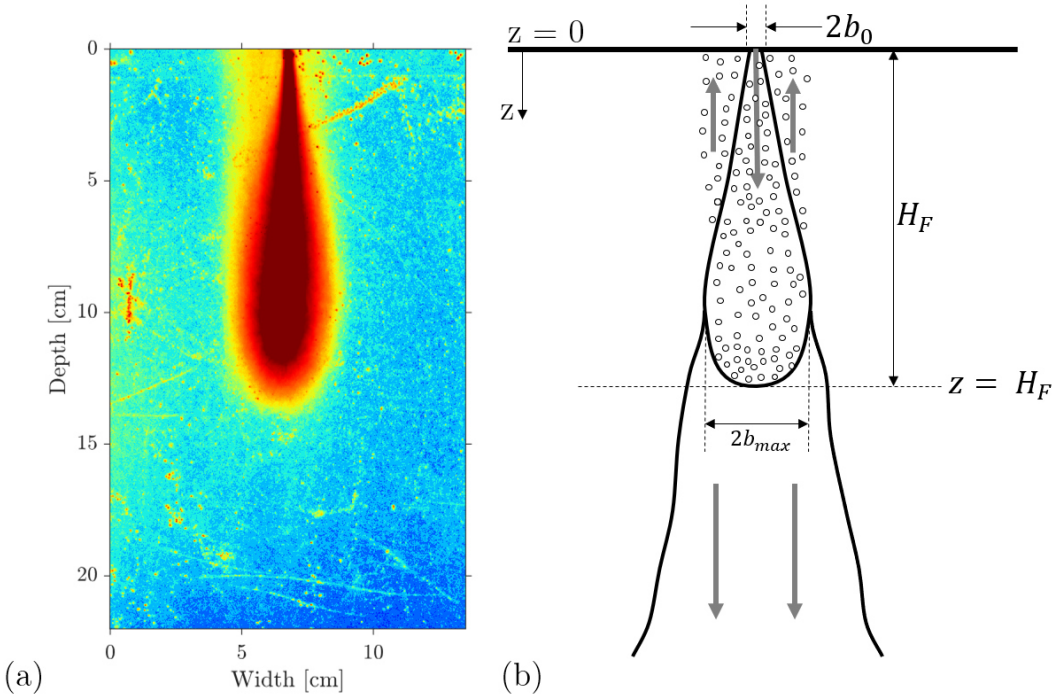

Fig. 2.3 (a) False-colour image of the averaged fountain profile recorded for experiment 14 in table 2.1, corresponding to the fountain shown in figure 2.2 (a) to (c). In this figure, however, the image intensity has been amplified and the colour bar adjusted to visualise the cylindrical region in which the air bubbles rise after having separated from the liquid phase of the fountain fluid. (b) Cartoon summarising the experimental observations. The bubbles separate from the flow at $z = H_F$. At this point the liquid velocity equals the bubble slip velocity, $u(H_F) = u_{slip}$. The liquid phase of the fountain continues to propagate as a simple jet owing to its residual momentum. The vertical co-ordinate, z, is positive downwards.

A second imaging technique utilises time-series images, taken through the centre line of the fountain. This provides detailed information about the evolution of maximum fountain height over time (Williamson et al., 2008). An image of such a time-series is shown in figure 2.4 (a). The first six seconds show the penetration of air bubbles into the tank up to a maximum distance of around 12 cm measured from the base of the nozzle. After 6 seconds, the source liquid is dyed to show that the liquid phase of the fountain fluid continues to propagate downwards after the bubbles have separated from the flow. This indicates that the liquid momentum flux is not exhausted at the maximum bubble penetration depth. The two red rectangles labelled (I) and (II) define the time intervals over which the averaged fountain shapes in figure 2.2 (b) and (c) have been computed.

Figure 2.4 (b) shows a time-series image of the maximum penetration distance of a bubble fountain with an initial gas fraction of approximately 40%. Although this is initially very gas rich, the mixing and dilution with ambient liquid rapidly reduces the gas fraction. The region shaded in grey is the area in which bubbles can be found. The red line marks the bottom border of the bubble region and illustrates how the instantaneous bubble penetration depth fluctuates over time, while the horizontal green line shows the time-averaged fountain depth.

The image in figure 2.4 (c) shows a time-series of a vertical line, away from the centre of the fountain (red line in figure 2.2 (a)). This time-series identifies a series of rising bubbles, seen by the sloping lines. The majority of these lines rise to the top of the image, indicating that bubbles rise beyond the top of the fountain, and are not re-entrained.

The experimental set-up, in which we can independently control the flux of air and water through a submerged nozzle, allows us to investigate the influence of variations in the source buoyancy flux for a fixed source momentum flux. The four averaged fountain shapes displayed in false-colour in figure 2.5 were obtained for the same source momentum flux, but the source buoyancy flux increases from panel (a) to panel (d). The liquid and the gas enter the tank through the same nozzle. Assuming that the gas and liquid have the same exit velocity from the nozzle, then an increase in either the liquid flux or the gas flux results in a larger nozzle exit velocity, as given by the relation

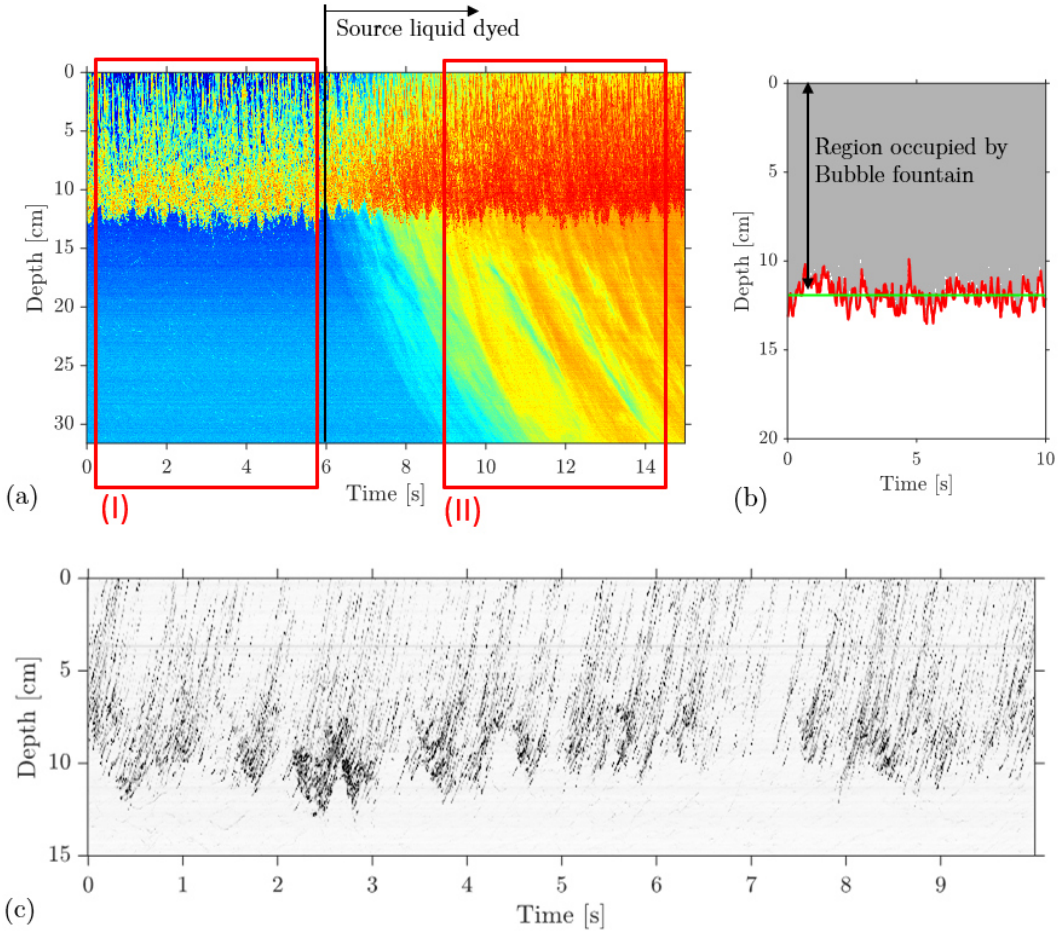

Fig. 2.4 (a) Time-series of the vertical line through the centre of a turbulent bubble fountain, shown in false-colour. For times less than 6 s, the image represents the intensity of light reflected from the bubbles. For times after 6 s, the liquid phase of the fountain fluid is dyed and may also be seen in the false-colour image. Although the bubbles only penetrate to a depth of approximately 12 cm, the liquid and hence dye continues downwards into the tank. The two red rectangles mark the time intervals over which individual frames have been averaged to extract averaged fountain shapes. These averaged fountain contours are displayed in figure 2.2 (b) and (c). Figure 2.4 (b) shows an enlarged image of the bubble penetration depth into the tank. The bubble-laden region is shaded in grey. This image highlights the fluctuation of fountain height with time, shown as a red line. The bubble penetration depths listed in table 2.1 correspond to the average fountain height shown as a green horizontal line. (c) Time-series of a vertical line, off-centre of the fountain as indicated by the red line in figure 2.2 (a). All lines have a similar gradient implying that the rise speed of the bubbles is $u_{slip} = 28 \pm 4\,\mathrm{cm/s}$. The straightness of the lines reflects the rapid adjustment of the bubbles to their terminal rise speed. The majority of the inclined lines extend to the top of the image suggesting that very few bubbles are re-entrained into the fountain.

$$u_0 = \frac{Q_{W_0} + Q_A}{\pi\, b_0^2} = \frac{Q_{W_0}}{\pi\, b_0^2\,(1 - C_0)} \tag{2.4}$$

where Q_{W_0} and Q_A are the source volume fluxes of water and air, respectively and C_0 is the gas volume fraction inside the nozzle, given by

$$C_0 = \frac{Q_A}{Q_{W_0} + Q_A}. \tag{2.5}$$

Our assumption that the nozzle exit velocities of the liquid and gas are equal in magnitude is motivated by the observation that the bubble diameters (d_B = 2 - 5 mm) are comparable in size to the nozzle diameters (d_N = 3 - 6 mm).

The source momentum flux is proportional to the square of the initial velocity, u_0. The momentum flux is carried almost completely by the liquid phase of the fountain fluid as the density of air is three orders of magnitude smaller than the density of water. The source momentum flux can thus be written as

$$M_0 \approx (1 - C_0)\,\pi\, b_0^2\, u_0^2. \tag{2.6}$$

Fountains with the same initial liquid flow rate and the same nozzle exit velocity have comparable initial momentum fluxes, irrespective of the air flow rate. At a constant liquid flux, the nozzle exit velocity can be kept constant by increasing the nozzle radius and simultaneously increasing the air flow rate such that u_0 remains unaffected. Following this procedure, we can investigate fountains with a constant source momentum flux but varying buoyancy fluxes. Figure 2.5 shows that increasing the initial gas volume fraction from (a) 8% to (d) 78% yields a height reduction of around 9 cm or 60%, despite the fact that the source momentum flux remains constant. In single-phase fountains there is a decrease in fountain height when the buoyancy flux is increased for a given source momentum flux (Hunt and Burridge, 2015; Morton et al., 1956; Turner, 1966). However, models describing the maximum penetration depth of bubbles in bubble fountains produced by a liquid jet plunging through the surface of a liquid reservoir have neglected the influence of the buoyancy flux (e.g. Clanet and Lasheras (1997)). With the present experimental set-up, we show that, as may be anticipated from the single-phase fountain results, the source buoyancy flux can indeed have a significant effect on the maximum bubble penetration depth.

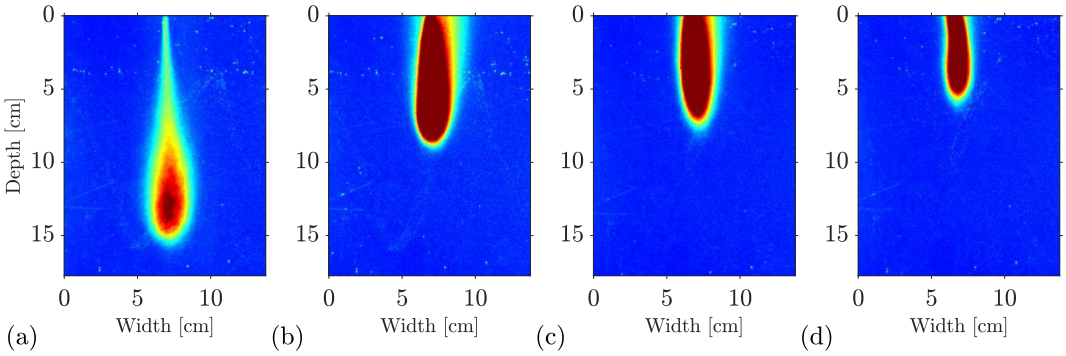

Fig. 2.5 Four averaged fountain shapes (averaging period = 10 s) at the same constant momentum flux with different buoyancy fluxes. The source gas volume represents a fraction of (a) 8% (b) 47% (c) 69% and (d) 78% of the total volume of fluid issuing from the nozzle. The images are shown in false-colour produced from the reflection of light by the bubbles in the fountain. No dye was used in the liquid phase of the fountain fluid in these experiments.

2.3.2 Scaling of experimental results

Figure 2.6 (a) shows the values of Fr_0 and Λ used in each of our experiments. The colour-coding indicates the measured bubble penetration depth in centimetres. Experiments reported by Turner (1966) and Hunt and Burridge (2015) suggest that the height of rise of single-phase fountains with $Fr_0 > 4$ scales as

$$H_{F_{single-phase}} = 2.46 \frac{m_0^{3/4}}{|f_0|^{1/2}} \tag{2.7}$$

where $m_0^{3/4}/|f_0|^{1/2}$ is a characteristic length scale of the fountain.

Mingotti and Woods (2016) showed that particle-laden fountains behave similarly to single-phase fountains if $\Lambda_P = u_{fall}/u_F << 1$, where u_{fall} is the terminal fall velocity of a single particle in water. For values of Λ_P greater than unity, however, the rise height of the particles decreases compared to that of a single-phase fountain. By analogy, in the present problem, we compare the terminal rise velocity of a bubble, u_{slip}, with the characteristic fountain velocity, u_F. We find that u_{slip} has a value of 28 ± 4 cm/s, in accord with published data (Clift et al., 2005, p.172). This slip velocity is large compared to the characteristic fountain velocity, u_F, in our experiments so that we did not access the region $\Lambda < 1$. Our experimental data, however, confirms that the maximum bubble penetration depth decreases with Λ for $\Lambda > 2$ and that these depths are smaller than the height of the analogous single-phase fountain. Indeed, figure 2.6 (b) illustrates the maximum penetration distance of bubbles, normalised by

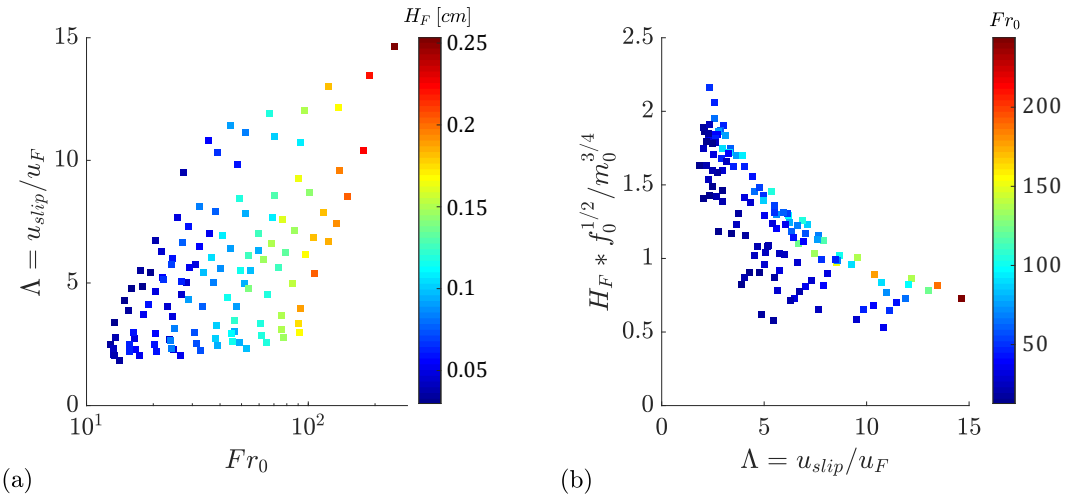

Fig. 2.6 (a) Illustration of the Fr_0-Λ-space covered by our new experiments. The colour-coding specifies the bubble penetration distance in centimetres. (b) Illustration of the bubble penetration distance, H_F, normalised by the scaling for the height of a single-phase fountain, $m_0^{3/4} f_0^{-1/2}$, as a function of Λ, the ratio of bubble slip speed and characteristic fountain velocity. The colour-coding specifies Fr_0.

the characteristic single-phase fountain length scale, $m_0^{3/4}|f_0|^{-1/2}$, as a function of $\Lambda = u_{slip}/u_F$. The colour-coding specifies the source Froude number for each of the 126 data points. Error bars have been omitted for clarity; these are shown in figure 2.9. For reference, with this scaling for the length, a classical single-phase fountain would reach a dimensionless height of 2.46. Figure 2.6 (b) shows that the non-dimensional height decreases as Λ increases. There is also a trend in the colour-coding which indicates that for a given value of Λ, experiments with higher values of Fr_0 have systematically larger heights than experiments with lower Fr_0 (figure 2.6 (b)). In the next section, we develop a model for the bubble fountain in an attempt to understand these data.

2.4 A theoretical model

Theoretical models for turbulent single-phase fountains have been based on conservation equations for horizontally-averaged momentum, buoyancy and volume fluxes (Bloomfield and Kerr, 2000; McDougall, 1981; Morton et al., 1956; Turner, 1966). We build on this approach to describe the bubble fountains produced from a co-flowing stream of air and water issuing from a submerged nozzle, as described above. On its own, the liquid stream would behave as a jet,

decelerating as it entrains ambient liquid. The gas phase, however, introduces buoyancy effects, leading to a more rapid deceleration of the flow up to the point of bubble separation, which is assumed to occur when the magnitude of the bubble rise speed matches the downward speed of the fountain liquid. The bubbles are modelled to have a descent speed equal to the difference between the liquid velocity and their rise speed, $u_B(z) = u(z) - u_{slip}$; we justify this simplification in section 2.6 in which we compare the predictions of the present simplified model with a more detailed model in which we account for the change in speed of bubbles relative to the liquid over time. Note that the rise speed of all bubbles in the size range 2 to 5 mm, which is characteristic of the present bubble fountains, is similar at approximately 28 ± 4 cm/s (Clift et al., 2005, p.172). Hence, as a first approximation, we assume there is a single rise speed.

We introduce the variables $\widetilde{C}(z,r)$, $\widetilde{u_B}(z,r)$ and $\widetilde{u}(z,r)$ to represent the time-averaged gas volume fraction, gas speed and liquid speed in the fountain as a function of the vertical coordinate z and radial coordinate r. We denote the horizontally-averaged *top-hat* volume fraction, $C(z)$, gas velocity $u_B(z)$, liquid velocity $u(z)$ and fountain radius $b(z)$, in terms of the volume flux, $Q_W(z) = \pi\, q_W(z)$, gas flux, $Q_A(z) = \pi\, q_A(z)$, and momentum flux, $M(z) = \pi\, m(z)$ in the fountain, according to the relations

$$q_A(z) = \int_0^\infty \widetilde{C}(z,r)\; 2\, r\; \widetilde{u_B}(z,r)\; dr = C(z)\; b(z)^2\; (u(z) - u_{slip}). \tag{2.8}$$

$$q_W(z) = \int_0^\infty (1 - \widetilde{C}(z,r))\; 2\, r\; \widetilde{u}(z,r)\; dr = (1 - C(z))\; b(z)^2\; u(z) \tag{2.9}$$

$$m(z) \approx m_W(z) = \int_0^\infty (1 - \widetilde{C}(z,r))\; 2\, r\; \widetilde{u}(z,r)^2\; dr = (1 - C(z))\; b(z)^2\; u(z)^2 \tag{2.10}$$

where $(1 - C(z))$ is the liquid volume fraction. In evaluating the total momentum flux of the fountain, we should, in principle, account for the sum of the momentum carried by the gas and the liquid phase. However, as the density of air is three orders of magnitude smaller than the density of water, the contribution of the gas phase to the overall momentum is negligible and so

in equation 2.10 we only account for the momentum flux of the liquid phase of the fountain fluid.

In the model, we assume that on leaving the nozzle, the vertical bubble velocity rapidly adjusts to the value $u_0 - u_{slip}$, where the terminal bubble rise speed is $u_{slip} \approx 28$ cm/s. As a simplification we estimate the properties of the flow beyond this adjustment zone by assuming conservation of volume, momentum and gas flux across this zone. We denote the flow in the nozzle and downstream of the adjustment zone with the subscripts 0 and 1, respectively, leading to the relations:

$$(1 - C_0)\, b_0^2\, u_0 = (1 - C_1)\, b_1^2\, u_1 \tag{2.11}$$

$$(1 - C_0)\, b_0^2\, u_0^2 = (1 - C_1)\, b_1^2\, u_1^2 \tag{2.12}$$

$$C_0\, b_0^2\, u_0 = C_1\, b_1^2\, (u_1 - u_{slip}). \tag{2.13}$$

In section 2.6, we show that the predictions of this model, in which we assume rapid adjustment of the bubble speed on leaving the nozzle (equations 2.11 - 2.13), are within 3% of those of a more complete model, in which we allow the bubble speed relative to the liquid speed to adjust owing to the effects of both the bubble buoyancy and the drag between the bubble and the liquid. In this section, we now develop a model for the bubble fountain, assuming the bubble speed has value $u - u_{slip}$ beyond the nozzle.

In the experiments we did not observe significant re-entrainment of bubbles back into the descending fountain flow. Indeed, figure 2.4 (c) shows that most bubble traces extend all the way to the top of the image, indicating that after they have separated from the fountain, the bubbles rise to the surface and escape, rather then being re-entrained into the fountain core. To help understand these observations, in section 2.7 we calculate the trajectory of an air bubble which separates from the fountain at $z = H_F$ and $R(H_F) = b_{max}$, the outer radius of the fountain. As the bubble rises, it migrates inwards towards the fountain owing to the radial velocity field associated with the entrainment. However, the rise speed is so large that the bubbles only migrate a small radial distance prior to reaching the free surface, and hence are not re-entrained. Therefore, in the model of the fountain we assume the gas flux is independent of depth

$$\frac{d}{dz}(q_A) = 0. \tag{2.14}$$

The volume flux of water in the fountain continually increases with distance owing to the entrainment (cf. Morton et al. (1956))

$$\frac{d}{dz}(q_W) = 2\ \alpha\ m^{1/2} = 2\ \alpha\ b(z)\ u(z)\ \sqrt{1 - C(z)}. \tag{2.15}$$

Finally, the rate of change of momentum in the vertical direction can be expressed as

$$\frac{d}{dz}(m) = -\ g^{'}(z)\ b(z)^2 = -\ g\ C(z)\ b(z)^2 \tag{2.16}$$

where the minus sign is associated with the negative buoyancy force of the bubbles. It should be noted that our model applies to light fountains which initially propagate downwards. The model is strictly valid for the region in which $u(z) > u_{slip}$, so that the bubbles are carried down by the fountain. As we approach the point where $u(z) \rightarrow u_{slip}$, the bubbles will separate from the flow and the flux of air, q_A, rapidly decreases. Since we assume the bubbles all have a similar rise speed, we can use the model to estimate the maximum depth reached by the bubbles, by finding the point where $u(z) = u_{slip}$. As we approach this point, the model predicts that the radius diverges, since in the model the bubble flux is a constant (equation 2.14); in practice, the turbulent fluctuations lead to a range of depths around this height at which the bubbles actually separate, while the liquid phase of the fountain fluid carries on downwards beyond the point of separation (figure 2.2 (c)). In this context, it is worth noting that integral models of turbulent plumes and fountains often predict a divergence of the radius as the flow approaches the maximum distance from the source (Morton et al., 1956).

To proceed, it is useful to scale the momentum and water fluxes relative to their initial values, and the distance relative to the length-scale of the equivalent single-phase fountain, leading to the dimensionless variables

$$\hat{m} = \frac{m}{m_0} \qquad \hat{q} = \frac{q_w}{q_{w_0}} \qquad \hat{z} = z\frac{f_0^{1/2}}{m_0^{3/4}} = z\frac{(C_0\ b_0^2\ u_0\ g)^{1/2}}{m_0^{3/4}}. \tag{2.17}$$

Equation 2.14 implies that the gas flux and therefore the buoyancy flux, f_0, is a constant. The remaining two equations may be expressed in dimensionless form

$$\frac{d\hat{m}}{d\hat{z}} = \frac{-1}{Fr_0}\left(\frac{1}{\frac{\hat{m}}{\hat{q}} - \frac{1}{Fr_0}\Lambda}\right) \tag{2.18}$$

and

$$\frac{d\hat{q}}{d\hat{z}} = Fr_0\ 2\ \alpha\ \hat{m}^{1/2}. \tag{2.19}$$

These equations illustrate the influence on the flow of the source Froude number, Fr_0, and the ratio of bubble slip speed to characteristic fountain velocity, $\Lambda = u_{slip}/u_F$.

The only free parameter in the model is the entrainment coefficient, α. By comparison of the model prediction with the actual fountain penetration distance for each of the 126 experiments we have run, we find that the value α = 0.04 $\pm$ 0.004 minimises the Root-Mean-Square error,

$$e = \sqrt{\frac{1}{126}\sum_{n=1}^{126}(H_{Model}(i) - H_{Exp}(i))^2}, \tag{2.20}$$

where $H_{Model}(i)$ and $H_{Exp}(i)$ are the model prediction and the experimental observation of the maximum height reached by the bubbles for experiment i (see figure 2.7 (a), solid line). We have also calculated

$$e_2 = \frac{1}{126}\sum_{n=1}^{126}\frac{H_{Exp}(i) - H_{Model}(i)}{H_{Exp}(i)} \tag{2.21}$$

which corresponds to the mean value of the difference between the theoretical prediction of the bubble penetration distance and the experimentally observed bubble penetration distance, as a fraction of the experimental measurement, using the data from all our experiments. In figure 2.7 (a), e_2 is shown as a function of α with the dotted line. It is seen that $e_2 = 0$ when $\alpha = 0.04$ and that this value minimises the RMS error. In figure 2.7 (b) we illustrate the ratio of the experimentally measured bubble penetration depth and the theoretical prediction, plotted as a function of the source Froude number, Fr_0. For our set of 126 experiments we find a standard deviation of the bubble penetration distance, σ_{SD}, of 11.5% and a maximum difference between the data and the model prediction of approximately 30%. This estimate of the entrainment coefficient, α, is approximately one half of the entrainment coefficient found by Bloomfield and Kerr (2000) for single-phase fountains. We suggest this difference may be associated with the rising bubbles which act to suppress

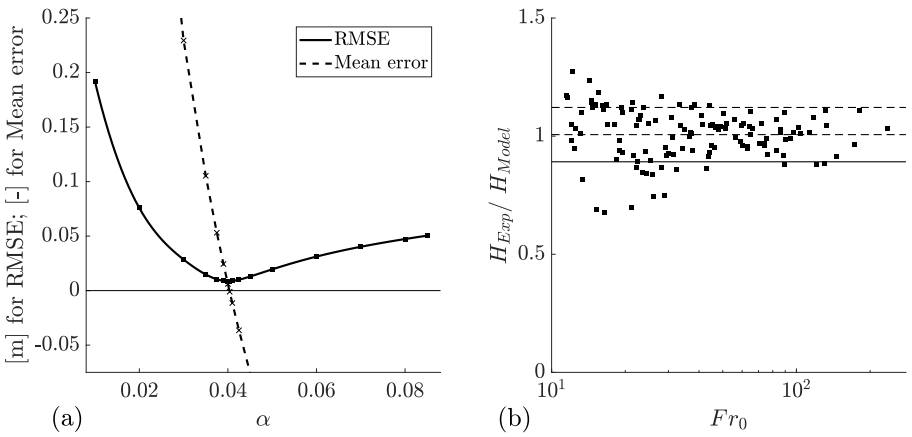

Fig. 2.7 (a) Root-Mean-Square error (RMSE, solid line) and the error in the prediction of the mean penetration distance as a fraction of the experimentally observed value (dashed line), as a function of the entrainment coefficient α. Both errors have their absolute minimum at $\alpha = 0.04$. (b) Comparison of experimental data and model prediction for the penetration depth of the bubbles, H_{Exp}/H_{Model}, as a function of source Froude number with a logarithmic scaling on the x-axis ($10 < Fr_0 < 240$) for an entrainment coefficient of $\alpha = 0.04$. The 126 data points have a mean value of 1.02 (shown as a solid horizontal line) with a standard deviation of 0.115 (shown as the two dashed horizontal lines). The maximum deviation between experimental measurement and model prediction is approximately 30%.

the formation of large-scale turbulent eddies which drive the entrainment. A similar effect was reported by Neto *et al.* (2016).

The structure of the fountain, as predicted by the non-dimensional model, is displayed in figure 2.8. The cartoon of the fountain in figure 2.3 (b) highlights that the fountain height is measured so that the downward direction is positive. The three panels in figure 2.8 show how the dimensionless momentum flux, volume flux and liquid velocity develop as one travels downwards through the fountain. All model solutions were obtained for $Fr_0 = 100$ and each plot contains three lines for $\Lambda = 0$, $\Lambda = 1$ and $\Lambda = 3$. Only when $\Lambda = 0$, does the momentum of the fountain fluid fall to zero as the fountain reaches its maximum depth. For $\Lambda > 0$, the momentum flux is still positive at the point at which the bubbles separate from the flow.

Figure 2.8 (b) highlights the importance of the entrainment of ambient water into the fountain. The liquid flux rapidly increases so that the fountain fluid is soon dominated by entrained liquid rather than the initial source fluid. The liquid velocity, plotted in figure 2.8 (c), rapidly decreases after leaving the nozzle

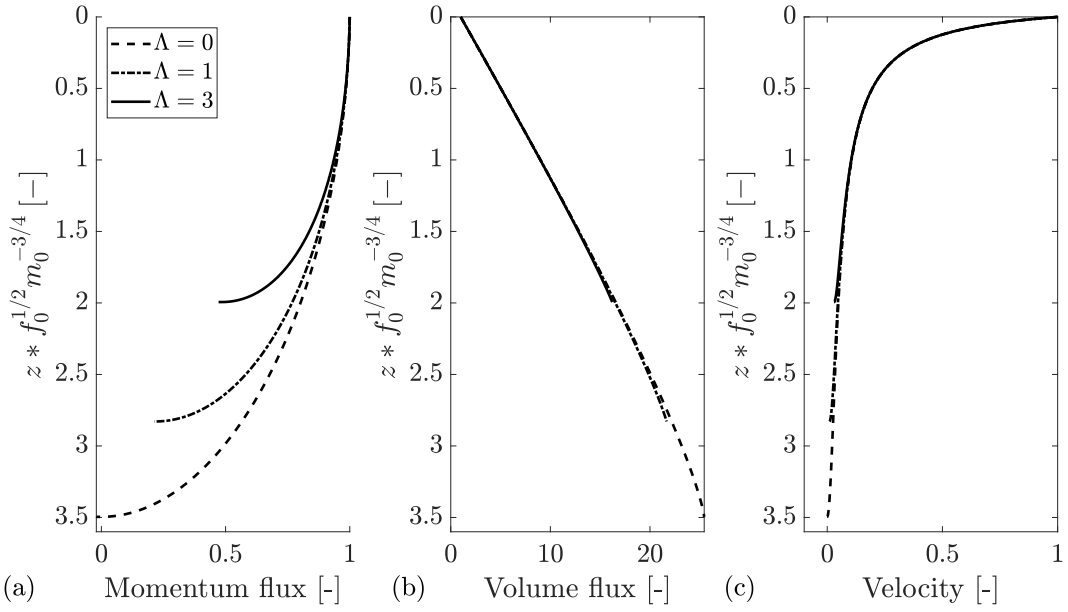

Fig. 2.8 Variation of the non-dimensional momentum flux (a); volume flux (b); velocity (c) as a function of the distance below the source. Curves are given for the parameter values $\Lambda = 0$ (dashed), $\Lambda = 1$ (dotted) and $\Lambda = 3$ (solid), and in this case for $Fr_0 = 100$.

but remains positive, except in the case $\Lambda = 0$. Solutions of the non-dimensional model presented in equations 2.18 and 2.19 also allow for an investigation of the influence of Fr_0 and Λ on the penetration depth of the bubbles. Figure 2.6 (b) shows that the experimental measurements of non-dimensional height decrease as Λ increases and Fr_0 decreases. This finding is consistent with the model predictions as seen in figure 2.9, which illustrates the predictions of the bubble penetration distance as a function of Λ for four different values of Fr_0 and compares these with our experimental measurements.

The three panels in figure 2.9 divide the experimental data into three sets of results: (a) a high Froude number range with $40 < Fr_0 < 240$, (b) an intermediate range with $20 < Fr_0 < 40$, and (c) all data points with $12 < Fr_0 < 20$. The lines represent the model predictions for source Froude numbers of 10, 20, 40 and 240. Figure 2.9 (a) shows that the majority of the data points for $Fr_0 > 40$ lie between the model solution for $Fr_0 = 40$ (blue line) and $Fr_0 = 240$ (green line). Similarly, the majority of the data points for the intermediate and low Fr_0 regimes also lie mostly between the lines delineating the model predictions for the bounding values of Fr_0. The error bars included in this graph reflect uncertainties in the source conditions: for

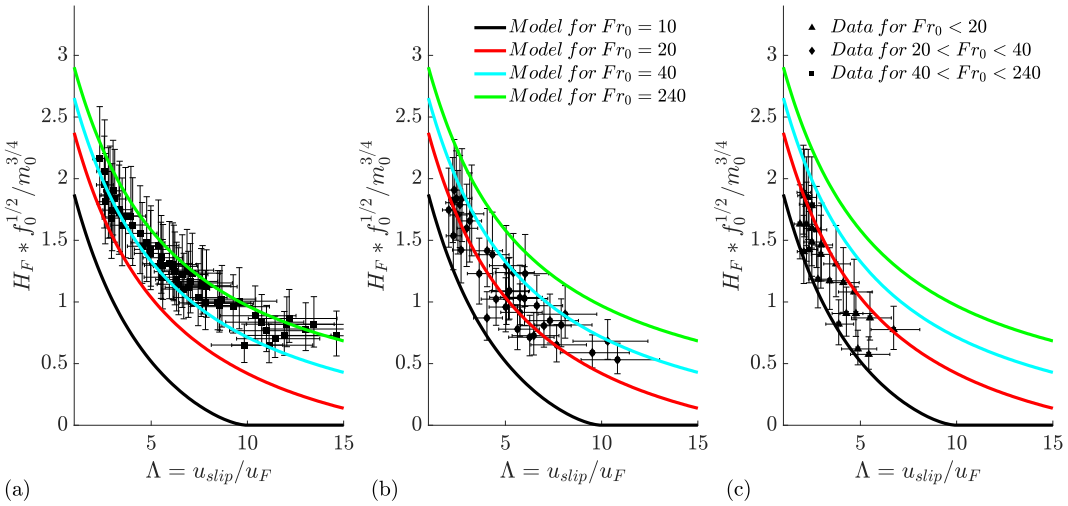

Fig. 2.9 Comparison of the theoretical model with the experimental data plotted as non-dimensional height as a function of $\Lambda = u_{slip}/u_F$. Each plot shows four model solutions for $Fr_0 = 10$, $Fr_0 = 20$, $Fr_0 = 40$ and $Fr_0 = 240$. Panel (a) contains all data points with $40 < Fr_0 < 240$. Similarly, (b) shows the experimental data for $20 < Fr_0 < 40$ and (c) contains the data points for $12 < Fr_0 < 20$.

our experimental system, the liquid flux is known to an accuracy of $\pm 5\%$ and the air flux is known to an accuracy of $\pm 10\%$.

2.5 Comparison with bubble fountains produced by plunging jets

In our experimental set-up, shown in figure 2.1, the nozzle is submerged in water and this allows for independent control of the air and the water flux at the source. However, turbulent bubble fountains in water are also produced when a pure downward propagating liquid jet enters the free surface of a tank of water. At the plunging point, the jet entrains air from the environment, producing a bubble fountain. A schematic of this set-up is shown in figure 2.11 (a). In this case, the amount of entrained air is a dependent parameter, controlled by d_0, L_J and u_0, the diameter, length and velocity of the plunging jet, respectively (Biń, 1993; Clanet and Lasheras, 1997).

Turbulent bubble fountains generated by plunging liquid jets are frequently employed in the process industry, for waste water treatment and for lake restoration (Biń, 1993). Clanet and Lasheras (1997) have investigated such

fountains and have proposed a model for the depth of penetration of bubbles entrained by such plunging water jets which takes the form

$$\frac{H_F}{2b_0} = \frac{1 + tan(12.5°)}{2\,tan(12.5°)} \frac{u_0}{u_{slip}}. \tag{2.22}$$

This model is very different to our new model for submerged bubble fountains (presented in section 2.4) as it does not account for the effects of buoyancy; the maximum bubble penetration depth is independent of the air flux, Q_{Air}. Clanet and Lasheras' model assumes a fixed spreading angle of 12.5° and a constant bubble slip velocity of $u_{slip} = 22\,\mathrm{cm/s}$. The only free parameters in equation 2.22 are the jet diameter and velocity, d_0 and u_0. As stated in section 2.2, the initial momentum flux in the water jet is $m_0 = b_0^2 u_0^2 = d_0^2 u_0^2/4$. Clanet and Lasheras' model, given by equation 2.22, can therefore be written in terms of m_0 according to the relation

$$H_F \approx 25\, b_0\, u_0 = 25\, m_0^{1/2} \tag{2.23}$$

This expression, which does not account for the effects of the gas phase, corresponds to the evolution of a simple single-phase jet, decelerating as it entrains ambient water. The equivalent entrainment coefficient would be 0.07. A simple decelerating jet would propagate over very long distances. Clanet and Lasheras, however, define the point at which the fountain liquid velocity matches the bubble rise speed as the point of maximum bubble penetration depth, $u(z_{max}) = u_{slip}$.

Clanet and Lasheras' model, expressed in simplified form in equation 2.23, depends only on the initial momentum flux. No account of the bubble buoyancy on the dynamics of the fountain is included. With our new experimental set-up with a submerged nozzle, however, we were able to vary the buoyancy flux for a given momentum flux. In figure 2.5, we clearly show that the maximum bubble penetration depth decreases for larger buoyancy fluxes at a constant initial momentum flux. We conducted this investigation for four initial momentum fluxes. For each momentum flux we produced fountains with four different gas fractions ranging from 10% to 80%, resulting in a total of 16 data points. The reduction in fountain height with increasing gas volume fraction is displayed in figure 2.10. The sloped lines describe the best linear fit through the bubble penetration distance measurements for a fixed source momentum flux. Clanet and Lasheras' model (equation 2.19) does not depend on the gas fraction and

therefore predicts a constant bubble penetration depth for a given momentum flux. This prediction is plotted as a short horizontal line at the intersection of the best-fit line and the model prediction. This point of intersection serves as a rough approximation for the gas flux entrained by the plunging jet experiments of Clanet and Lasheras (1997).

Even though Clanet and Lasheras' model neglects the influence of buoyancy on the maximum bubble penetration depth, their predictions are in very good agreement with their experimental data. A resolution of this seems to be that the model of Clanet and Lasheras implies an entrainment coefficient of about 0.07, which is much larger than we have determined for our model (section 2.4). The enhanced entrainment predicts a faster deceleration of the fountain and this compensates for the lack of the negative buoyancy force associated with the bubbles, which also acts to decelerate the fountain.

We can re-interpret the experimental data on the penetration depth of the bubble fountains produced by a plunging jet provided by Clanet and Lasheras (1997) using our new theoretical model. The liquid and momentum fluxes at the source are known as well as the measured bubble penetration depth. For each data point we can therefore find a gas flux so that the maximum bubble penetration distance predicted by our new model corresponds to the published fountain height measurement. Figure 2.11 illustrates the prediction of the ratio of the flux of entrained air as a fraction of the source liquid flow rate, Q_A/Q_{W_0}, as a function of the dimensionless parameter $\Omega = u_0^2/(gd_0)$, where d_0 is the nozzle diameter. Although there is no data on the actual gas flux in these specific plunging jets, we can nevertheless check if our predictions are consistent with empirical laws which have been published for the rate of entrainment of air into similar plunging jets. For example, we compare our results with two empirical relationships ((Van de Donk, 1981) (dashed line) and (Ohkawa et al., 1986) (solid line)) between the bubble penetration distance and the ratio of gas flux to liquid flux which are based on experimental measurements (Biń, 1993). Our estimates of the gas flux entrained into the plunging liquid jets reported by Clanet and Lasheras (1997) are consistent with these empirical relations; indeed the majority of our predictions fall between those of the two empirical models. This statement holds true for both the model presented in section 2.4 and for the model presented in section 2.6 which allows for an adjustment in bubble velocity. The predictions for the flux of entrained air of the two models agree to within 3%. We do note that some caution is required since there is a

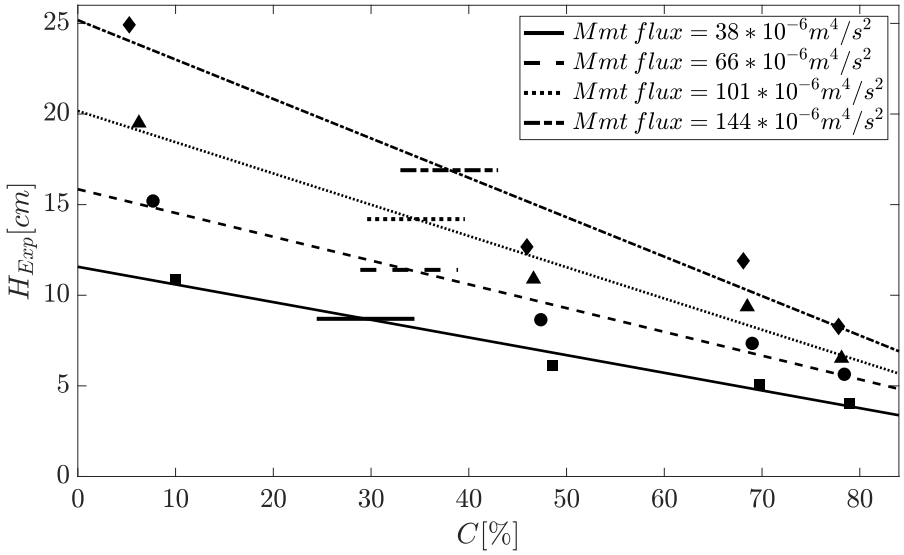

Fig. 2.10 Variation of the maximum bubble penetration depth for fountains with the same initial momentum flux. The source momentum flux was kept constant by fixing the liquid volume flux and adjusting nozzle diameter and air flux such that the source velocity, u_0, remains unchanged. Each of the sloped lines is a linear best-fit through four fountain height measurements at a constant momentum flux, $m_0 = q_{W_0} u_0$, but varying source gas fluxes. Increasing the source gas flux at a fixed momentum flux yields a reduction in bubble penetration depth. The dashed line (3rd line from the top) corresponds to the averaged fountain shapes shown in figure 2.5. The horizontal lines correspond to the height predicted by the model presented by Clanet and Lasheras (1997).

non-negligible difference between the two empirical models plotted in figure 2.11.

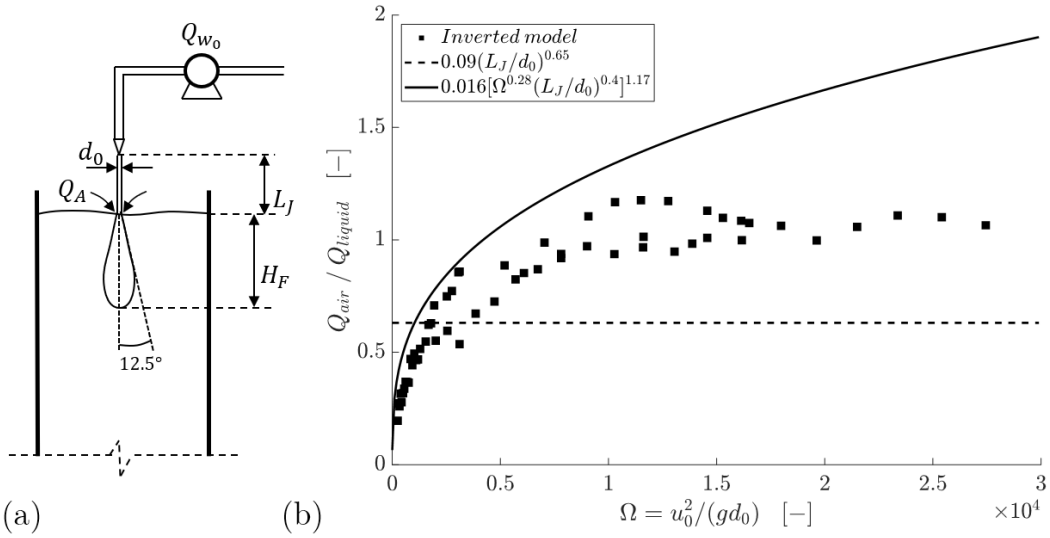

Fig. 2.11 (a) Schematic of a bubble fountain generated by a liquid jet plunging through a liquid surface. The curved arrows represent the air entrainment at the plunging point. For bubble fountains in water this air flux, Q_A, is fixed for a given jet diameter, d_0, jet length, L_J, and jet velocity, u_0. (b) The new theoretical model was applied to existing experimental data (Clanet and Lasheras, 1997) to calculate the amount of air entrained by plunging liquid jets based on the source momentum flux of the water jet and the maximum penetration depth of the resulting bubble fountain. The ratio of entrained gas to initial liquid flux, Q_A/Q_{W_0}, for these data points, shown as black squares, is plotted as a function of $\Omega = u_0^2/(gd_0)$. The data points are compared against empirical fits (Ohkawa et al., 1986; Van de Donk, 1981) to show that the new model can be used to calculate a first approximation of the entrained gas flux for plunging water jets.

2.6 Adjustment of the bubble velocity inside the fountain

The theoretical model presented in section 2.4 assumes that on exiting the nozzle and adjusting, the downward velocity of the gas phase, u_B, differs from the downward liquid velocity, u, by a constant equal to the bubble rise speed, $\Delta u = u - u_B = u_{slip} = 0.28\,\mathrm{m/s}$ (see equation 2.8). Inside the nozzle, however, we assume that the velocities of the gas and the liquid phase are equal in magnitude since the gas bubbles are observed to be of comparable radius to the radius of the nozzle (see equation 2.4). Our assumption that the gas bubbles rapidly decelerate until attaining the constant slip velocity, $\Delta u = u_{slip}$, is a simplification since the adjustment in bubble speed occurs over a finite adjustment length. We now show that provided this adjustment length is short compared to the length scale over which the momentum flux evolves, then this simplification does not have a large effect on the prediction of the maximum penetration distance of the bubbles in the fountain. The main effect of the bubble slip velocity on the motion of the fountain relates to its impact on the buoyancy force. Provided that the length scale over which the bubbles adjust to the terminal speed relative to the liquid is short compared to the length scale over which the buoyancy forces are important, then the buoyancy and momentum flux of the jet beyond the transition region is similar to that at the source. In this section, we explore this simplification in some detail. To this end, we introduce a further equation which accounts for the deceleration of the gas phase relative to the liquid

$$(\rho_{air}+\frac{1}{2}\rho_w)\frac{4}{3}\pi R_B^3\frac{d}{dt}(\Delta u) = \frac{4}{3}\pi R_B^3 g(\rho_w-\rho_{air})-C_D(Re_B)\pi R_B^2\frac{1}{2}\rho_w\Delta u^2. \quad (2.24)$$

The term in brackets on the left hand side accounts for the added mass effect owing to the displacement of ambient liquid around the bubble. The first term on the right-hand side is the buoyancy force experienced by a single bubble. The second term on the right-hand side provides a representation of the total drag on the bubble, where $C_D(Re_B)$ is the drag coefficient, R_B is the bubble radius and $\frac{d}{dt}(\Delta u)$ describes the bubble deceleration relative to the liquid velocity in the vertical direction. The bubble Reynolds number is defined in terms of the

liquid density, ρ_w, the relative speed of the fluid and bubbles, Δu, the fluid viscosity, μ_w, and the bubble diameter, d_B, according to the relation

$$Re_B = \frac{\rho_w \, \Delta u \, d_B}{\mu_w}. \tag{2.25}$$

The drag coefficient, C_D, is a function of the bubble Reynolds number and experimental measurements (Turton and Levenspiel, 1986) have been approximated by the empirical expression

$$C_D(Re_B) = \frac{24}{Re_B}(1 + 0.173 Re_B^{0.657}) + \frac{0.413}{1 + 16300 Re_B^{-1.09}}. \tag{2.26}$$

The time derivative in equation 2.24 can be transformed into a spatial derivative using the chain rule

$$\frac{d}{dt}(\Delta u) = u_B \frac{d}{dz_B}(\Delta u) \approx 2g^{'} - C_D(Re_B)\frac{3}{4\,R_B}\Delta u^2 \tag{2.27}$$

where z_B is the position of the bubble relative to the nozzle, and the vertical velocity of the bubble, $u_B(z)$, has an initial value of $u_B(0) = u_0$ and adjusts towards the value $u - u_{slip}$ when the bubble has travelled a distance of order Z_B^* from the nozzle. We can rewrite equation 2.27 in the form

$$\frac{d}{dz_B}(u) - \frac{d}{dz_B}(u_B) \approx \frac{2g^{'}}{u_B} - C_D(Re_B)\frac{3}{4\,R_B\,u_B}\Delta u^2. \tag{2.28}$$

By combining this equation with the equations for conservation of mass, momentum and buoyancy, we can find the variation of the velocity, buoyancy and radius of the fountain with distance from the source. Also the expression for the gas flux, equation 2.8, is generalised to the form

$$q_A(z) = \int_0^\infty \widetilde{C}(z,r)\; 2\; r\; \widetilde{u_B}(z,r)\; dr = C(z)\; b(z)^2\; u_B. \tag{2.29}$$

If we combine equation 2.28 with equations 2.9-2.16 we can then solve for the motion of the bubble fountain. In figure 2.12 we illustrate a series of predictions of the model presented in this section (solid lines) and we compare these with the predictions of the simplified model proposed in section 2.4 (dashed lines). In figure 2.12 (a), we show the prediction of the magnitude of the buoyancy force acting on a bubble (black line), the drag force acting on a bubble (red line), and the acceleration of the bubble (blue line). The buoyancy force is matched by the sum of the drag and the acceleration of the bubble (equation 2.24). Initially,

on leaving the nozzle, the dominant balance is between the buoyancy and the acceleration of the bubble. However, as the bubble speed adjusts in the first 10-20% of the total fountain height, the force balance becomes dominated by a balance between the buoyancy force and the drag and subsequently the bubble moves with the high Reynolds number near-constant slip velocity relative to the liquid. In panel (b), we illustrate the model prediction of the velocity of the fountain liquid (red and black) and the bubbles (blue) as a function of depth. It is seen that the more complete model presented in this section (solid blue line) leads to a delay in the deceleration of the bubbles compared to the approximate model in section 2.4 (dashed blue line). However, there is little difference in the predictions of the speed of the liquid in the fountain. Panel (c) illustrates the rapid increase in the bubble Reynolds number as the bubbles adjust to their slip speed in the upper 20% of the fountain. Panel (d) clarifies the evolution of the bubble slip speed (dashed line) with position in the jet, as given by a local balance between the buoyancy force and the drag, as well as the mean speed of the liquid (solid line), while panels (e) and (f) illustrate that the momentum flux and volume flux of the fountain, as predicted by the model presented in this section, is indistinguishable from the prediction of the simplified model given in section 2.4.

In figure 2.13 we compare the predictions of the bubble penetration depth as given by the model in this section (labelled H_{u_B}) and the simplified model of section 2.4 ($H_{u-u_{slip}}$). The data is plotted as a function of the source Froude number for the conditions pertaining in all 126 experiments reported herein. The difference between the predictions of the two models is less than 3%.

Figure 2.13 suggests that for the parameter space covered by our experiments, the model predictions for maximum bubble penetration depth are insensitive to the choice of initial gas phase velocity in the range from $\Delta u = 0$ to $\Delta u = u_{slip} = 0.28\,\mathrm{m/s}$. This results from the fact that the length over which the bubbles adjust to the liquid speed minus the high Reynolds number slip velocity is short compared to the length scale over which the buoyancy flux begins to influence the momentum flux of the fountain. Figure 2.8 illustrates the variation of the momentum flux, volume flux and velocity as a function of depth. The figure illustrates that on exiting the nozzle, the liquid velocity rapidly decreases, whereas the momentum flux in the vertical direction remains constant for the first 20% of the distance travelled by the fountain. In the parameter regime covered by the present experiments, the momentum flux

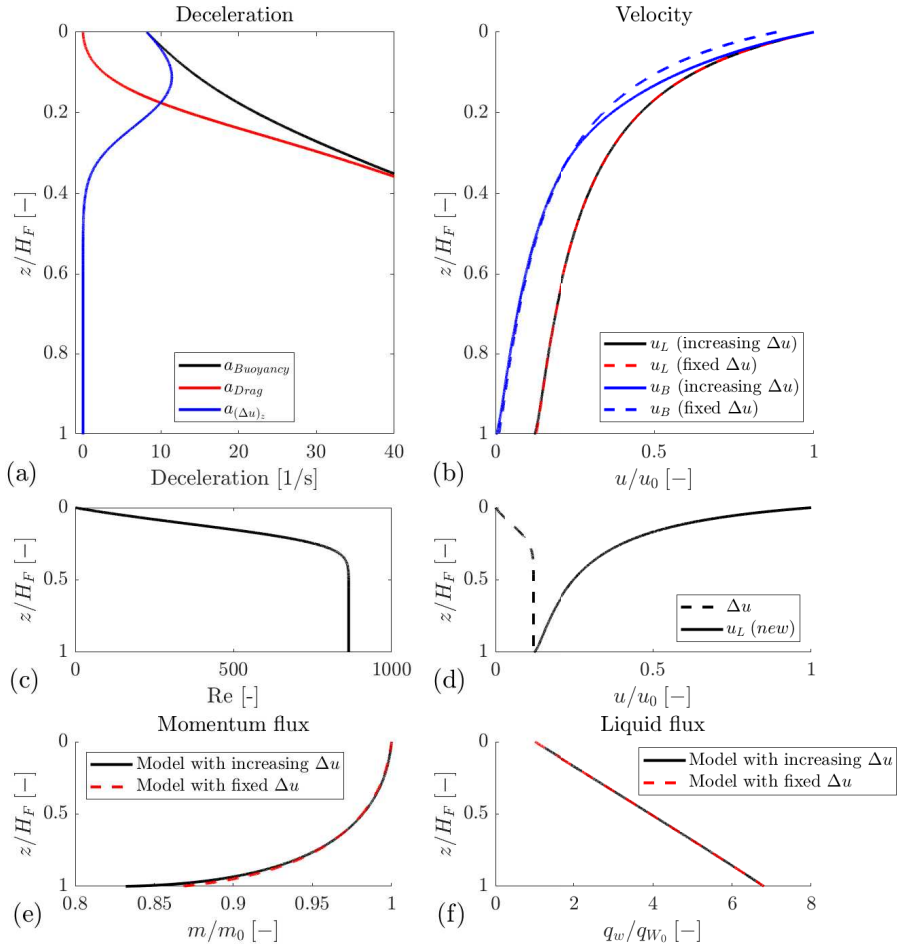

Fig. 2.12 (a) Illustration of the evolution of the three terms of equation 2.28 as a function of normalised distance from the source. Initially, the bubble decelerates owing to its buoyancy, but in steady state, the buoyancy is balanced by the turbulent drag. (b) Evolution of the liquid and bubble velocity plotted as a function of non-dimensional distance from the source. The dashed blue and red lines correspond to the predictions of the simplified model presented in section 2.4 of this chapter. The solid blue line illustrates a gradual deceleration of the bubble compared to the liquid (black line), as predicted by the model which accounts for the evolution of the bubble velocity relative to the liquid, presented in this section. (c) Plot of Reynolds number as a function of the dimensionless distance from the source, as predicted by the model of section 2.6. (d) Plot of normalised liquid velocity (solid line) and the difference between liquid and bubble velocity (dashed line) as a function of fountain height, as predicted by the model of section 2.6. (e) Evolution of momentum flux and (f) liquid flux as a function of distance from the source. The red line corresponds to the model in section 2.4 of this chapter and the black line shows the prediction of the model presented in section 2.6. For all panels, the source conditions correspond to experiment 1 in table 2.1 ($Fr_0 = 86$).

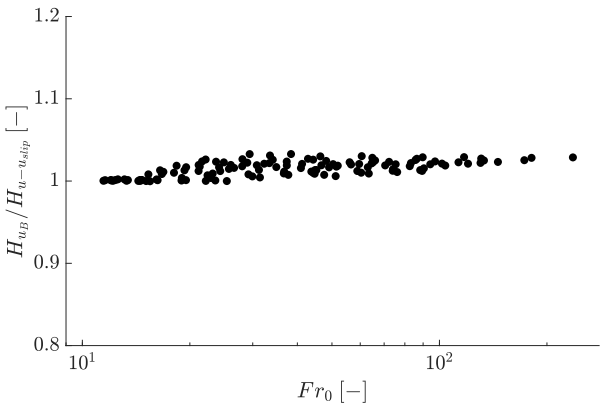

Fig. 2.13 Comparison of the model predictions of the maximum bubble penetration depth as predicted by the two models: H_{u_B} corresponds to the penetration depth predicted by the model of section 2.6, which allows the bubble speed relative to the liquid to vary with position, while $H_{u-u_{slip}}$ corresponds to the model presented in section 2.4 of this chapter, in which the bubble is assumed to have a constant slip velocity relative to the liquid. In the figure, the ratio of H_{u_B} to $H_{u-u_{slip}}$ is shown as a function of the source Froude number for the source conditions of all 126 experiments. The difference between the model predictions is somewhat larger for higher Froude numbers, but is always less than 3%.

of the fountain only begins to evolve once the bubbles have adjusted to a downward velocity corresponding to $u_B = u - u_{slip}$. We can show this more rigorously by comparing the length scales over which changes in bubble velocity, volume flux and momentum flux occur in dimensionless form. To identify scalings, some analysis of the governing equations is helpful. The right-hand side of equation 2.28 can be rewritten in terms of its characteristic roots, which are

$$\Delta u^*_{1,2} = \pm\sqrt{\frac{8g^{'}\,R_B}{3C_D(Re_B)}} \approx \pm\sqrt{\frac{8g\,R_B}{3C_D(Re_B)}}. \tag{2.30}$$

Since the density of air is very small compared to the density of water the effective buoyancy, $g^{'}$, is approximately equal to the acceleration due to gravity, $g^{'} \approx g$. Using these characteristic roots, equation 2.27 can be rewritten as

$$(u - \Delta u)\frac{d}{dz_B}(\Delta u) \approx \gamma(\Delta u - \Delta u^*_1)(\Delta u - \Delta u^*_2) \tag{2.31}$$

where $\gamma = \frac{3C_D(Re_B)}{4R_B}$. In our experiments the average bubble radius is about 1.5 mm, so that $\gamma \approx 500 C_D(Re_B)\,\mathrm{m}^{-1}$. The remaining two equations are

$$\frac{d(q_W)}{dz} = \frac{d}{dz}((1 - C(z))b(z)^2 u(z)) = 2\,\alpha\, m^{1/2} = 2\,\alpha\, b(z)\, u(z)\, \sqrt{1 - C(z)} \tag{2.32}$$

and

$$\frac{d(m)}{dz} = \frac{d}{dz}((1 - C(z))b(z)^2 u(z)^2) = -\,g^{'}(z)\, b(z)^2 = -\frac{f_0}{u_B}. \tag{2.33}$$

Scaling the drag coefficient with the value at high Reynolds numbers, C_{D_∞}, we can define a normalised drag coefficient, $\hat{C_D} = C_D(Re_B)/C_{D_\infty}$ for each value of Re_B. We proceed by scaling the vertical coordinate, z, by $\Gamma = 3C_{D_\infty}/(4R_B) \approx 250\,\mathrm{m}^{-1}$ so that $\hat{z} = z\Gamma$. The remaining dimensionless variables may be defined as

$$\hat{u} = \frac{u}{u_{slip}}; \qquad \hat{\Delta u} = \frac{\Delta u}{u_{slip}}; \qquad \hat{\hat{u}} = \frac{u}{u_0}; \qquad V = \frac{u_0}{u_{slip}}; \qquad \hat{u} = V\hat{\hat{u}}; \qquad \hat{b} = \frac{b}{b_0} \tag{2.34}$$

It is important to note that the right hand side of equation 2.30 can be expressed in the form

$$u_s(Re_B) = \sqrt{\frac{8g\,R_B}{3C_D(Re_B)}} = \sqrt{\frac{1}{\hat{C_D}}}\; u_{slip} \tag{2.35}$$

where the constant high Reynolds number bubble slip speed is

$$u_{slip} = \sqrt{\frac{8g\,R_B}{3C_{D_\infty}}}. \tag{2.36}$$

For our average observed bubble radius of 1.5 mm and a drag coefficient at high Reynolds numbers of $C_{D_\infty} \approx 0.5$ (Schlichting, 1979; Turton and Levenspiel, 1986) we find $u_{slip} = 0.28\,\mathrm{m/s}$. With these scalings, equations 2.31 to 2.33 can be written in dimensionless form as

$$\left(\hat{\hat{u}} - \frac{\hat{\Delta u}}{V}\right)\frac{d}{d\hat{z_B}}(\hat{\Delta u}) \approx \frac{1}{V}\left(\hat{\Delta u} - \frac{1}{\sqrt{\hat{C_D}}}\right)\left(\hat{\Delta u} + \frac{1}{\sqrt{\hat{C_D}}}\right) \tag{2.37}$$

$$\frac{d}{d\hat{z}}((1-C)\hat{b}^2\hat{u}) = \frac{2\,\alpha}{b_0\Gamma}\,\hat{b}\,\hat{u}\,\sqrt{1-C} \tag{2.38}$$

$$\left(\hat{u} - \frac{\hat{\Delta u}}{V}\right)\frac{d}{d\hat{z}}((1-C)\hat{b}^2\hat{u}^2) = -\frac{f_0}{V^3\,u_{slip}^3\,\Gamma\,b_0^2}. \tag{2.39}$$

In this form, the non-dimensional pre-factors on the right-hand side of each equation allow for a comparison of how quickly the bubble velocity, liquid flux and momentum flux adjust in the fountain. Equation 2.37 suggests that with $V >> 1$, the length scale for the adjustment of the bubble speed is given by $Z^*_{Bubble} = V$. The corresponding length scale for the adjustment of the momentum flux, as given by equation 2.39, is $Z^*_{mmt} = \frac{V^3\,u_{slip}^3\,\Gamma\,b_0^2}{f_0}$. Using the parameter values corresponding to our 126 experimental source conditions, we find $\frac{Z^*_{mmt}}{Z^*_{Bubble}}$ lies in the range 10-400 so we expect that the bubble speed adjusts to the speed of the liquid minus the rise speed of the bubbles long before the buoyancy force leads to a reduction in the momentum flux of the fountain. We infer that the simplified model presented in section 2.4 in which we assume that $u_B(z) = u(z) - u_{slip}$ provides a good approximate description of the experimental fountains discussed in this chapter.

It is of interest to note from equation 2.38, that the entrainment of ambient fluid into the fountain occurs over a length scale $Z^*_{Ent} = \frac{b_0\Gamma}{2\,\alpha}$. This is also small relative to the length scale over which the buoyancy forces influence the momentum flux in the fountain. This illustrates that, in the initial stages of the flow, the velocity decreases rapidly owing to the turbulent mixing, and this leads to the rapid drop in velocity seen in figure 2.8. However, the rate of entrainment is proportional to the product $u(z)\,b(z)\,\sqrt{1-C(z)}$ and this does not change across the transition region described by equations 2.11-2.13, so that the entrainment process is insensitive to the initial speed of the gas bubbles.

2.7 Validating the assumption that the rising bubbles are not re-entrained into the descending core

In equation 2.14, we assume that the gas flux, and hence the buoyancy flux, remains constant at all heights in the fountain. We now examine this approximation, which requires that the gas bubbles which separate from the fountain liquid at $z = H_F$ are not re-entrained during their ascent. The bubbles separate from the down-flowing liquid at the outer edge of the fountain, a distance $b(H_F) = b_{max}$ from the centre line, as shown by the cartoon in figure 2.14 (a). We have measured this maximum fountain radius in our experiments. The ratio of the maximum fountain radius, b_{max}, to the maximum bubble penetration depth, H_F, is plotted in figure 2.14 (b) as a function of Fr_0. This graph shows that the fountain radius decreases compared to the total fountain depth for larger Froude numbers. The colour-coding further suggests a decrease in the ratio of maximum fountain radius to fountain depth with Λ, highlighting that both Fr_0 and Λ are critical parameters controlling the fountain depth (see figure 2.6 (b)) as well as the fountain radius.

The entrainment of ambient fluid into the fountain draws the rising gas bubble towards the fountain core such that the distance of a rising bubble from the centre line, $R(z)$, decreases during the ascent from $R(z = H_F) = b_{max}$ to $R(z = 0)$. If $R(0)$ is larger than the initial fountain radius at the nozzle we can assume that the bubbles are not re-entrained (figure 2.14 (a)). The vertical bubble velocity corresponds to the bubble slip speed,

$$\frac{dz}{dt} = -u_{slip}. \tag{2.40}$$

Note the coordinate system to the left of figure 2.14 (a) which specifies that the vertical coordinate, z, is taken as positive downwards. The horizontal velocity component depends on the entrainment velocity into the fountain as well as the distance of the rising bubble from the edge of the fountain. The entrainment velocity can be written as

$$u_{ent}(z) = \alpha\, u(z)\, \sqrt{1 - C(z)} \tag{2.41}$$

(see equation 2.15). Assuming that the entrainment velocity in the ambient liquid is purely horizontal, then at radius $R(z) > b(z)$, the horizontal velocity component thus becomes

$$\frac{dR}{dt} = -u_{ent}(z)\,\frac{b(z)}{R(z)} = -\alpha\,u(z)\,\sqrt{1-C(z)}\,\frac{b(z)}{R(z)}. \tag{2.42}$$

We can combine equation 2.42 with equation 2.40 and this results in the integral relation

$$\frac{-\alpha}{u_{slip}}\int_{H_F}^{z} u(z)\,b(z)\,\sqrt{1-C(z)}\,dz = \int_{b_{max}}^{R(z)} R\,dR. \tag{2.43}$$

Equation 2.43 can be rewritten to give an expression for $R(z)$ in the form

$$R(z) = \sqrt{b_{max}^2 - \frac{2\alpha}{u_{slip}}\int_{H_F}^{z} u(z)\,b(z)\,\sqrt{1-C(z)}\,dz}. \tag{2.44}$$

The fountain liquid velocity, $u(z)$, the fountain radius, $b(z)$, and the gas fraction, $C(z)$, are all known from the fountain model (equations 2.8 - 2.10) so that the integral can be solved numerically. In order that the bubble is not re-entrained we require $R(z) > b(z)$ for $0 < z < H_F$. We have tested this condition for all 126 experiments we have conducted and found that in each case it holds. For example, in figure 2.14 (c) we illustrate the value $R(0) - b(0)$, for each experiment, as a function of the source Froude number.

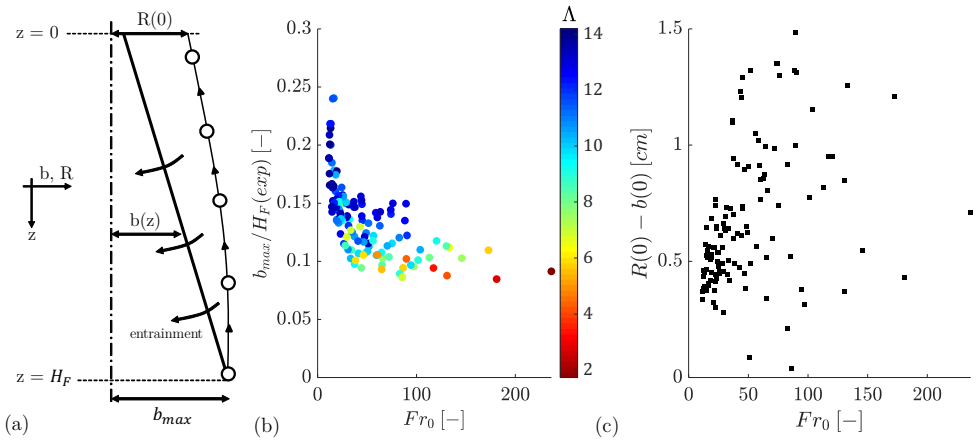

Fig. 2.14 (a) Cartoon illustrating the trajectory of a rising air bubble, separating from the fountain at $z = H_F$ and $b(H_F) = b_{max}$. The entrainment of ambient liquid into the fountain deflects the rising bubble towards the fountain core. The variable $R(z)$ denotes the distance of the rising air bubble from the centre line of the fountain, shown as the vertical dot-dashed line. (b) Experimentally determined ratio of maximum fountain radius, b_{max}, and bubble penetration depth, H_F, plotted as a function of the source Froude number. The colour-coding specifies Λ. (c) The distance of the gas bubble from the outer edge of the fountain at $z = 0$, $R(0) - b(0)$, plotted as a function of the Froude number.

2.8 Summary

We have studied the dynamics of turbulent bubble fountains in fresh water with a series of new experiments, complemented by a theoretical model based on conservation of the volume, momentum and buoyancy fluxes. We show that the penetration depth of the bubble fountains is controlled by the source Froude number, Fr_0, as well as Λ, the ratio of bubble rise speed to characteristic fountain velocity. The predictions of the model are consistent with our new experimental measurements of the penetration distance of the bubbles in the case of an entrainment coefficient $\alpha = 0.04 \pm 0.004$. Our model assumes that there is little re-entrainment of rising gas bubbles and this is motivated by the observation that the bubble rise speed is large compared to the entrainment velocity. We find that the bubbles separate from the fountain at the point where the liquid velocity matches the bubble rise speed and the liquid phase of the fountain fluid continues to travel downwards owing to its residual momentum. We further show that the new theoretical model can be applied to estimate the volume of air entrained by plunging water jets based on the observed bubble

penetration distance.

In the following chapter, we explore the behaviour of low Reynolds number bubble fountains in oil. We find that there is a range of bubble sizes and hence bubble rise velocities. In chapters 4 and 5 we consider the case where the ambient liquid lies in a confined space so that filling-box effects need to be considered (cf. Baines and Turner (1969)).

Chapter 3

Experimental study of low Reynolds number fountains

3.1 Abstract

We present an experimental investigation of low Reynolds number bubble fountains. These fountains are produced by issuing a mixture of air and oil downwards through a nozzle submerged in an oil-filled tank. Their source Froude numbers range from 5 to 100 with the source Reynolds number ranging between 10 and 80, indicating that the flow is not turbulent. The smallest bubbles observed in the experiments have diameters less than the pixel size of 0.2 mm, the largest bubbles have diameters of up to 1 cm.

Dye visualisation experiments suggest that bubbles with diameters of less than 1 mm do not separate from the fountain fluid, whereas the larger bubbles do separate from the flow. We find that the maximum depth reached by the smaller bubbles in these multiphase fountains agrees with the scaling observed for high Froude number single-phase fountains with comparable Reynolds numbers.

Experimental videos show that some of the smaller bubbles, carried upwards by the return flow associated with the fountain, accumulate at the free surface of the tank and form a bubble-rich layer which grows downwards into the tank. This layer eventually grows past the maximum fountain height and contaminates the entire tank. We hypothesize that the ratio of bubble rise speed to background flow velocity in the tank determines the threshold in bubble size below which all bubbles are carried to the bottom of the tank.

We confirm this hypothesis in the subsequent chapter where we present a quantitative investigation of multiphase fountains in confined spaces, motivated by the qualitative findings presented in this chapter.

3.2 Introduction

Our investigation of the penetration depth of low Reynolds number bubble fountains in oil builds on the work on turbulent bubble fountains in water presented in the previous chapter. We note that there are some crucial differences between bubble fountains in water and oil.

First, the source Reynolds number,

$$Re_0 = \frac{\rho u_0 b_0}{\mu} \tag{3.1}$$

is inversely proportional to the viscosity of the ambient liquid, μ. Here, ρ is the density of the liquid, u_0 the nozzle exit velocity, and b_0 the nozzle radius. In our experiments we chose the source conditions to be comparable to the parameters observed in lubrication systems of internal combustion engines. Accordingly, the nozzle diameters range from 3 to 5 mm, and the liquid flow rates through these nozzles are in the range from 5 to 20 ml/s. The oil used in the present experiments has a density of 890 kg/m^3 and a viscosity of 0.055 Pa s so that the source Reynolds numbers (cf. equation 3.1) are between 10 and 80, indicating that the flow is not turbulent. We therefore no longer assume turbulent entrainment of ambient fluid as we did in chapter 2 where the source Reynolds numbers were $O(1000)$.

Second, in our model of turbulent bubble fountains presented in the previous chapter, we assumed that the terminal rise velocity of air bubbles in water is constant for bubble diameters between 2 and 6 mm (Clift et al., 2005). However, this is not true for bubbles rising freely in oils. Haberman and Morton (1953) presented a detailed set of experiments on gas bubbles rising in a mineral oil with a density of 866 kg/m^3 and a viscosity of 0.058 Pa s, both values being comparable to the density and viscosity of the oil used in the present experiments. They investigate bubbles with diameters, d_B, between 0.4 and 40 mm and find that the terminal rise velocity increases with bubble size. For the smallest bubbles ($d_B = 0.4$ mm) they record a rise velocity of 0.25 cm/s. For bubbles with 2 mm diameter the rise speed increases to 4 cm/s and the

rise speed of bubbles with $d_B = 10$ mm increases to 20 cm/s. In the present experiments, the nozzle exit velocities are of the order of metres per second (cf. table 3.1), so that most bubbles are carried through the fountain.

In the previous chapter we illustrated that turbulent air-water fountains decelerate owing to (i) the turbulent entrainment of ambient liquid and (ii) the negative buoyancy force provided by the bubbles. We estimated the maximum bubble penetration depth as the distance from the source where the liquid velocity matches the constant terminal bubble rise speed of 28 cm/s. For comparison, in this chapter we quantify the maximum bubble penetration depth in terms of the source fluxes of buoyancy and momentum, and compare the results with classical single-phase fountain data. We further present experimental evidence that the smaller air bubbles do not separate from the liquid stream. The aim of this investigation is to improve our understanding of the dynamics of bubble fountains in viscous liquids.

In the second part of this chapter, from section 3.6 onwards, we discuss the experimental observation that some of the small bubbles carried upwards by the fountain do not have enough time to rise and escape through the free surface. Instead, these bubbles accumulate underneath the free surface and form a bubble rich layer which grows downwards into the tank. This bubble-rich layer changes the effective ambient of the fountain. This aeration of oil by bubble-laden fountains is also observed in the sump of internal combustion engines (Baran, 2007). The bubbles reduce the lubrication capabilities of the oil and introduce compressibility effects which may affect the hydraulic activation of valves (Nemoto et al., 1997).

3.3 Experimental method

Low Reynolds number bubble fountains are produced by issuing a mixture of oil and air downwards through a nozzle submerged by 5-10 cm in a tank filled with oil. The exact amount of oil that is supplied to the tank through the nozzle is removed at the bottom of the tank to ensure a steady reservoir level and to replicate the closed oil circulation system of internal combustion engines. The air is supplied from a pressurised air line. The Perspex tank is 40 cm high, with a width and depth of 20 cm. A light sheet was mounted to the back of the tank to provide uniform illumination. The apparatus is shown as a CAD-drawing in figure 3.1 (a) and a simplified schematic is shown in

panel (b). The air flux was controlled via a *Uniflux variable area* flowmeter and three round nozzles of diameter 2.9 mm, 3.84 mm and 5 mm are used as sources in the experiments. A *Watson Marlow* peristaltic pump is employed to circulate the oil. A $JAI\ SP-5000$ monochrome high-speed camera with a 1:28 *HAMA* lense is used to record high speed videos at a frame rate of 100 Hz for a duration of 10 s for the 48 experiments listed in table 3.1. This table lists two groups of experiments. The experiments above the horizontal line (M1-M12) form four sets of three experiments with the same source momentum flux, but different buoyancy fluxes. The experiments below the horizontal line (B1-B36) form 3 sets of 12 experiments with the same source buoyancy flux but varying momentum fluxes. Each experiment in table 3.1 was repeated three times and the parameters shown in the table correspond to the average values of the three runs.

The viscosity of the vegetable oil ($\mu_{oil} \approx 0.055\,\mathrm{Pa\,s}$) was measured with a *Kinexus* rheometer and the surface tension ($\sigma_{oil} \approx 0.032\,\mathrm{N/m}$) was measured via an optical method (*Kruss DSA 100*).

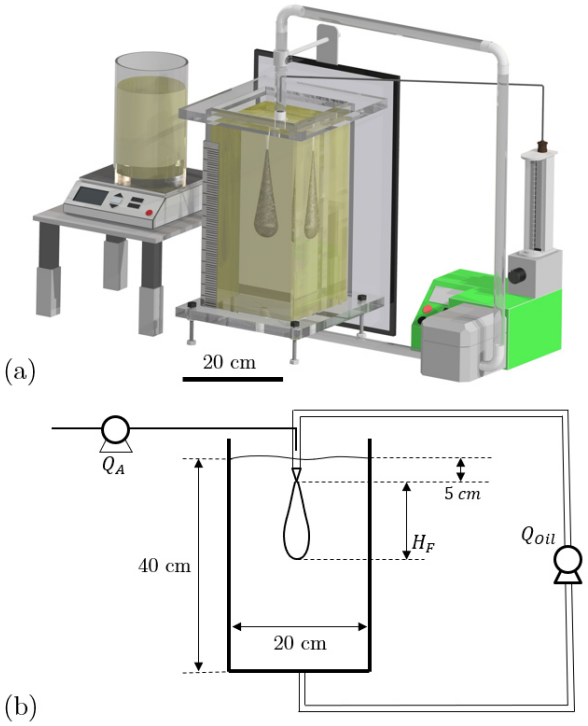

Fig. 3.1 (a) CAD model of the experimental apparatus. The peristaltic pump (green) issues oil through the nozzle at the top of the tank and simultaneously removes the same amount of liquid at the bottom to maintain a constant reservoir level. The air flow rate is controlled by a flowmeter (on top of the pump) connected to a pressurised air line. A light sheet is placed behind the tank to provide uniform illumination. (b) Schematic of the experimental apparatus. Labelled are the air flux, Q_A, the oil flux, Q_{oil}, the fountain height, H_F, and the dimensions of the tank.

Exp.	b_0 $[mm]$	Q_{oil} $[\frac{ml}{s}]$	Q_A $[\frac{ml}{s}]$	C_0 [%]	u_0 $[\frac{m}{s}]$	Fr_0	$H_F[cm]$	M_0e6 $[\frac{m^4}{s^2}]$	B_0e6 $[\frac{m^4}{s^3}]$
M1	1.45	7.50	0.83	10	1.26	33	5.51	9.46	8.175
M2	1.92	7.50	7.10	49	1.26	11	4.28	9.46	69.65
M3	2.50	7.50	17.3	70	1.26	7	4.34	9.46	169.4
M4	1.45	11.2	0.83	7	1.82	57	15.8	20.4	8.175
M5	1.92	11.2	9.89	47	1.82	17	7.13	20.4	97.04
M6	2.50	11.2	24.5	68	1.82	11	6.64	20.4	241.0
M7	1.45	14.8	0.83	5	2.37	85	19.1	35.0	8.175
M8	1.92	14.8	12.6	46	2.37	22	10.3	35.0	123.7
M9	2.50	14.8	31.7	68	2.37	14	9.15	35.0	310.7
M10	1.45	16.2	0.83	5	2.58	97	21.7	41.8	8.175
M11	1.92	16.2	13.7	46	2.58	24	11.7	41.8	134.1
M12	2.50	16.2	34.4	68	2.58	15	9.51	41.8	337.8
B1	1.45	7.50	0.83	10	1.26	33	5.43	9.46	8.175
B2	1.45	11.2	0.83	7	1.82	57	13.8	20.4	8.175
B3	1.45	14.8	0.83	5	2.37	85	20.7	35.0	8.175
B4	1.45	16.2	0.83	5	2.58	97	22.2	41.8	8.175
B5	1.92	7.50	0.83	10	0.72	16	3.14	5.40	8.175
B6	1.92	11.2	0.83	7	1.04	28	7.43	11.6	8.175
B7	1.92	14.8	0.83	5	1.35	42	10.7	20.0	8.175
B8	1.92	16.2	0.83	5	1.47	48	13.9	23.8	8.175
B9	2.50	7.50	0.83	10	0.42	8	1.46	3.18	8.175
B10	2.50	11.2	0.83	7	0.61	15	3.76	6.86	8.175
B11	2.50	14.8	0.83	5	0.80	22	6.78	11.8	8.175
B12	2.50	16.2	0.83	5	0.87	25	7.18	14.1	8.175
B13	1.45	7.50	3.33	31	1.64	23	5.77	12.3	32.70
B14	1.45	11.2	3.33	23	2.20	36	9.82	24.6	32.70
B15	1.45	14.8	3.33	18	2.75	51	14.7	40.6	32.70
B16	1.45	16.2	3.33	17	2.96	57	18.0	47.9	32.70
B17	1.92	7.50	3.33	31	0.94	11	3.89	7.02	32.70
B18	1.92	11.2	3.33	23	1.25	18	6.33	14.1	32.70
B19	1.92	14.8	3.33	18	1.57	25	10.4	23.2	32.70
B20	1.92	16.2	3.33	17	1.69	28	11.7	27.3	32.70
B21	2.50	7.50	3.33	31	0.55	6	3.26	4.14	32.70
B22	2.50	11.2	3.33	23	0.74	9	4.73	8.29	32.70
B23	2.50	14.8	3.33	18	0.92	13	6.72	13.7	32.70
B24	2.50	16.2	3.33	17	0.99	15	7.88	16.4	32.70
B25	1.45	7.50	20.0	73	4.16	30	7.06	31.2	196.2
B26	1.45	11.2	20.0	64	4.72	38	10.7	52.9	196.2
B27	1.45	14.8	20.0	57	5.27	47	13.6	78.0	196.2
B28	1.45	16.2	20.0	55	5.48	51	14.8	88.8	196.2
B29	1.92	7.50	20.0	73	2.37	15	5.14	17.8	196.2
B30	1.92	11.2	20.0	64	2.69	19	7.73	30.2	196.2
B31	1.92	14.8	20.0	57	3.00	23	10.0	44.5	196.2
B32	1.92	16.2	20.0	55	3.13	25	10.8	50.6	196.2
B33	2.50	7.50	20.0	73	1.40	8	4.21	10.5	196.2
B34	2.50	11.2	20.0	64	1.59	10	6.26	17.8	196.2
B35	2.50	14.8	20.0	57	1.77	12	8.36	26.2	196.2
B36	2.50	16.2	20.0	55	1.84	13	9.31	29.9	196.2

Table 3.1 Table specifying the range of source conditions for two sets of experiments on low Reynolds number bubble fountains. The experiments above the horizontal line form four sets of three experiments with the same source momentum flux. The experimental set below the horizontal line comprises of three sets of twelve experiments with constant source buoyancy flux. The table lists: Number of experiment ($Exp.$), nozzle radius (b_0), oil flux at the source (Q_{oil}), air flux at the source (Q_A), initial gas fraction (C_0), nozzle exit velocity (u_0), source Froude number (Fr_0), fountain height (H_F), source momentum flux (M_0), and source buoyancy flux (B_0). Each experiment was run three times and the listed fountain height, H_F, corresponds to the average value.

3.4 Experimental observations

An instantaneous image of a low Reynolds number bubble fountain in oil is shown in figure 3.2 (a). We identify individual bubbles as spheres of low light intensity. The smallest bubbles have diameters smaller than the width of an individual pixel ($d_B < 0.2\,mm$), while the largest bubbles have diameters of up to 1 cm. The maximum propagation depth of the bubbles for this particular fountain (experiment B14 in table 3.1) is just above 10 cm. The image in figure 3.2 (a) suggests that there is a distribution of bubble sizes in both the vertical and the horizontal direction. Smaller bubbles are carried deeper into the tank and further away from the fountain centre line compared to bubbles with larger diameters.

The time-averaged fountain shape is obtained by superimposing all 1000 instantaneous fountain images from the 10 s slow motion videos. An example of such an averaged fountain shape is shown in figure 3.2 (b) in false-colour. The colours in this figure represent a measure of the recorded light intensities. Dark regions, or bubble-rich zones, are shown in red, clear fluid is shown in blue. Panel (c) in figure 3.2 illustrates a time-series of a vertical line through the centre of the fountain in false-colour. This image suggests that on the fountain centre line the maximum bubble penetration depth oscillates around a mean value of approximately 10 cm. Such time-series images were employed to determine the maximum fountain depth for all experiments shown in table 3.1. Each experiment was run three times. The fountain heights quoted in table 3.1 correspond to the mean value of the three runs. The average deviation of fountain heights from this mean in the three runs was found to be 7%.

The first group of experiments (M1 to M12) consists of four sets of three experiments with the same source momentum flux but varying buoyancy fluxes. Owing to the negligible density of the air compared to the density of the oil, the momentum flux in the fountain is predominantly due to the oil flux,

$$M(z) = M_A(z) + M_{oil}(z) \approx M_{oil}(z) = Q_{oil}(z)u_{oil}(z), \tag{3.2}$$

where $M(z)$ is the total momentum flux, $M_A(z)$ the momentum flux of the air and $M_{oil}(z)$ the momentum flux carried by the oil. $Q_{oil}(z)$ is the volume flux of oil and $u_{oil}(z)$ is the oil velocity as a function of the vertical co-ordinate z. The total momentum flux at the source was kept constant by ensuring that both $Q_{oil}(0)$ and $u_{oil}(0)$ are fixed. The nozzle exit velocity is fixed by simultaneously

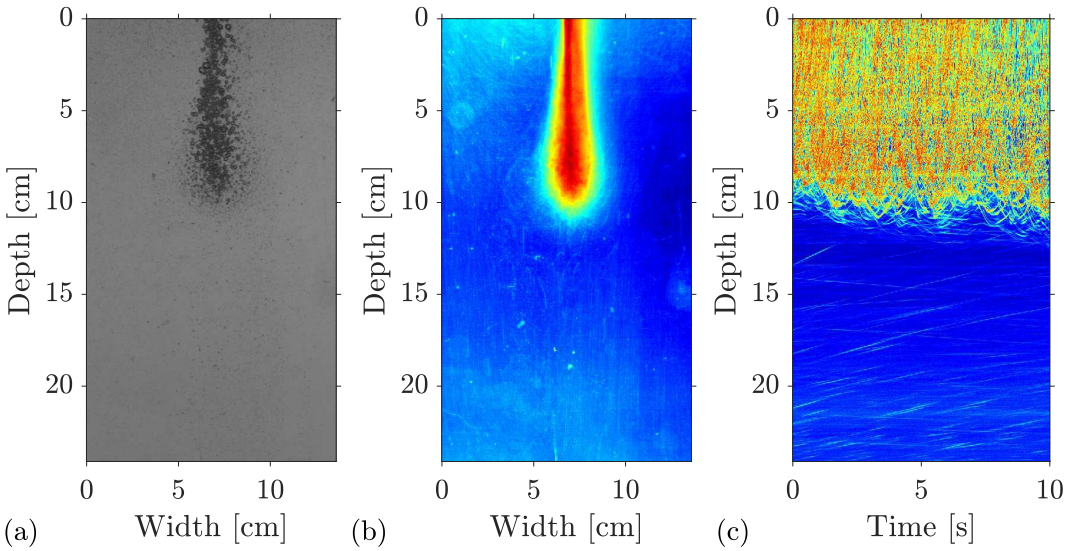

Fig. 3.2 Images from experiment B14 listed in table 3.1. (a) Single frame from the slow motion video showing an instantaneous fountain shape in which individual bubbles can be identified. We observe a distribution of bubble sizes. The largest bubbles are approximately 1 cm in diameter. The smallest bubbles are smaller than the pixel size of approximately 0.2 mm. The bubbles reach a maximum depth of approximately 10 cm. (b) False-colour image of the bubble fountain in which the colour denotes a time-averaged light intensity, obtained by superimposing 1000 instantaneous fountain shapes. (c) Time-series of a vertical line through the fountain centre shown in false-colour. Again, the colour is a measure of the recorded light intensity.

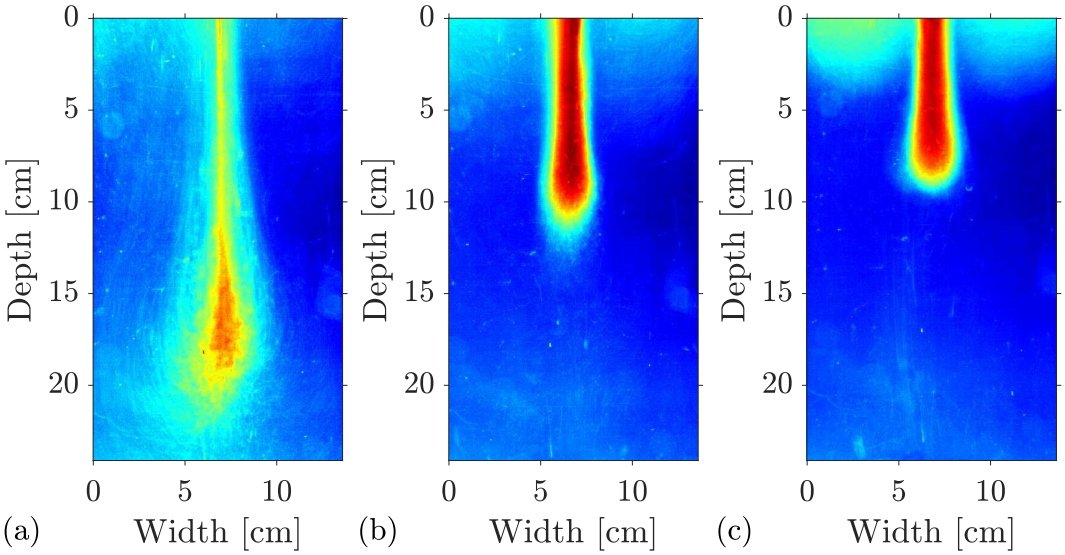

Fig. 3.3 False-colour images of the averaged fountain shapes of three fountains with the same source momentum flux. The source buoyancy flux increases from left to right with a volumetric gas concentrations at the source of (a) 5%, (b) 46%, and (c) 68%. The fountains correspond to experiments M7, M8 and M9 in table 3.1. As the buoyancy flux in the fountain increases, the fountain height reduces from approximately 20 cm in panel (a) to about 10 cm in panel (c).

increasing the nozzle radius and the air flux through the nozzle. As shown by equation 3.2, the total momentum flux is barely affected by an increase in air flux. However, the buoyancy flux in the fountain is directly proportional to the air flux, Q_A, so that

$$B(z) \approx gQ_A(z), \tag{3.3}$$

where g is the gravitational acceleration. Figure 3.3 shows the averaged shape of three bubble fountains in false-colour (experiments M7-M9) which all have the same source momentum flux, but the volumetric gas fraction at the source increases from 5% in panel (a) to 46% in panel (b) and 64% in panel (c). Owing to the associated increase in buoyancy flux, we observe a reduction in fountain height from over 20 cm in panel (a) to approximately 10 cm in panel (c). A similar trend was presented in the previous chapter on turbulent bubble fountains in water.

Similarly, we can investigate the effect of increasing the source momentum flux by keeping the source buoyancy flux constant. This is achieved by fixing Q_A whilst increasing Q_{oil}, and thus u_0, as both the air and the oil are issuing

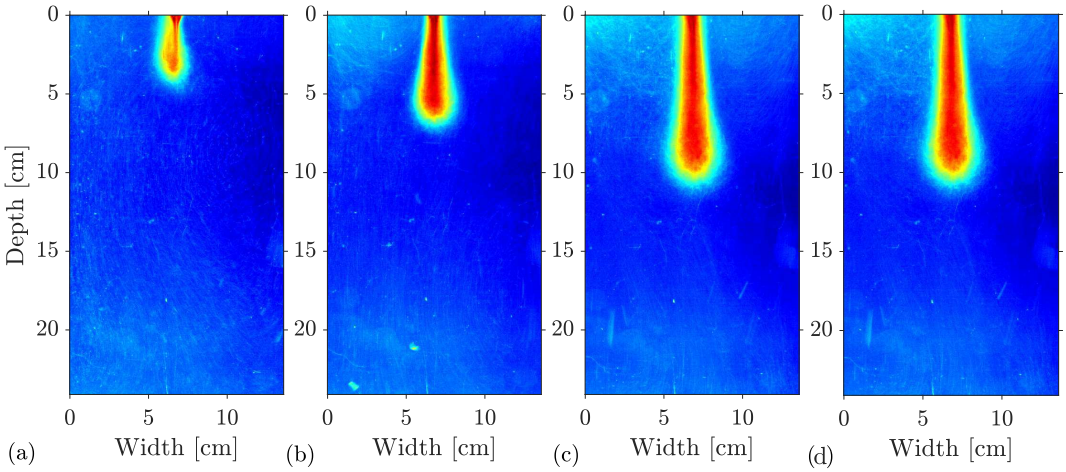

Fig. 3.4 False-colour images of the averaged fountain shapes of four fountains with the same source buoyancy flux. The source momentum flux increases from left to right. The fountains correspond to experiments B17, B18, B19 and B20 in table 3.1. As the momentum flux in the fountain increases, the fountain height increases from less than 5 cm in panel (a) to about 12 cm in panel (d).

through the same nozzle. Figure 3.4 shows false-colour images of the averaged fountain shape of four such fountains (experiments B17-B20 in table 3.1). We observe an increase in fountain height as the momentum flux at the source is increased. In panel (a), the fountain height is less than 5 cm, whereas in panel (d) is it approximately 12 cm. The light intensities of the false-colour images were adjusted to be in the range from 0 (no bubbles) to 1 (maximum bubble load) to maximise the contrast in the images. This implies that the colour intensities should not be compared across different panels as they do not represent equivalent grey-scales in the raw images. Additionally, these grey-scales do not provide a reliable measure of the bubble concentration since the light absorption is non-linearly related to bubble sizes and fountain depth. A calibration of light intensities in terms of the bubble load is therefore not possible.

In the present high-speed videos (cf. figure 3.2 (a)) we observe a range of bubble sizes in the oil-air fountains. In our investigation of turbulent bubble fountains in water (see previous chapter) we exploited the observation that most bubbles observed in water have diameters in the range 2 - 5 mm for all of which the rise speed is approximately 28 cm/s. We described that the flow in the fountain core of such water-air fountains decelerates owing to i) the entrainment of ambient liquid and ii) the negative buoyancy force provided by

the bubbles. We defined the maximum bubble penetration depth to be the point at which the water velocity matches the constant terminal bubble rise speed. At this depth, the bubbles separate from the fountain fluid and rise. The water, however, continues to propagate downwards. This observation is illustrated in figure 3.5 (a) and (c). Panel (a) shows a false-colour image of the averaged profile of a bubble fountain in water. The colour intensity is a measure of the light reflected from the bubbles. The source liquid (water) is not visible. In panel (c), however, the same air-water fountain is shown with dyed source liquid. The image illustrates that the water has some finite downward momentum flux at the point where the bubbles separate. The source liquid, water, continues to propagate downwards, past the point of bubble separation.

In the present low Reynolds number bubbles fountains, however, we do not observe this effect, as shown in panels (b) and (d) of figure 3.5. In panel (b) only the bubbles are visible to the camera, whereas in panel (d) the oil issuing through the nozzle has been dyed. Here, we observe that the source liquid does not propagate further than the bubbles and the bubbles do not separate from the flow. Instead, we observe that the small air bubbles trap all source liquid and carry it to the top of the tank. This observation is consistent with the findings of Mingotti and Woods (2016). They present a detailed investigation on the maximum height reached by particles in particle-laden fountains. They find that the ratio of terminal particle settling velocity to the characteristic fountain velocity,

$$\Lambda = \frac{u_{fall}}{u_F} \qquad \text{with} \qquad u_F = \frac{B_0^{1/2}}{M_0^{1/4}}, \tag{3.4}$$

determines if the particles separate from the flow ($\Lambda > 0.5$) or if the particle-laden fountain behaves like the equivalent single-phase fountain with the same source fluxes of buoyancy and momentum ($\Lambda < 0.5$). In the former case ($\Lambda > 0.5$) the source liquid continues to propagate in the direction of the initial momentum flux after the bubbles have separated. In the present experiments on oil-air fountains, all source liquid is returned upwards past the nozzle, as it is observed for single-phase fountains (cf. figure 3.5 (e)). The smaller bubbles ($d_B < 1\,\text{mm}$) remain in suspension with the liquid. The experimental videos, however, suggest that the larger bubbles ($d_B > 5\,\text{mm}$) do not reach the maximum height of the fountain, but separate from the flow at some fraction of the total fountain height. Bubble fountains in vegetable oil thus display

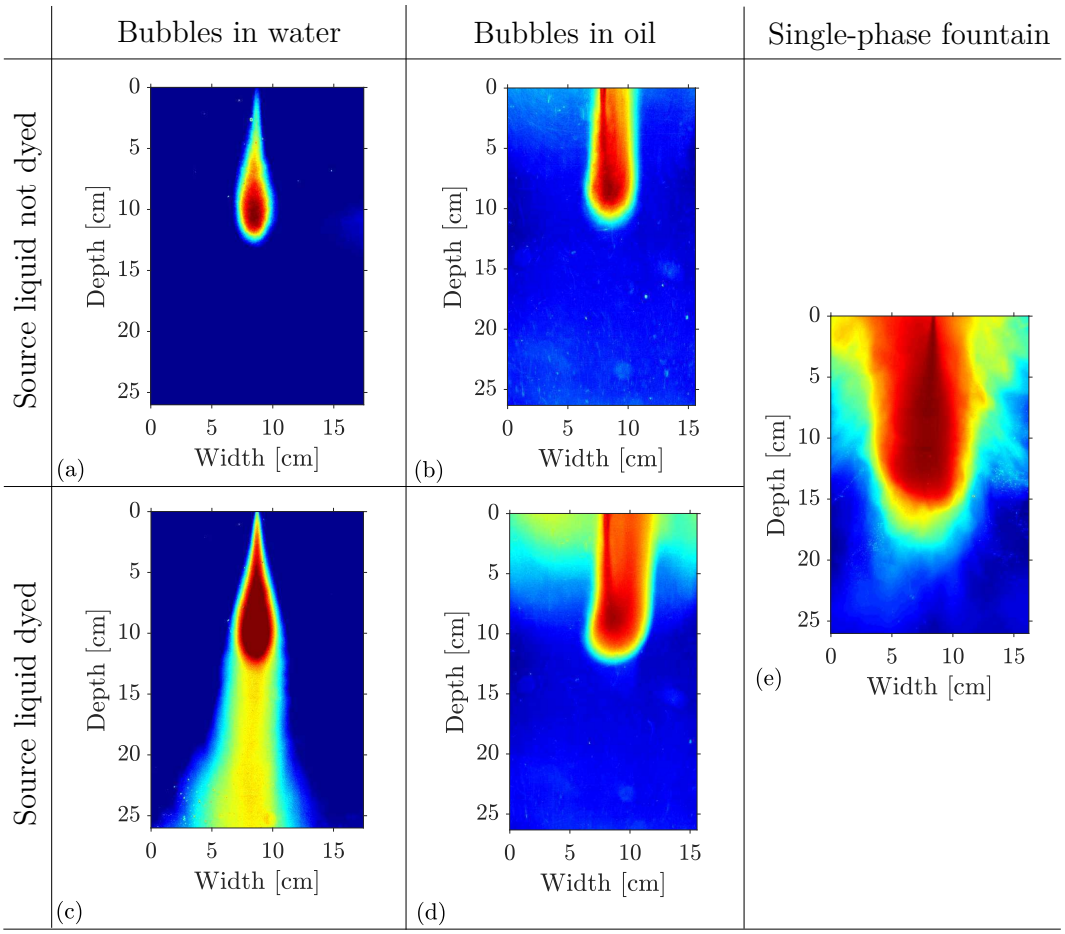

Fig. 3.5 Experimental investigation of the motion of the source liquid for bubble fountains in water, bubble fountains in oil, and single-phase fountains. Panels (a) and (c) show the time-averaged profile of a bubble fountain in water. In panel (a), only the bubbles are visible, in panel (c) dye has been added to visualise the source liquid. The source liquid continues to propagate downwards after the bubbles seperate from the flow and rise. Panels (b) and (d) show the time-averaged profile of a bubble fountain in vegetable oil. In panel (b), only the bubbles are visible, in panel (d) dye has been added to the source fluid. All the source fluid is trapped by the bubbles and carried upwards after the bubbles have reached their maximum depth. Panel (e) shows an image of the averaged shape of a single-phase fountain (fresh water injected downwards into salty water) for comparison. All images are shown in false-colour.

features of both separated flow (large bubbles) and single-phase flow (small bubbles). In the present experiments, the nozzle exit velocity of the oil is of the order of metres per second and far exceeds the bubble slip velocities, which are of the order of centimetres per second. This suggests that most of the air bubbles with $d_B < 5\,\mathrm{mm}$ are carried all the way through the fountain.

Owing to the range of bubble sizes and the non-turbulent nature of these fountains, it is difficult to capture the detailed physics of this problem in a simple theoretical model. However, we can investigate the scalings for the steady-state height of these fountains in terms of their source fluxes of buoyancy and momentum, as well as the dependency on the source Reynolds number.

3.5 Scalings of the experimental data

The steady-state rise height of axisymmetric fountains is independent of the source Reynolds number, Re_0, if the fountain flow is fully turbulent, and if the source Froude number,

$$Fr_0 = \frac{u_0}{\sqrt{b_0 g_0'}}, \tag{3.5}$$

is larger than 1. b_0 is the nozzle radius, u_0 the nozzle exit velocity, and g_0' is the reduced gravity at the source (Hunt and Burridge, 2015; Turner, 1966). Based on experimental data, the steady-state rise height of these turbulent single-phase fountains, H_F, may be expressed in terms of the source fluxes of buoyancy and momentum so that

$$H_F = 2.46(M_0/\pi)^{3/4}(|B_0|/\pi)^{-1/2} = 2.46 b_0 Fr_0. \tag{3.6}$$

In figure 3.6 we plot the dimensionless fountain height, H_F/b_0, as a function of the source Froude number. In this figure, the red data points correspond to the measurements presented by Hunt and Burridge (2015) for single-phase turbulent fountains, and the red line, providing the best fit for the experimental data, has a gradient of 2.46. The black data points correspond to our measurements of maximum bubble penetration depth in low Reynolds number oil-air fountains, and the error bars represent the maximum deviation of our measurements of H_F from the averaged value over three experiments. The observed scatter in our experiments is comparable to that in the single-phase fountain data. Fitting

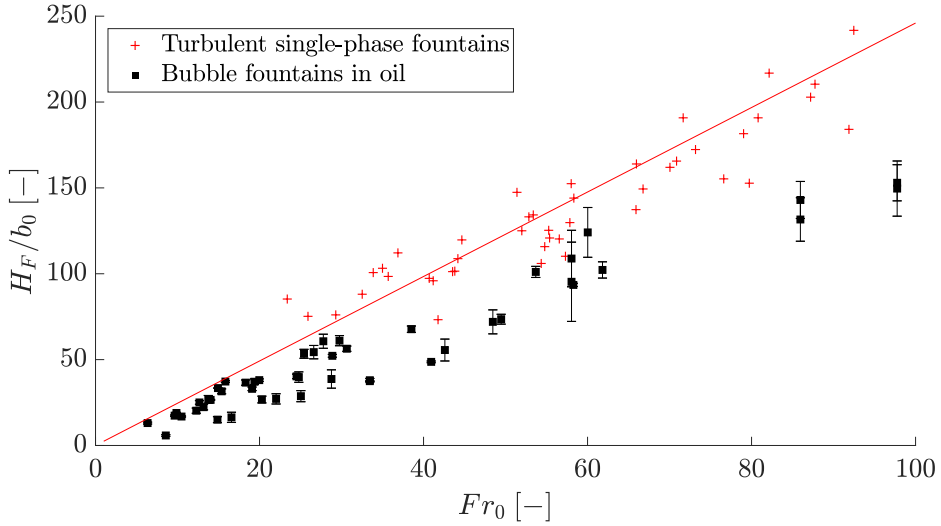

Fig. 3.6 Measured maximum bubble penetration depth, normalised by the source radius, H_F/b_0, plotted as a function of the source Froude number, Fr_0. The black squares represent the measurements of the 48 experiments listed in table 3.1. The red crosses correspond to measurements of turbulent single-phase fountains published by Hunt and Burridge (2015). The red line corresponds to the scaling $H_F = 2.46\, Fr_0 b_0$.

a straight line through our data suggests that $H_F \approx 1.5 Fr_0 b_0$ (cf. equation (3.6) for single-phase fountains), suggesting that our oil-air fountains have a lower steady-state height compared to single-phase fountains with the same source buoyancy and momentum fluxes.

The empirical relation of equation 3.6 is valid for turbulent single-phase fountains and is independent of the source Reynolds number. Williamson et al. (2008) investigated the effect of both the source Froude number and the source Reynolds number on low Reynolds number fountains, and they provide a regime map for $0.7 < Fr_0 < 100$ and $15 < Re_0 < 1900$. This regime diagram (figure 2 of their paper) provides an overview of a range of complicated observations including flopping, circling, bobbing and jet instabilities exhibited by low Reynolds number fountains. The regime map further divides the Reynolds number space into a laminar region ($Re_0 < 120$), a transitional region ($120 < Re_0 < 2000$), and a fully turbulent region, ($Re_0 > 2000$). In figure 3.7 we plot the Fr_0-Re_0-regime diagram for the present set of experiments on bubble-laden oil fountains, including the three distinct Reynolds number regimes (see above). We note that according to the definition of Williamson

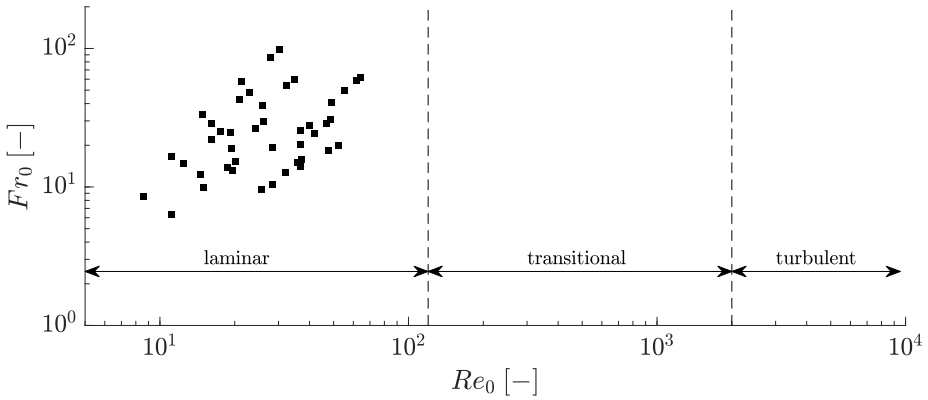

Fig. 3.7 Regime diagram of the Froude number and Reynolds number space covered by the present experiments (black squares). The dashed vertical lines delimit the Reynolds number regimes identified by Williamson et al. (2008).

et al. (2008), the present experimental data is in the large Froude number space ($Fr_0 > 1$), and covers the laminar Reynolds number space ($Re_0 < 120$).

The behaviour of single-phase fountains in this low Reynolds number and high Froude number space is complex and various empirical fits have been developed to improve our understanding of these flows. The investigations by Williamson et al. (2008) and Burridge et al. (2015) suggest that for large Froude numbers ($Fr_0 > 1$) and low Reynolds numbers ($Re_0 < 120$) the mean steady-state fountain height of single-phase fountains scales according to the purely empirical law

$$H_F = 0.34 b_0 Fr_0 Re_0^{1/2}. \tag{3.7}$$

The scaling of equation 3.7 is compared with the present data on low-Reynolds number bubble fountains in figure 3.8. The dashed line has a gradient of 0.34. The data points represent our data, the colour-coding corresponds to the nozzle exit velocity. A large nozzle exit velocity indicates large volume fluxes of both oil and air, as well as large fountain heights. The experimental data is in good agreement with the dashed line of gradient 0.34, based on low Reynolds number single-phase fountain data. The colour-coding of the outliers suggests that these four data points, shown in red, have large nozzle exit velocities, partially owing to a very high gas fraction at the source. The rise height of these fountains is less than the rise height of analogous single-phase

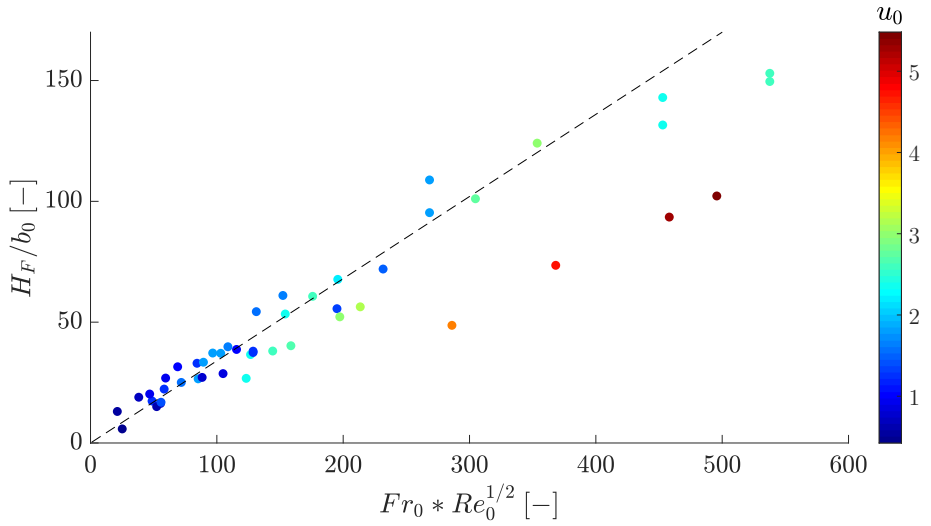

Fig. 3.8 Scaling of the dimensionless steady-state fountain height for low Reynolds number fountains (Burridge et al., 2015; Williamson et al., 2008). The dashed line represents equation 3.7. The colour-coding corresponds to the nozzle exit velocity.

fountains. This is likely to be a consequence of the reversal of bubble motion within the fountains, disturbing the down-flow in the fountain core.

Burridge et al. (2015) have found that for large Froude number fountains the steady-state fountain height, H_F, is independent of the source Reynolds number only when the source Reynolds number exceeds 1000. This is indeed the case for bubble fountains in water presented in the previous chapter, but the rise height of the present low Reynolds number bubble fountains does depend on the source Reynolds number, as shown in figure 3.8.

3.6 The filling-box observation

The experimental investigation presented in the previous section is based on slow motion videos, recorded for a duration of 10 seconds with a frame rate of 100 images per seconds. During these experiments we observed that some of the smaller bubbles ($d_B < 1\,\mathrm{mm}$) do not immediately escape at the free surface of the tank. Instead, they accumulate underneath the free surface and form a bubble-rich layer that grows downwards into the tank. To gain an understanding of this process, we ran 12 additional experiments, 60 minutes in length at a frame rate of one image per second. The source conditions of these experiments are listed in table 3.2. In each experiment, we stop the flow

Exp.	b_0 $[mm]$	Q_{oil} $[\frac{ml}{s}]$	Q_A $[\frac{ml}{s}]$	C_0 [%]	u_0 $[\frac{m}{s}]$	Fr_0
FB1	1.45	7.50	10	57	2.65	29
FB2	1.45	7.50	20	73	4.16	41
FB3	1.45	16.2	10	38	3.97	54
FB4	1.45	16.2	20	55	5.48	62
FB5	1.92	7.50	10	57	1.51	15
FB6	1.92	7.50	20	73	2.37	20
FB7	1.92	16.2	10	38	2.26	27
FB8	1.92	16.2	20	55	3.13	31
FB9	2.50	7.50	10	57	0.89	8
FB10	2.50	7.50	20	73	1.40	11
FB11	2.50	16.2	10	38	1.33	14
FB12	2.50	16.2	20	55	1.84	16

Table 3.2 Table specifying the range of source conditions for experiments on bubble fountains in oil, run for a duration of 60 minutes, to investigate the formation of a bubble-rich layer that grows from the free surface into the tank. The table lists: Number of experiment ($Exp.$), nozzle radius (b_0), oil flux at the source (Q_{oil}), air flux at the source (Q_A), initial gas fraction at the source (C_0), nozzle exit velocity (u_0) and source Froude number (Fr_0).

through the nozzle and through the extraction vent at the bottom of the tank after 30 minutes, so that the bubbles are allowed to rise freely.

The cartoon in figure 3.9 illustrates the formation and downward propagation of the bubble-rich layer in panels (a) to (c). Larger bubbles escape close to the protruding nozzle, whereas smaller bubbles spread horizontally underneath the free surface, feeding a bubble rich layer. Eventually, the bubble layer grows past the fountain height. Panel (d) of figure 3.9 illustrates the rise of the bubble front during the second half of each experiment. The horizontal dashed line in panels (a) to (d) marks the depth of the bubble front.

In our experimental investigation, we track the position of this bubble front as a function of time (cf. figure 3.11). The schematic in panel (e) of figure 3.9 provides a simplified illustration of the propagation of this bubble-rich layer, shaded in grey. The capital letters (A-D) link panels (a) to (d) to this time-series cartoon. We identify three regimes:

Regime 1 (fast filling): Initially, we observe a fast propagation speed of the bubble front up to the depth reached by the fountain.

Regime 2 (slow filling): Once the bubble front surpasses the depth of the fountain, the propagation velocity of the front reduces. We hypothesize that the constant downward velocity of the front in this regime, u_{layer}, is determined by a balance of the background flow velocity, u_{BG}, and the bubble rise velocity, u_{rise}, as indicated on the cartoon. The background flow velocity in the tank,

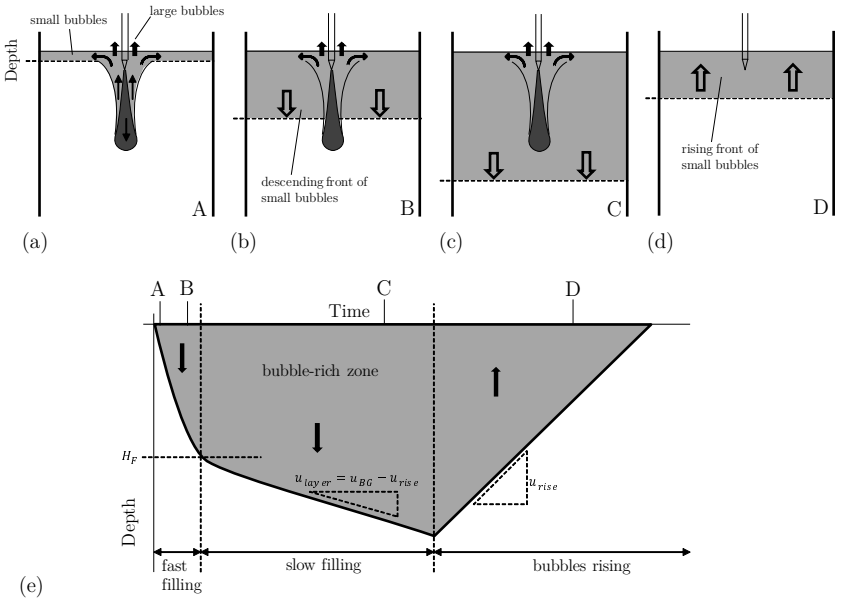

Fig. 3.9 Cartoon of the formation of a bubble-rich layer underneath the oil-air interface (panels (a) to (c)), followed by the rise of the bubbles after the circulating flow is turned off (panel (d)). Panel (e) illustrates a time series of the propagation of the bubble front, highlighting three regimes. The capital letters link this figure to figures 3.10 and 3.11.

u_{BG}, is equal to the ratio of source oil flux and the cross-sectional area of the tank,

$$u_{BG} = \frac{Q_{oil}}{A}, \tag{3.8}$$

where A is approximately $0.04\,\mathrm{m}^2$ so that the propagation speed of the bubble front below the depth of the fountain is given by

$$u_{layer} = u_{BG} - u_{rise}. \tag{3.9}$$

Regime 3 (bubbles rising): With the fountain flow switched off, the bubbles rise to the free surface and leave the tank. The slope of the contours in the time-series image in this third regime corresponds to the bubble rise speed, u_{rise}.

Figure 3.10 contains four images extracted from the 60 minute slow motion video of experiment FB3 (see table 3.2) at different times. The four panels correspond to the four cartoons in figure 3.9. The first image in panel (a) (marked with a capital A to link to figures 3.9 and 3.11) shows the initial bubble

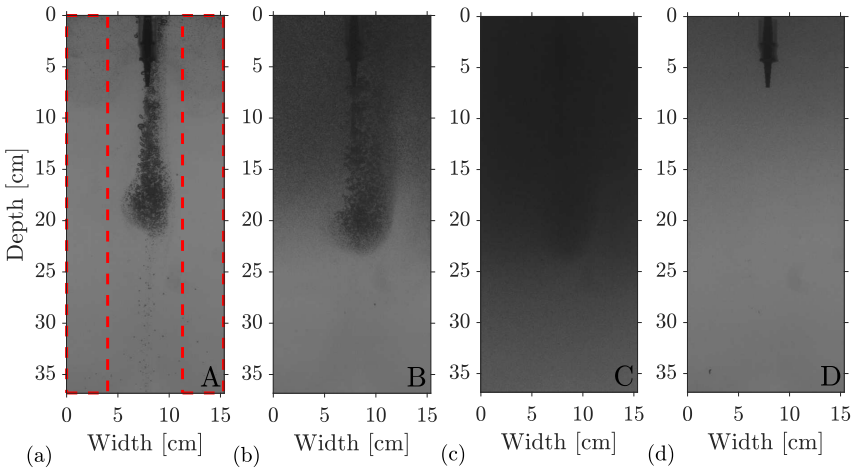

Fig. 3.10 Instantaneous images of low Reynolds number bubble fountains (experiment FB3 in table 3.2) after (a) 1 s, (b) 100 s, (c) 28 min and (d) 50 min. Small bubbles accumulate at the top and form a bubble-rich layer which grows downwards into the tank. After 30 min the bubble fountain is turned off and the bubbles rise back to the free surface. The two red rectangles in panel (a) mark the zone over which a horizontal average was taken to plot the time-series image in figure 3.11.

fountain in a clear and uncontaminated environment. Two red rectangles have been added to this image to illustrate the region that we refer to when discussing the environment. The nozzle protrudes approximately 7 cm into the tank.

The second panel (marked B) shows the fountain after approximately 100 seconds. The environment close to the free surface (at a depth of 0 cm) is much darker compared to panel (a), owing to the accumulation of small bubbles in this zone. The bubble-rich region grows into the tank as time progresses, as shown in the image of panel (c), extracted after about 28 minutes.

After 30 minutes we stop all flow through the nozzle and through the extraction vent at the bottom of the tank and the bubbles are allowed to rise freely. Panel (d) of figure 3.10 shows the contaminated ambient (without any fountain) after 50 minutes - or 20 minutes after the fountain has been turned off. The image is brighter compared to panel (c), indicating that a large fraction of bubbles has escaped through the free surface at the top of the tank.

To visualise the accumulation of bubbles underneath the free surface and the subsequent growth of the bubble-rich layer downwards into the tank, we compute the horizontally-averaged light intensity of the background (highlighted by the two red rectangles in figure 3.10 (a)) as a function of time. Two of these horizontally-averaged time-series images are shown in figure 3.11, obtained

for experiments FB1 (a) and FB3 (b). The time-series image shown in panel (b) corresponds to the experimental images displayed in figure 3.10. The four vertical lines marked by capital letters link the image in figure 3.11 to figures 3.9 and 3.10. The interface between the clear fluid (blue colour) and the bubble-laden fluid (red colour) corresponds to the location of the bubble front, highlighted by the dashed horizontal lines in figure 3.9.

Two horizontal lines were added to the panels in figure 3.11. The upper blue horizontal line at a depth of 7 cm marks the position of the nozzle outlet. The lower red line marks the initial height of the oil-air fountain. In both panels in figure 3.11 the tank is initially clear and the horizontally-averaged background light intensity thus shows a vertical blue column of pixels at time zero. Subsequently, we observe the growth of the bubble-rich layer downwards into the tank, as illustrated by the cartoon in figure 3.9 (d). Red colour denotes a high concentration of bubbles. In panel (a), obtained for experiment FB1, the bubble-rich layer quickly fills the tank up to the depth reached by the fountain. The filling-box velocity of the bubble-rich layer reduces considerably in the region below the fountain.

In panel (b), obtained for experiment FB3, we double the source flux of oil. This results in a much faster propagation speed of the bubble front in the region below the fountain. The bubble-laden region extends all the way to the bottom of the tank after about 1500 s, indicating that bubbles are extracted through the exhaust vent and circulated around the system. This observation is crucial in the context of engine oil aeration as all bubbles that are carried downwards past the maximum fountain height will eventually be extracted from the sump and distributed to various components within the engine. The formation of a propagating bubble-rich layer as a by-product of bubble fountains is thus an important process affecting the performance of lubrication systems.

The rise velocity of the bubbles can be inferred from the slope of the colour-contours in figure 3.11 after 1800 seconds. The fastest bubbles (slope of the dark red colour contour) have a rise speed of approximately 1 mm/s, the slowest bubbles rise at a rate of about 0.1 mm/s. Owing to this range in bubble sizes and hence bubble rise speeds, the front of the bubble-rich layer is very diffuse (cf. 3.11 (b)). It is therefore difficult to validate equation 3.9 with the present experiments.

Our observations on the growth of a bubble-rich layer downwards into the tank, however, have motivated a detailed investigation of multiphase filling-box

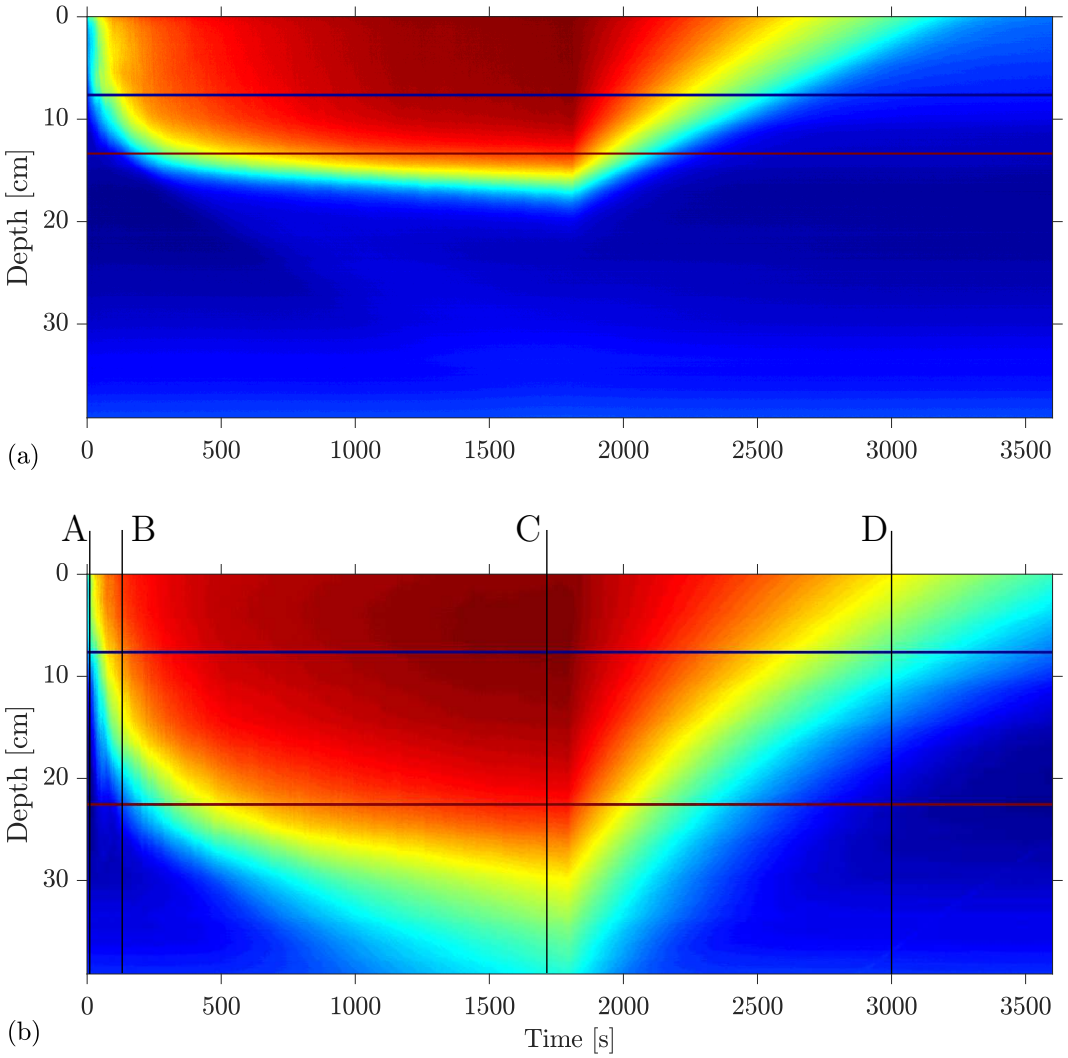

Fig. 3.11 Time-series images of the horizontally-averaged background region (see the two red rectangles in figure 3.10 (a)) for experiments (a) FB1 and (b) FB3. The colour-coding represents a measure of the recorded light intensity. Red indicates a high bubble concentration. Blue indicates clear fluid. The capital letters in panel (b) correspond to the capital letters in figures 3.9 and 3.10.

processes induced by a multiphase fountain in a confined environment. This investigation is presented in the following chapter where we produce particle-laden fountains as an upside-down analogue to bubble fountains. We use a mono-disperse sample of particles to produce particle-laden fountains, as this enables us to precisely control the terminal velocity and the concentration of the second phase. Furthermore, we use water as the working fluid to develop our understanding of these complex processes in a generic liquid. In these experiments it was possible to test and validate equation 3.9.

3.7 Summary

This chapter presented an experimental study on low Reynolds number bubble fountains in oil. Owing to the high viscosity of the working fluid, the flow in the present experiments is in the laminar regime.

Our slow-motion videos revealed a range of bubble sizes from a fraction of a millimetre up to one centimetre. The terminal rise speed of the smallest bubbles was found to be less than 0.1 mm/s and these bubbles do not separate from the fountain flow but are instead carried downwards by the mean flow in the fountain.

We measured the rise height of these laminar fountains and find that the experimental data matches the scalings presented for single-phase fountains with high source Froude numbers and low source Reynolds numbers. This scaling does depend on the source Reynolds number.

The experimental videos demonstrated that a large proportion of the smallest bubbles do not escape the tank on reaching the oil-air interface. Instead, these bubbles accumulate and form a bubble-rich layer that grows downwards into the tank. Time-series images allowed us to visualise the propagation of this bubble front. Measurements of the bubble rise speeds revealed that the velocity of this filling-box front depends on both the strength of the background flow field and the bubble rise speed.

The filling-box flow of bubble fronts driven by bubble fountains is crucial in the context of engine oil aeration but the underlying concepts also apply to the distribution of contaminants and pathogens by ventilation systems. To identify the parameters that control the fate of the bubbles or particles in such systems, we need to reduce the complexity of the system. To overcome the challenges associated with the large range of bubble sizes as well as the laminar nature

of the flow we will proceed in the next chapter with an investigation of the transport of particles by particle-laden fountains in confined environments.

Chapter 4

Particle fountains in a confined environment

4.1 Abstract

We present new experiments and theoretical models of the motion of relatively dense particles carried upwards by a liquid jet into a laterally confined space filled with the same liquid. The incoming jet is negatively buoyant and rises to a finite height, at which the dense mixture of liquid and particles, diluted by the entrainment of ambient liquid, falls back to the floor. The mixture further dilutes during the collapse and then spreads out across the floor and supplies an up-flow outside the fountain equal to the source volume flux plus the total entrained volume flux.

The fate of the particles depends on the particle fall speed, u_{fall}, compared to (i) the characteristic fountain velocity in the fountain core, u_F, (ii) the maximum upward velocity in the ambient fluid outside the fountain, $u_u(0)$, which occurs at the base of the fountain, and (iii) the upward velocity in the ambient fluid above the top of the fountain associated with the original volume flux in the liquid jet, u_{BG}. From this comparison we identify four regimes:

(1) If $u_{fall} > u_F$, then the particles separate from the fountain and settle on the floor.

(2) If $u_F > u_{fall} > u_u(0)$, the particles are carried to the top of the fountain but then settle as the collapsing flow around the fountain spreads out across the floor; we do not observe particle suspension in the background flow.

(3) For $u_u(0) > u_{fall} > u_{BG}$ we observe a particle-laden layer outside the fountain which extends from the floor of the tank to a point below the top of the fountain. The density of this lower particle-laden layer equals the density of the collapsing fountain fluid as it passes downwards through this interface. The collapsing fluid then spreads out horizontally through the depth of this particle-laden layer, instead of continuing downwards around the rising fountain. In the lower layer, the negatively buoyant source fluid in fact rises as a negatively buoyant jet, but this transitions into a fountain above the upper interface of the particle-laden layer. The presence of the particles in the lower layer reduces the density difference between fountain and environment, leading to an increase in the fountain height.

(4) If $u_{fall} < u_{BG}$ then an ascending front of particles rises above the fountain and eventually fills the entire tank up to the level where fluid is removed from the tank.

We compare the results of a series of new laboratory experiments with simple theoretical investigations for each case, and discuss the relevance of our results.

4.2 Introduction

A detailed investigation of the dynamics of particle-laden fountains in a confined environment is an important step towards a better understanding of the transport of particles in industrial process equipment and fluidised beds (Rowe and Nienow, 1976). In many systems, individual jets of fluid are supplied to reactor vessels with the purpose of mixing, suspending, or filtering particles. Particle-laden fountains also develop during explosive volcanic eruptions, when dense mixtures of ash and gas are ejected from volcanic vents at high speed (Woods, 2010). Insights into the transport of dense particles in upward propagating fountains are also related to modelling the transport of bubbles in downward propagating liquid jets, as formed by streams of air and oil entering the sump of internal combustion engines (cf. chapter 2). Depending on the volume flux of the oil, the sump geometry and bubble size and rise speed, the bubbles either rise and escape, or they are carried to the bottom of the sump and recirculate around the engine with adverse effects on lubrication and hydraulics (Nemoto et al., 1997). Producing particle-laden fountains as an analogue experiment to

bubble fountains provides some desirable simplifications as particle size, shape and concentration are easily controlled.

In this chapter, we explore the dynamics of a low-concentration particle-laden fountain supplied to an enclosed vessel. We present a series of new experiments of such flows and compare the results with some simple theoretical models to describe the fate of the particles. We assume there is an outflow at high level above the fountain. The mass concentration of particles at the source is always less than 10% to ensure that the Boussinesq approximation holds for our experiments. We note, however, that especially in fluidised beds, the particle concentration is often higher and such situations are beyond the scope of the present study.

In developing the experiments and models, we are guided by a number of previous studies on the motion of low-concentration particle-laden fountains (Mingotti and Woods, 2015a,b, 2016), and of the ascent and mixing produced by single-phase fountains (SPF) in an enclosed space (Ansong et al., 2008; Baines et al., 1993; Baines and Turner, 1969; Baines et al., 1990; Bloomfield and Kerr, 1999; Linden, 1999).

First, we note that with a particle fountain, there are two regimes which depend on the ratio of the characteristic fountain speed, u_F, compared to the fall speed of the particles, u_{fall}. When u_F exceeds u_{fall}, then the fountain behaves as a single-phase flow (Mingotti and Woods, 2016) and, assuming the Boussinesq approximation applies, then the rise height for high Froude number fountains, $Fr_0 > 4$, depends on the specific buoyancy and momentum flux of the single-phase fountain (subscript SPF) (Turner, 1966),

$$H_{SPF} = 2.46\, m_0^{3/4} |f_0|^{-1/2}, \tag{4.1}$$

where $m_0 = M_0/\pi = b_0^2 u_0^2$ and $f_0 = B_0/\pi = g^{'} b_0^2 u_0$ are the specific buoyancy and momentum fluxes at the source. M and B are the specific buoyancy and momentum fluxes including a prefactor π. Both notations (with and without π) are frequently seen in the literature. In this expression, $g^{'}$ is the reduced gravitational acceleration given by $g^{'} = g\,(\rho_a - \rho_F)/\rho_a$, with ρ_a the density of the ambient liquid and ρ_F the bulk density of the fountain fluid. b_0 and u_0 are the nozzle radius and nozzle exit velocity respectively.

Second, we note that in fountains with large source Froude number, $Fr_0 = u_0/\sqrt{b_0 g^{'}}$, the fountain becomes highly turbulent and entrains a large volume

of fluid as it rises to its maximum height, so that the volume flux at the top of the fountain, Q_{top}, far exceeds that at the source (Bloomfield and Kerr, 2000; Morton et al., 1956; Turner, 1966). The fluid in such fountains decelerates owing to the entrainment of ambient liquid and the presence of the negative buoyancy. During the initial ascent of the dense jet, the fluid reaches a maximum height H_i, but as this fluid collapses back outside the fountain, it is entrained by the ascending flow, increasing the negative buoyancy flux of the ascending flow relative to the ambient. As a result, the fountain height falls to a quasi-steady value $H_F \approx 0.7\, H_i$ (Turner, 1966). A CAD drawing of the experimental set-up is shown in figure 4.1, and a cartoon of a collapsed fountain is shown in figure 4.2 (a), illustrating the up-flow in the fountain, Q_F, the down-flow around the fountain, Q_d, the resulting up-flow in the ambient, Q_u, and the up-flow in the background above the top of the fountain, Q_0. In an unconfined environment, the top of the fountain oscillates around the height H_F. In a laterally confined environment, however, an upward flow develops in the ambient fluid, fed by the liquid spreading out from the fountain on the floor. Baines et al. (1990) have investigated this fountain filling-box phenomenon for classical single-phase fountains in a homogeneous environment and Bloomfield and Kerr (1999) extended the work to account for a density-stratified environment. They found that when the volume flux supplied through the fountain was removed at high level above the fountain, the ambient layer of more dense fluid always grows past the height of the fountain. The increasing density of the ambient fluid leads to a gradual decrease in the negative buoyancy flux of the fountain and hence an increase in fountain height.

In this chapter we explore the filling-box dynamics of particle-laden fountains which result when a jet of particle-laden fluid enters an enclosed space filled with the same fluid. We first introduce the experimental method in section 4.3 and then present our experimental data and theoretical models, arranged into four regimes, which depend on the terminal fall speed of the particles relative to the three characteristic velocities in the system.

4.3 Experimental method

We generated particle-laden fountains by supplying a mixture of fresh water and Silicon-Carbide particles to an upwards directed nozzle submerged in a tank of fresh water. The particles provide a buoyancy force which opposes the

direction of the momentum flux at the source, thus producing a fountain. In this chapter we present two groups of experiments: Firstly, a set of 9 experiments for which all source conditions are fixed and only the particle size is varied between 12.8 μm and 212 μm. The exact particle sizes and source conditions are listed in table 4.1 above the horizontal line (experiments a-i). Secondly, we present a set of 25 experiments with particle diameters between 12.8 and 30 μm. In this second set we also vary the nozzle diameter, source fluxes and particle concentration. These fountains have source Reynolds numbers between 1000 and 4000 and the initial Froude numbers range from 6 to 42. Three round stainless steel nozzles of internal diameter of approximately 2.9 mm, 5.2 mm and 8.5 mm were used as the sources. By repeating all experiments once, we estimate that the error associated with our experiments is somewhere close to 15%.

The mixture of water and particles (*Carborex F070 to F500* by *Washington Mills*) was pumped (*Watson Marlow* peristaltic pump) through a submerged nozzle at the bottom of a Perspex tank of dimensions 40 cm x 20 cm x 20 cm as shown in figure 4.2 (b). An electroluminescent light sheet, connected to the back of the tank, provided uniform illumination for a *JAI SP-5000* monochrome high-speed camera with a 1:28 *HAMA* lens. High-speed videos, eight minutes in length, with a frame rate of 10 Hz were recorded for all experiments. We use time-series images through the fountain centreline to extract the fountain height automatically.

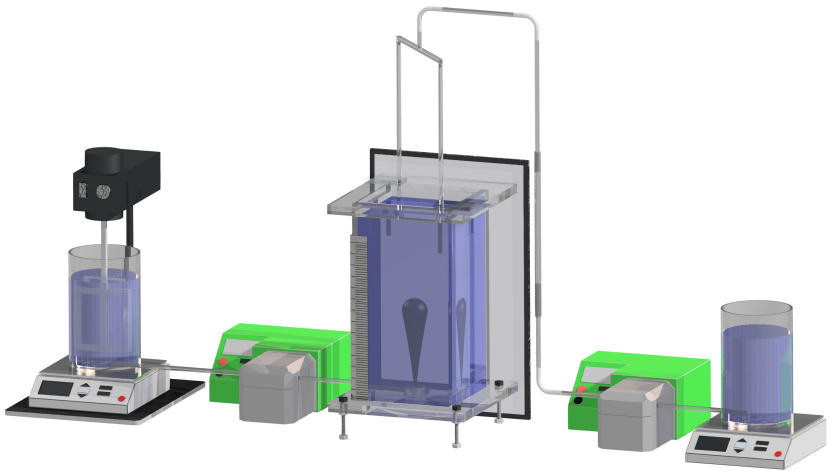

Fig. 4.1 CAD drawing of the experimental set-up showing the tank in the middle, with a peristaltic pump (green) on either side. The mixer, shown to the left, ensures that the particles remain suspended in the source fluid tank.

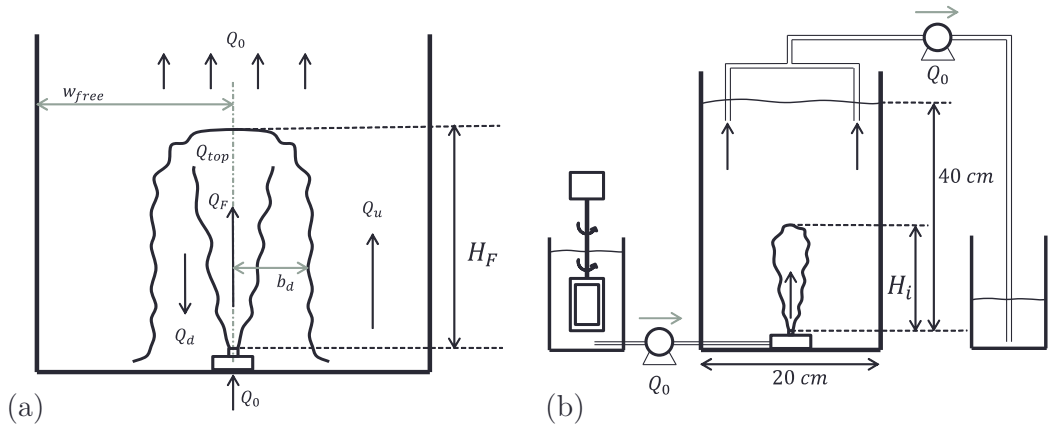

Fig. 4.2 (a) Cartoon of the collapsed fountain showing the fountain height, H_F, and the volume fluxes in the fountain core, Q_F, the down-flow, Q_d, the up-flow outside the fountain, Q_u, and the volume flux above the top of the fountain, Q_0. (b) 2D schematic of the experimental set-up: Particles and fresh water are mixed together and pumped through a nozzle at the bottom of the tank (centre). A second pump extracts the liquid at the top of the tank to maintain a fixed reservoir level. The initial fluid leaving the nozzle reaches a maximum height, H_i (panel (b)), prior to the development of the collapsing fluid around the central jet, which leads to the lower quasi-steady fountain height, H_F (panel (a)). Once the filling-box flow develops in the ambient fluid, some particles may be suspended, leading to an adjustment to a steady-state fountain height H_∞ (section 4.7).

Exp.	d_P $[\mu m]$	u_{fall} $[mm/s]$	b_0 $[mm]$	$C_0(SiC)$ $[g/L_W]$	Q_0 $[ml/s]$	u_0 $[m/s]$	Fr_0 $[-]$	H_F $[cm]$	$\kappa = Q_0/(A\, u_{fall})$ $[-]$
a	212	54.1	2.60	30	11.6	0.54	24	5.96	0.005
b	106	13.5	2.60	30	11.6	0.54	24	8.64	0.021
c	75.0	6.78	2.60	30	11.6	0.54	24	10.6	0.043
d	63.0	4.78	2.60	30	11.6	0.54	24	15.9	0.060
e	44.5	2.39	2.60	30	11.6	0.54	24	13.5	0.121
f	36.5	1.60	2.60	30	11.6	0.54	24	14.7	0.180
g	29.2	1.03	2.60	30	11.6	0.54	24	13.8	0.281
h	17.3	0.56	2.60	30	11.6	0.54	24	14.1	0.801
i	12.8	0.31	2.60	30	11.6	0.54	24	13.5	1.463
1	29.2	1.03	1.45	50	6.06	0.92	42	12.7	0.148
2	29.2	1.03	2.60	50	6.06	0.29	10	4.91	0.148
3	29.2	1.03	2.60	10	6.06	0.29	22	9.27	0.148
4	29.2	1.03	2.60	10	11.6	0.54	41	18.9	0.281
5	29.2	1.03	2.60	50	11.6	0.54	18	8.95	0.281
6	29.2	1.03	4.25	10	6.06	0.11	6	6.11	0.148
7	29.2	1.03	4.25	10	11.6	0.20	12	13.7	0.281
8	17.3	0.36	1.45	50	6.06	0.92	42	13.0	0.420
9	17.3	0.36	2.60	50	6.06	0.29	10	4.74	0.420
10	17.3	0.36	2.60	10	6.06	0.29	22	10.6	0.420
11	17.3	0.36	4.25	50	23.8	0.42	11	10.1	1.651
12	17.3	0.36	4.25	10	6.06	0.11	6	5.13	0.420
13	17.3	0.36	4.25	10	23.8	0.42	25	28.9	1.651
14	12.8	0.20	2.60	10	11.6	0.54	41	19.4	1.436
15	12.8	0.20	2.60	50	11.6	0.54	18	9.61	1.436
16	12.8	0.20	4.25	10	11.6	0.20	12	14.1	1.463
17	12.8	0.20	4.25	10	23.8	0.42	25	26.2	3.015
18	12.8	0.20	4.25	10	22.2	0.39	23	23.1	2.815
19	12.8	0.20	4.25	50	22.2	0.39	10	9.14	2.815
20	29.2	1.03	1.45	50	3.60	0.55	25	8.01	0.088
21	29.2	1.03	4.25	50	23.8	0.42	11	12.2	0.579
22	12.8	0.20	4.25	10	17.1	0.30	18	25.2	2.166
23	12.8	0.20	4.25	10	19.7	0.30	21	21.1	2.491
24	12.8	0.20	4.25	50	17.1	0.35	8	8.69	2.166
25	12.8	0.20	4.25	50	19.7	0.35	9	10.5	2.491

Table 4.1 Table with source conditions for two sets of experiments on turbulent particle-laden fountains. In the experiments above the horizontal line, all parameters except the particle size and thus u_{fall} are kept constant. In the remaining experiments we vary the source momentum and buoyancy fluxes. The table lists: number of the experiment ($Exp.$), particle diameter (d_P), Stokes' velocity of the particles (u_{fall}), nozzle radius (b_0), initial particle concentration (C_0), volume flux at the source (Q_0), nozzle exit velocity (u_0), source Froude number (Fr_0), fountain height (H_F), and ratio of background velocity to terminal particle settling velocity (κ).

4.4 Experimental observations: identification of 4 regimes

In our first set of experiments (table 4.1, a-i) all source conditions are fixed and we only vary the particle size and thus the terminal fall speed of the particles, u_{fall}, as given by Stokes' law for the small particles used herein,

$$u_{fall} = \frac{2}{9} g \frac{\rho_P - \rho_W}{\mu_W} \frac{d_P^2}{4}, \tag{4.2}$$

where $\rho_P = 3.21\,\mathrm{g/cm^3}$ is the density of the Silicon Carbide particles, $\rho_W \approx 1\,\mathrm{g/cm^3}$ is the density of the ambient water and $\mu_W \approx 1\,\mathrm{mPa\,s}$ is the dynamic viscosity of water at room temperature. The Reynolds number of the particles based on their fall speed and radius is always much smaller than 10 (much smaller than 0.1 for experiments 1-25).

We find that the fate of the particles depends on the relative magnitude of u_{fall} compared to three distinct up-flow velocities. These are (i) the up-flow velocity within the fountain core as quantified by the characteristic fountain velocity, $u_F = B_0^{1/2} M_0^{-1/4}$, (ii) the maximum upward filling-box speed in the ambient fluid which occurs at the base of the fountain, $u_u(0)$, and (iii) the up-flow velocity above the top of the fountain, u_{BG}, which results from the source flux, $u_{BG} = Q_0/A$, where $Q_0 = \pi q_0 = \pi b_0^2 u_0$ is the source volume flux and A is the cross-sectional area of the tank. Based on the ratios $u_F/u_{fall}, u_u(0)/u_{fall}$ and u_{BG}/u_{fall}, we identify four regimes which are illustrated in figure 4.3 and described in the following sections.

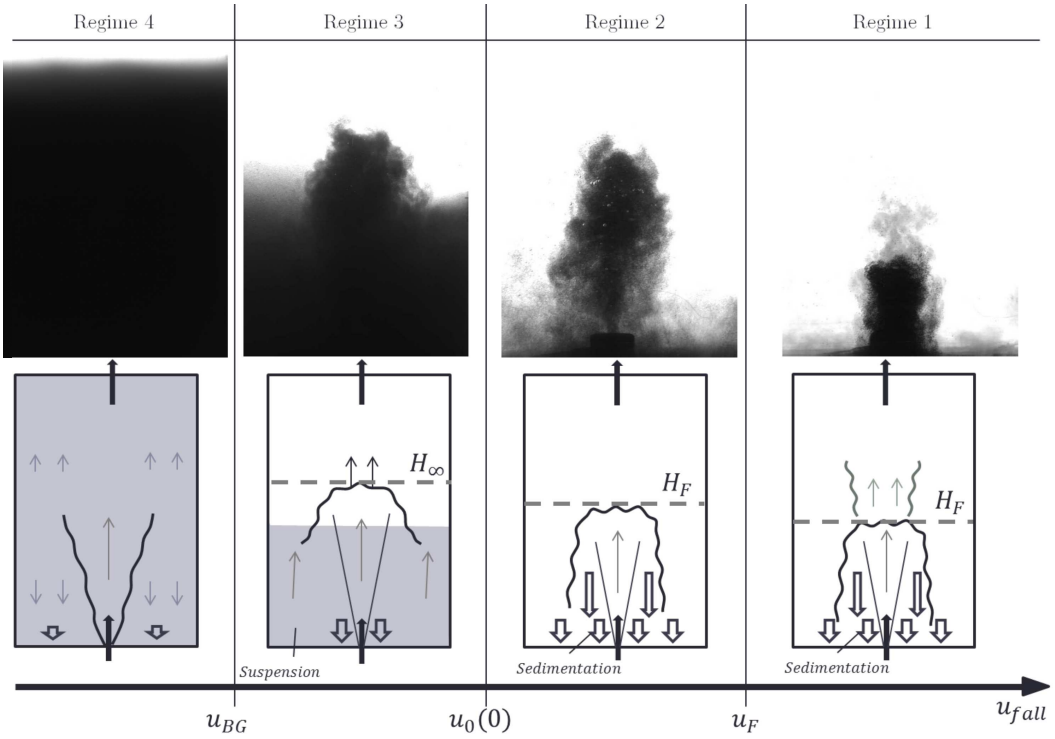

Fig. 4.3 Regime diagram with images from four experiments (Regime 1: exp (a); Regime 2: exp (c), Regime 3: exp (g); Regime 4: exp (i)) and accompanying schematics describing the quasi-steady-state observations for the four distinct regimes. The regimes depend on the relative magnitude of u_{fall} compared to the characteristic fountain velocity, u_F, the maximum up-flow speed outside the fountain, $u_u(0)$, and the background velocity, u_{BG}. In the experimental image of the separated flow regime (Regime 1), some dye has been added to the source liquid to show that the particles separate from the flow when the fountain liquid still has some upward momentum.

4.5 Regime 1: $u_{fall} > u_F$, the separated two-phase fountain

If u_{fall} exceeds the characteristic fountain velocity, u_F, the particles separate from the fountain liquid and fall out of the fountain before the liquid runs out of momentum. Mingotti and Woods (2016) found that the maximum height reached by the particles in a particle-laden fountain, H_F, decreases compared to the height of an equivalent single-phase fountain, H_{SPF}, if $\Lambda = u_{fall}/u_F > 0.25$. Figure 4.4 (a) illustrates the variation of H_F/H_{SPF} as a function of Λ for experiments a-i, and our observations are consistent with the results of Mingotti and Woods (2016).

4.6 Regime 2: $u_F > u_{fall} > u_u(0)$, no filling-box

For $\Lambda = u_{fall}/u_F < 0.25$, particle-laden fountains behave like the analogous single-phase fountain of the same buoyancy and momentum flux, and the particles are carried to the top of the fountain. However, if u_{fall} is larger than the maximum filling-box speed in the ambient, $u_{fall} > u_u(0)$, the particles quickly settle to the floor. No particles are suspended in the environment and the fountain reaches a quasi-steady height, H_F. The maximum filling-box speed, $u_u(0)$, can be estimated by considering the total volume flux in the fluid, which collapses back down to the base of the tank around the central up-flowing fountain. Burridge and Hunt (2016) have measured the total volume flux of the collapsing fluid at the level of the source, $Q_d(0)$, and based on their data for $Fr_0 > 2$ they proposed the empirical law

$$Q_d(0) = Q_0(1 + 0.71Fr_0). \tag{4.3}$$

The upward filling-box flow, Q_u, and the upward filling-box velocity, u_u, are then given by the mass balance

$$Q_u(z) = A_{free}u_u(z) = Q_d(z) - Q_F(z) + Q_0 \tag{4.4}$$

where $A_{free} = A - A_F$ is the available area for the up-flow. A is the area of the enclosed space and A_F the area of the fountain. Mizushina et al. (1982) have shown experimentally that the radius of a collapsing fountain is constant

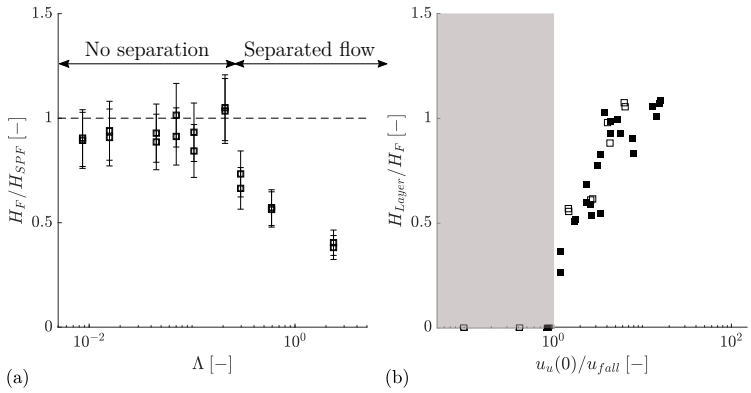

Fig. 4.4 (a) Ratio of the quasi-steady fountain height, H_F, as a fraction of the height of an equivalent single-phase fountain, H_{SPF} (equation 4.1), for experiments a-i as listed in table 4.1. This ratio is shown as a function of $\Lambda = u_{fall}/u_F$. The height of the particle-laden fountain is comparable to a single-phase fountain if $u_{fall} < 0.25u_F$, but decreases as Λ increases to larger values and the effects of separated flow become increasingly important (Mingotti and Woods, 2016). (b) Variation of the ratio of particle layer height in the ambient to the quasi-steady fountain height, H_{Layer}/H_F, as a function of $u_u(0)/u_{fall}$ for all experiments for which $u_{fall} > u_{BG}$. For $u_u(0)/u_{fall} < 1$ (region shaded in grey), no layer is observed. Experiments a-i are plotted as empty squares, the remaining experiments as solid squares.

at approximately $b_d = 0.37H_F$, so that $A_F = \pi b_d^2$. In figure 4.4 (b) the region where $u_{fall} > u_u(0)$ is shaded in grey. This panel contains a plot of the ratio of measured particle layer height as a fraction of the fountain height, H_{Layer}/H_F, as a function of the velocity ratio $u_u(0)/u_{fall}$. The graph illustrates that for $u_{fall} > u_u(0)$ no layer is observed. For $u_{fall} < u_u(0)$, however, a particle layer does form and becomes progressively deeper as $u_u(0)/u_{fall}$ increases. This is discussed in the following sections.

4.7 Regime 3: $u_u(0) > u_{fall} > u_{BG}$, trapped filling-box

If the particle fall speed is smaller than the maximum up-flow velocity outside the fountain, but exceeds the background velocity above the top of the fountain, $u_{BG} < u_{fall} < u_u(0)$, a particle layer develops around the fountain and extends from the floor to some height smaller than the fountain height. The presence of the particle-rich layer in this regime reduces the effective negative buoyancy flux in the fountain. Consequently, the fountain height increases from the quasi-

steady height prior to the development of the particle-laden layer, H_F, to a new steady-state fountain height, H_∞. Figure 4.5 (a) contains an experimental time-series image describing the evolution of a single vertical line of pixels, through the centre of a fountain, as a function of time. The initial starting fountain flow reaches a height of about 29 cm, but after approximately 10 s the fountain collapses and adjusts to a quasi-steady height of approximately H_F = 20 cm. The filling-box process then becomes established over the next 200 s (panel (c)), and the fountain height gradually rises to $H_\infty \approx 24$ cm. Both the initial quasi-steady fountain height, H_F, and the increased fountain height, H_∞, are marked in panel (a). Both H_F and H_∞ were determined automatically by detecting the top of the fountain from the time-series image through the fountain centre (panel (a)) after the initial fountain collapse. The random oscillations of the fountain top were averaged by considering a fountain height averaged over a 10 second period as shown by the red line in figure 4.5 (b). The initial averaged height corresponds to H_F, and the final averaged height is taken to be H_∞. The averaging period over which the running mean fountain height was computed (red line (b)) was chosen to be large compared to the time-scale over which the fountain top oscillates, but small compared to the time-scale over which the filing-box flow in the background becomes established. In our experiments, the time scale of fountain height fluctuation is of the order of seconds, and the time scale over which a particle layer develops in the ambient is closer to 100 seconds. We chose an averaging period of 10 seconds, but we find that averaging periods in the range from 5–20 s yield similar values for H_F and H_∞.

In order to calculate the height of rise of the fountain, we require a model that considers the ascent of a fountain which initially rises through the particle-laden layer of ambient fluid, but which then adjusts owing to the rapid increase in the negative buoyancy flux as it rises into the particle free layer above. In our investigation of this process we are guided by previous studies on single-phase salt water fountains in a two-layer stratified environment (Ansong et al., 2008; Baines et al., 1993). To help guide our understanding, in figure 4.6 (a) we show the key results presented by Baines et al. (1993). They produced single-phase fountains in a closed, ventilated space in which a constant flux of ambient fluid was removed from the tank at the level of the source. This led to the development of a counter-flow in the tank, opposing the direction of the initial momentum of the fountain. A stable interface develops at the height where

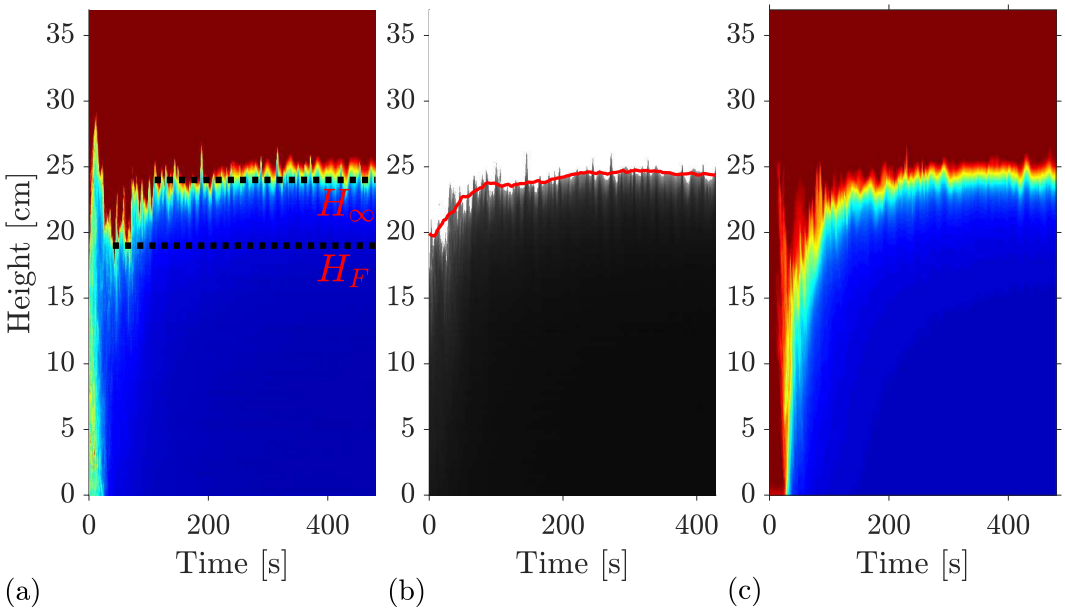

Fig. 4.5 (a) Time-series image in false-colour of a vertical line through the centre of the fountain obtained for exp. 4 in table 4.1. The overshoot fountain height, $H_i \approx 29\,\text{cm}$, after 10 s is followed by the quasi-steady fountain height, H_F, after about 30 s. As the filling-box flow develops (panel (c)) the fountain height increases to the steady-state fountain height, H_∞. (b) Illustration of the automated extraction of H_F and H_∞ by computing the average fountain height over a period of 10 seconds, as shown by the red line. (c) Time-series image of horizontally averaged light intensity outside the fountain illustrating the development of the particle layer in the background around the fountain.

the total entrainment into the fountain above the interface matches the volume flux of fluid removed from the tank (minus the source flux Q_0) at the elevation of the source. At large times, the buoyancy flux entering the tank through the nozzle is balanced by the total buoyancy flux of the liquid flux removed from the tank,

$$g_0^{'}Q_0 = g_{lower}^{'}(Q_{vent} + Q_0) \tag{4.5}$$

where $g_{lower}^{'}$ is the buoyancy in the lower layer and Q_{vent} is the volume flux of the ventilation flow. The authors further establish that at the height of the interface between the two layers, the buoyancy of the downward collapsing flow which is shed from the top of the fountain, $g_{d,int}^{'}$, matches $g_{lower}^{'}$. Hence, below the interface, they do not observe a strong return flow around the fountain core. We have repeated their experiments and show the results in figure 4.7. Panel (a) shows an image of the single-phase salt water fountain after the initial collapse. Panel (b) shows the fully developed two-layer stratification owing to the background flux in the tank. The colour of the source liquid is changed in panel (c) and (d) to monitor the flow path of the fountain fluid. We observe that upon entering the lower layer, the downward collapsing flow spreads out horizontally throughout the depth of the lower layer.

In the present experiments, by analogy, we envisage that the fountain fluid falling into the particle layer has the same buoyancy as this layer and so it spreads out horizontally into this layer, in a similar fashion to the saline fountain (figure 4.7). Owing to the absence of a return flow in the lower layer, we model the flow produced by the jet issuing from the source as a particle-laden jet with negative buoyancy. However, once this jet penetrates the interface with the particle free layer, we assume that the flow transitions to a turbulent fountain. The source conditions of this fountain correspond to the previously calculated jet properties just above the interface. The equations for the conservation of volume, buoyancy and momentum fluxes of a negatively buoyant jet in a uniform environment and their respective changes in the direction of the vertical co-ordinate z are

$$Q(z) = \pi b(z)^2 u(z) \qquad \frac{dQ(z)}{dz} = \alpha 2\pi b(z)u(z) \tag{4.6}$$

$$B(z) = \pi b(z)^2 u(z) g^{'}(z) \qquad \frac{dB(z)}{dz} = 0 \tag{4.7}$$

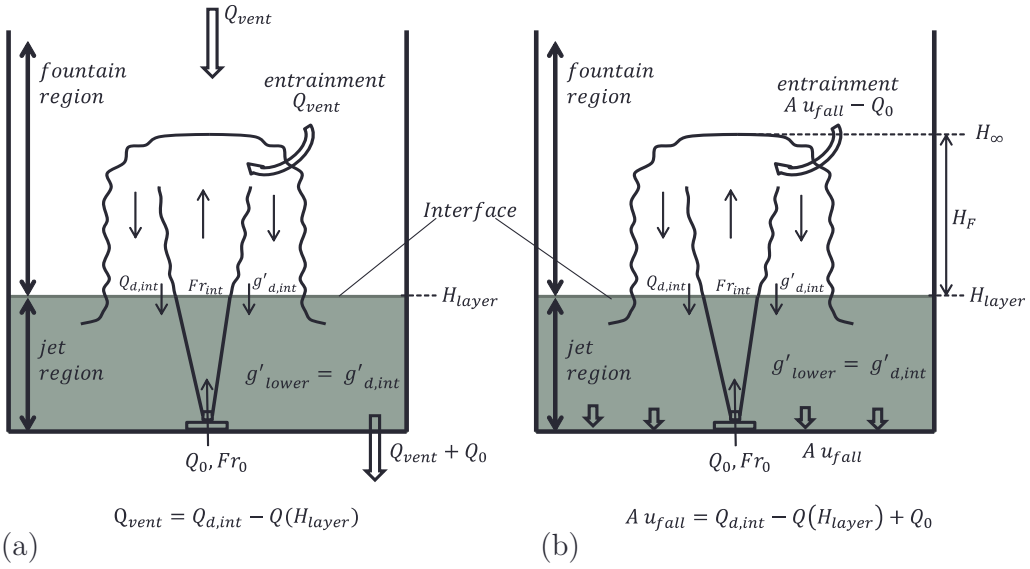

Fig. 4.6 (a) Cartoon illustrating the experimental set-up and key results of Baines et al. (1993) on single-phase fountains in a confined ventilated space. The height of the interface at $z = H_{layer}$ is fixed. In the lower layer, the flow issuing through the nozzle resembles a negatively buoyant jet. Above the interface, the flow transitions into a turbulent fountain. The entire ventilation flux, Q_{vent}, is entrained into the fountain above the interface. The buoyancy of the collapsing down-flow matches the buoyancy in the lower layer. (b) In Regime 3, a particle-laden layer forms which extends from the bottom of the tank to a height $z = H_{layer}$. Motivated by Baines et al. (1993) we model the flow in the lower layer as a negatively buoyant jet which transitions into a fountain as it passes upwards through the interface. The buoyancy of the downward return flux equals the buoyancy in the lower layer. Some fraction of the collapsing particle flux is re-entrained into the fountain, the remainder settles on the floor.

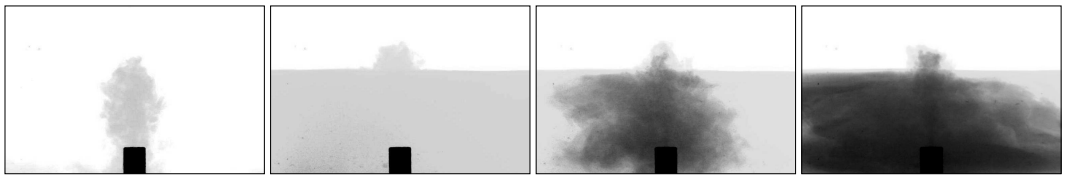

(a) (b) (c) (d)

Fig. 4.7 Images of single-phase fountains in a ventilated enclosure. (a) A single-phase salt water fountain ($H_F \approx 8$ cm) is produced in a fresh water tank. (b) The background ventilation rate, Q_{vent}, is adjusted (cf. Baines et al. (1993)) such that a stable two-layer stratification develops in the ambient. (c) In steady-state, the colour of the source liquid is changed to visualise the flow path of the fountain fluid. (c-d) The source liquid rises to the top of the fountain, collapses and spreads out at all heights around the fountain. A strong return flow, as characteristic for a fountain, is not observed in the lower layer.

$$M(z) = \pi b(z)^2 u(z)^2 \qquad \frac{dM(z)}{dz} = -\pi b(z)^2 g^{'}(z) \tag{4.8}$$

as described by Morton et al. (1956), where we adopt the horizontally-averaged top-hat model for the jet properties as well as the entrainment hypothesis which states that the entrainment of ambient liquid into the jet is proportional to the local jet velocity at any height. The constant of proportionality is taken to be $\alpha \approx 0.076$ (Bloomfield and Kerr, 2000).

For the present experiments on particle-laden fountains the analogue to the volume flux removed from the tank at the height of the source, $Q_{vent} + Q_0$, is the settling of particles at the bottom of the tank. The buoyancy of the lower layer may thus be determined as

$$g^{'}_{lower} = \frac{g^{'}_0 Q_0}{A u_{fall}}, \tag{4.9}$$

as illustrated by the cartoons in figure 4.6 (a) and (b). The effective buoyancy of the negatively buoyant jet in the lower layer becomes $g^{'}_{0,eff} = g^{'}_0 - g^{'}_{lower}$. The height of the top of the fountain, which forms as the negatively buoyant jet rises through the interface into the particle free fluid, is given as the sum of the interface height, H_{layer}, and the height of a turbulent fountain in the upper layer, $H_{F,upper}$, with the source conditions matching the properties of the jet just above the interface,

$$H_{\infty,theo} = H_{layer} + H_{F,upper}. \tag{4.10}$$

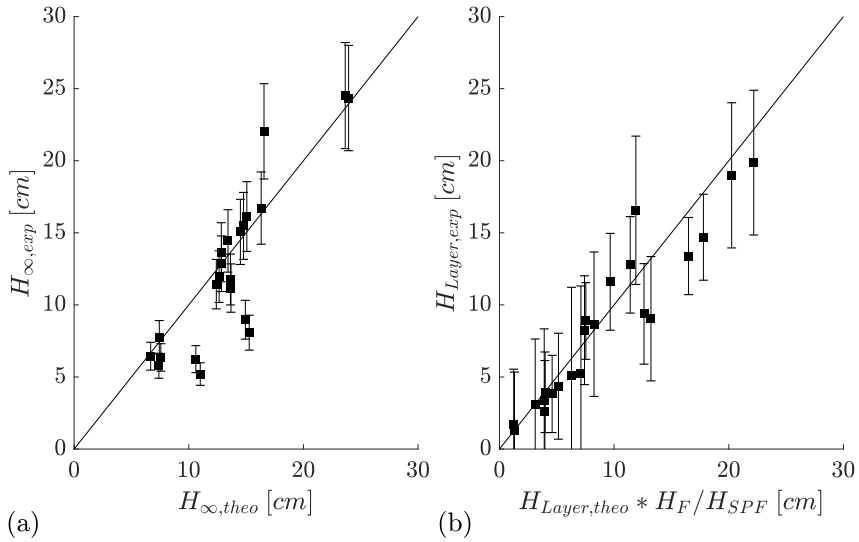

Fig. 4.8 (a) Comparison of the experimental measurements of total fountain height in the two-layer stratification, $H_{\infty,exp}$, on the y-axis, and the theoretical estimate of this height, $H_{\infty,theo}$ on the x-axis. (b) Plot of the measured height of the interface, $H_{Layer,exp}$, on the y-axis as a function of the theoretical estimate of the layer height, $H_{Layer,theo}$, corrected by the ratio H_F/H_{SPF}, on the x-axis.

Hunt and Burridge 2015 have published a detailed set of experiments with empirical relationships between the quasi-steady rise height of turbulent fountains as a function of the source radius of the jet and the Froude number for very weak fountains ($0.3 < Fr_0 < 1$), weak fountains ($1 < Fr_0 < 2$), intermediate fountains ($2 < Fr_0 < 4$) and forced fountains ($Fr_0 > 4$, see equation 4.1). We adopt these relationships to compute a theoretical estimate of the total fountain height in the upper layer, based on the jet radius just above the interface, b_{int}, and the corresponding Froude number, defined in terms of the density difference of the fountain and the upper layer fluid, g'_{int}, the jet velocity just above the interface, u_{int}, and the jet radius so that $Fr_{int} = u_{int}/\sqrt{g'_{int} b_{int}}$. In turn, the values of b_{int}, u_{int} and g'_{int} at the interface are calculated by numerical solution of the jet equations (equation 4.6 - 4.8) with the actual source conditions at the inflow nozzle, using the result in equation 4.5 to determine the effective buoyancy of the incoming jet. The results are shown in figure 4.8 (a), where we plot the experimentally determined total fountain height, $H_{\infty,exp}$, on the y-axis as a function of the corresponding theoretical estimate for the fountain height, $H_{\infty,theo}$ on the x-axis. Most data points (black squares) are in reasonable agreement with the solid black line, which has a gradient of one.

A theoretical estimate of the height of the interface between the lower and the upper layer in steady-state, H_{layer}, was obtained by matching the mass flux of the particles in the collapsing down-flow of the fountain above the interface with the settling flux of particles at the floor of the tank. Since the concentration of particles in the collapsing downflow matches that in the lower layer, this balance reduces to the simple form

$$Q_{d,int} - Q(H_{layer}) + Q_0 = A\, u_{fall}. \tag{4.11}$$

The cartoons in figure 4.6 (a) and (b) illustrate that $Q_{d,int}$ is the total volume flux of the collapsed fountain at the height of the interface. Burridge and Hunt (2016) provide a detailed set of empirical laws relating the total volume flux of a turbulent single-phase fountain as it collapses and falls past the original height of the input nozzle to the source Froude number. We use this relation to compute the total flux of collapsing fountain fluid, $Q_{d,int}$, by first solving the jet equations for each interface height. We then employ the empirical relationships to determine the value of $Q_{d,int}$ for each iteration of H_{layer}. We take the interface height at which $Q_{d,int} - Q(H_{layer}) + Q_0$ first decreases below $A\, u_{fall}$ as our theoretical estimate of the layer height, $H_{layer,theo}$. In figure 4.8 (b) the measured fountain height, $H_{Layer,exp}$, is plotted as a function of the theoretically estimated layer height, corrected by the ratio of measured fountain height and single-phase fountain height. The experimental data are compared with the theoretical prediction (black solid line of gradient one).

4.8 Regime 4: $u_{fall} < u_{BG}$, unbounded filling-box

When the terminal particle fall speed falls below the background velocity, $u_{fall} < u_{BG}$, particles are lifted above the top of the fountain and a particle front gradually fills the entire tank. The relative magnitude of the particle fall speed to the background velocity may be expressed in terms of the dimensionless parameter κ,

$$\kappa = \frac{Q_0}{A\, u_{fall}}. \tag{4.12}$$

Figure 4.9 (a) contains a plot of the ratio of measured particle layer height to quasi-steady fountain height, H_{Layer}/H_F, as a function of κ. The region $\kappa > 1$

is shaded in grey. In this regime the front rises and gradually fills the entire tank. Some experiments with κ close to, but smaller than one also led to the development of a particle-rich layer above the top of the fountain as shown in figure 4.9 (a). This is the result of the finite size distribution of the particles used in the experiments, such that even if the mean particle fall speed exceeds the background speed, u_{BG}, there is a non-negligible fraction of the particles for which $u_{fall} < u_{BG}$ and hence which are carried upwards to the high level vent in the tank.

An example of the ascending front of the particle layer is displayed in the experimental time-series image shown in figure 4.9 (b). By extracting the slope of the propagating fronts in such time-series images, we may estimate the filling-box speed. Figure 4.10 (a) illustrates the ratio of measured front velocity and the background velocity, u_{rise}/u_{BG}, as a function of κ. The solid black line corresponds to the background velocity minus u_{fall},

$$u_{rise} = u_{BG} - u_{fall}. \tag{4.13}$$

We observe that the measured rise speeds are described reasonably well by equation 4.13. The scatter is associated with the range of particle sizes, resulting in a diffuse front.

To check for consistency, we ran a series of equivalent single-phase fountain experiments for the source conditions of experiments 1-25 and found that the measured front velocities corresponded to the background velocity, u_{BG}, within an error of less than 8%. In figure 4.10 (a), these data points would lie on the dashed horizontal line.

In this regime, the influx of particles, Q_P, is balanced by both the flux of particles settling at the bottom of the tank (first term on the right-hand side below) and the flux of particles vented through the outflow at the top of the tank (second term on the right-hand side below),

$$Q_P = C_0 Q_0 = C_E A\, u_{fall} + C_E(Q_0 - A u_{fall}), \tag{4.14}$$

where we assume the particle concentration in the ambient fluid, C_E, is uniform. From equation 4.14, we infer that the particle concentration in the ambient matches the particle concentration at the source,

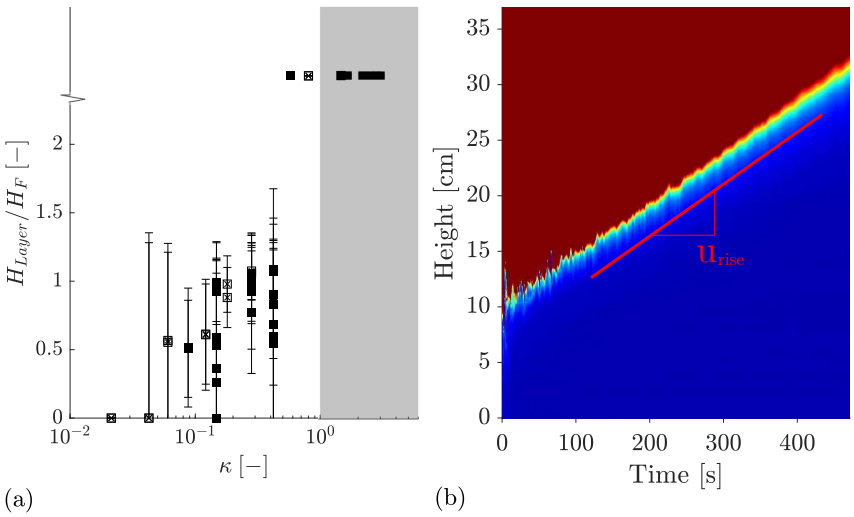

Fig. 4.9 (a) Variation of the ratio of the depth of the particle layer as a fraction of the quasi-steady fountain height, H_F, as measured for all experiments shown in table 4.1. The ratio is shown as a function of κ, the ratio of the background flow speed above the top of the fountain and the terminal particle fall speed. Open symbols correspond to experiments a-i and solid symbols represent experiments 1-25. For $\kappa > 1$ the interface height rises indefinitely. (b) Time-series image in false-colour through the centre of the fountain obtained for exp. 13 in table 4.1. The particle-laden layer (blue) surpasses the quasi-steady fountain height, H_F, after approx. 30 s, after which the front gradually fills the entire tank.

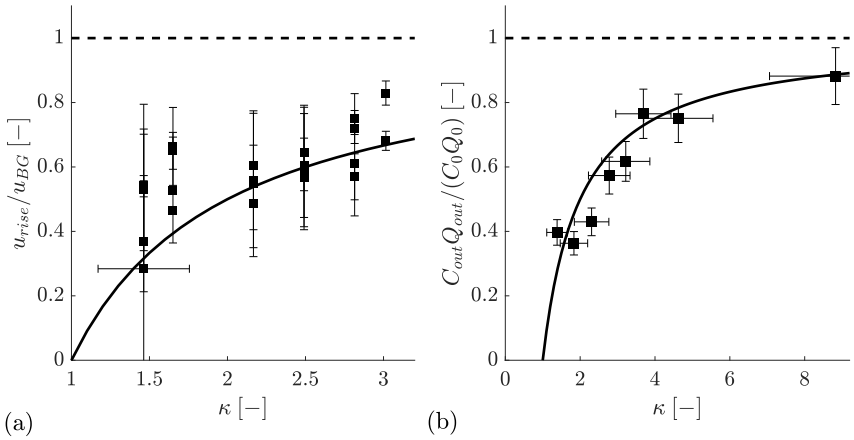

Fig. 4.10 (a) Plot of the ratio of the measured particle-laden front velocity to the background velocity, u_{rise}/u_{BG}, as a function of κ. The solid line corresponds to the prediction $u_{rise} = u_{BG} - u_{fall}$. (b) Measurement of the ratio of the vented particle flux, $C_{out}Q_{out}$, and the total volume flux supplied to the tank, C_0Q_0, plotted as a function of κ for $\kappa > 1$. The solid black line corresponds to the theory.

$$C_E = C_0. \tag{4.15}$$

As a result of this equality, the flow issuing from the nozzle now resembles a neutrally buoyant jet. Unfortunately, in this regime the particles in the background flow block the view of the fountain so we have not been able to visualise the flow issuing from the source. However, we have tested the prediction of equation 4.15 by running eight experiments in which we collect the outflow from the top of the tank. The weight of the total mixture of water and particles was measured as well as the weight of only the particles after a drying process, in order to determine the flux of particles issuing from the tank, $C_{out}Q_{out}$. The ratio of the vented particle flux to the total particle flux may thus be written as

$$\frac{C_0\left(Q_0 - Au_{fall}\right)}{C_0\left(Q_0 - Au_{fall}\right) + C_0 Au_{fall}} = 1 - \frac{1}{\kappa}. \tag{4.16}$$

The prediction of this model is shown as a solid black line in figure 4.10 (b) and appears to be in reasonable agreement with our experimental measurements.

4.9 Summary

We have studied the transport of particles supplied to a confined environment as a particle-laden fountain. We have identified four distinct regimes by comparing the terminal particle fall speed, u_{fall}, against the up-flow velocities in the fountain core, outside the fountain, and in the background above the top of the fountain. In Regime 1, the particles separate from the fountain liquid. In Regime 2, all particles are carried to the top of the fountain, but very quickly settle from the collapsing down-flow and do not form a particle layer in the ambient. In Regime 3, we observe a trapped particle-rich layer in the ambient fluid. This reduces the density difference between fountain and environment and encourages larger fountain heights. In Regime 4, the background flow is strong enough to lift particles above the top of the fountain and the entire tank eventually fills with particles. Novel experimental data are complemented by simple models which predict (i) whether or not a particle-rich layer develops in the ambient, (ii) the height of the contaminated layer, (iii) the increase in fountain height owing to the presence of the particle-rich layer, (iv) the velocity of the rising particle layer front for $\kappa > 1$, and v) the concentration of particles

in the ambient for $\kappa > 1$. This work provides a framework for interpreting the fate of particles carried by liquid jets in a confined space.

It would be of great interest to develop the models and experiments introduced herein to suspensions of multiple sizes, both in terms of the dynamics and also the potential for a novel separation system.

In the next chapter, we proceed with an experimental study on extremely confined single-phase fountains to investigate at what point the presence of the confinement affects the rise height and entrainment of these fountains.

Chapter 5

Experiments on horizontally confined turbulent fountains

5.1 Abstract

We present an experimental study on the effects of horizontal confinement on the rise height and entrainment of turbulent single-phase fountains. The axisymmetric single-phase fountains have source Reynolds numbers ranging between 1400 and 3000 and are generated by issuing dense fluid upwards through a round nozzle with a diameter of 3.8 mm. The fountains are placed inside a transparent confining tank of width W_C, open at top and bottom. We measure the rise height of the fountains as well as the entrainment of ambient liquid, and we investigate the dependence of these quantities on the ratio of the width of the confinement and the diameter of an equivalent unconfined fountain, W_C/D_{SPF}. We find that both the rise height and the entrainment efficiency of the present fountains remain unaffected by the confinement for $W_C/D_{SPF} > 2$. For smaller values of W_C/D_{SPF}, however, we observe a monotonic decrease in the rise height and the total entrainment and we present scaling arguments describing the entrainment into such extremely confined fountains.

5.2 Introduction

Turbulent fountains are frequently observed in industry and nature. A thorough understanding of the fluid flow in turbulent fountains is essential to predict the impact of volcanic eruptions, and to optimise industrial equipment such as air

conditioning and ventilation systems or water treatment plants (Bloomfield and Kerr, 2000; Kaminski et al., 2005; Lin and Linden, 2005; Mingotti and Woods, 2016; Neto et al., 2016; Van de Donk, 1981).

A wide range of literature exists on turbulent fountains based on the pioneering work of Turner (1966). Many authors have focussed their attention on developing scaling laws for the initial and steady-state rise heights reached by unconfined turbulent fountains, as well as the total entrainment of ambient fluid into the fountain flow (Burridge and Hunt, 2012, 2016; Hunt and Burridge, 2015; Kaminski et al., 2005; Mingotti and Woods, 2016; Turner, 1966). Other authors have focused their attention on developing theoretical models of turbulent fountains based on the conservation of the fluxes of volume, momentum and buoyancy (Bloomfield and Kerr, 2000; Carazzo et al., 2010). Most of this literature assumes that the fountain is located in an unconfined, quiescent environment.

To further our understanding of the operation of heating and ventilation systems, or the transport of pathogens and particles in rooms and buildings, some authors have presented studies on turbulent fountains in confined environments (Baines et al., 1993, 1990; Lin and Linden, 2005; Mingotti and Woods, 2015a,b). In these studies, the return flow of the fountain is allowed to accumulate and form a filling-box flow growing past the fountain, thereby changing the effective environment of the fountain. The width of the confinement in these studies, however, is many times larger than the width of the fountain, so that the rise height and the entrainment into the fountain are not affected by the confinement.

In this chapter we present novel experiments on extremely confined turbulent fountains to investigate the threshold at which the presence of the confinement does affect the rise height and entrainment of the fountain. We quantify this threshold in terms of the ratio of the width of the confinement surrounding the fountain, W_C, and the diameter of an unconfined single-phase turbulent fountain for given source fluxes of buoyancy and momentum, D_{SPF}. This diameter is proportional to the height of the unconfined fountain with a constant of proportionality of 0.34 (Mizushina et al., 1982). An empirical law for the height of an unconfined turbulent single-phase fountain was found through experiments to be

$$H_{SPF} = 1.84\, M_0^{3/4} |B_0|^{-1/2} \tag{5.1}$$

where M_0 and B_0 are the source fluxes of buoyancy and momentum (Hunt and Burridge, 2015; Turner, 1966). The source fluxes of volume, momentum and buoyancy are

$$Q_0 = \pi b_0^2 u_0; \qquad M_0 = Q_0 u_0; \qquad B_0 = g_0' Q_0 \tag{5.2}$$

where u_0 is the source exit velocity, b_0 is the source radius, and g_0' is the reduced gravitational acceleration at the source (Hunt and Burridge, 2015).

In the experiments presented in this chapter the source Reynolds number, Re_0, ranges between 1400 and 3000 and the source Froude number, Fr_0, ranges between 15 and 30. For this regime, an empirical relation for the total entrainment of ambient fluid into the fountain, Q_{SPF}, was found through experiments by Burridge and Hunt (2016)

$$Q_{SPF} = Q_0(1 + 0.71 Fr_0). \tag{5.3}$$

Equation 5.3 is in very good agreement with the scaling proposed by Mingotti and Woods (2016) for the volume flux of an unconfined fountain

$$Q_{SPF} = (1.07 \pm 0.26)\frac{M_0^{5/4}}{B_0^{1/2}}. \tag{5.4}$$

For the present experiments, the predictions of equations 5.3 and 5.4 differ by less than 8 %.

In this chapter we systematically vary the confinement ratio,

$$W_C/D_{SPF}, \tag{5.5}$$

between 0.6 and 34. This allows us to identify a threshold value of the confinement ratio above which the fountain height and the total entrainment into the fountain remain unaffected by the presence of the confinement. This finding may serve as a reference to other researchers for sizing experimental equipment, but it also allows for insights into the mixing provided by turbulent fountains. Adjusting the source fluxes or the width of the confinement would allow the operator to carefully control the density of the fountain return flow. We present scaling arguments for the entrainment of turbulent fountains in extremely narrow tanks.

5.3 Experimental method

Turbulent axisymmetric fountains are generated by issuing a dense salt water solution upwards through a round nozzle into a tank of width 128 cm, height 80 cm and depth 78 cm, filled with fresh water. A schematic of the experimental set-up is shown in figure 5.1 (a). The diameter of the nozzle is 3.8 mm and the outlet of the nozzle is located 25 cm above the base of the tank, as illustrated in figure 5.1 (b). Six confining tanks of width W_C, open at top and bottom, were manufactured from transparent Perspex. The height of the confining tanks is 30 cm. The four largest confining tanks were constructed with a square cross-sectional area to avoid distortion of the recorded images by curved surfaces. The widths of these four square confining tanks, W_C, are 15 cm, 12.5 cm, 10 cm and 7.5 cm. The two remaining smaller confining tanks were made from circular pieces of Perspex pipe. The diameters of these confining tanks are 4.4 cm and 3 cm. The centre lines of these confinements are aligned with the centre line through the nozzle.

The saline solution is pumped with a *Watson Marlow* peristaltic pump. In all experiments, the density of the source fluid is kept constant, with a reduced gravitational acceleration of $g_0' = 0.32\,\mathrm{m/s^2}$. The source fluxes of momentum and buoyancy are altered by adjusting the source volume flux, as listed in table 5.1.

A *JAI 5000-C* camera is employed to record images of the 21 experiments at a frame rate of 1 Hz. Images are recorded until the filling-box flow has grown past the height of the nozzle. The length of individual experiments therefore varies between 15 and 60 minutes.

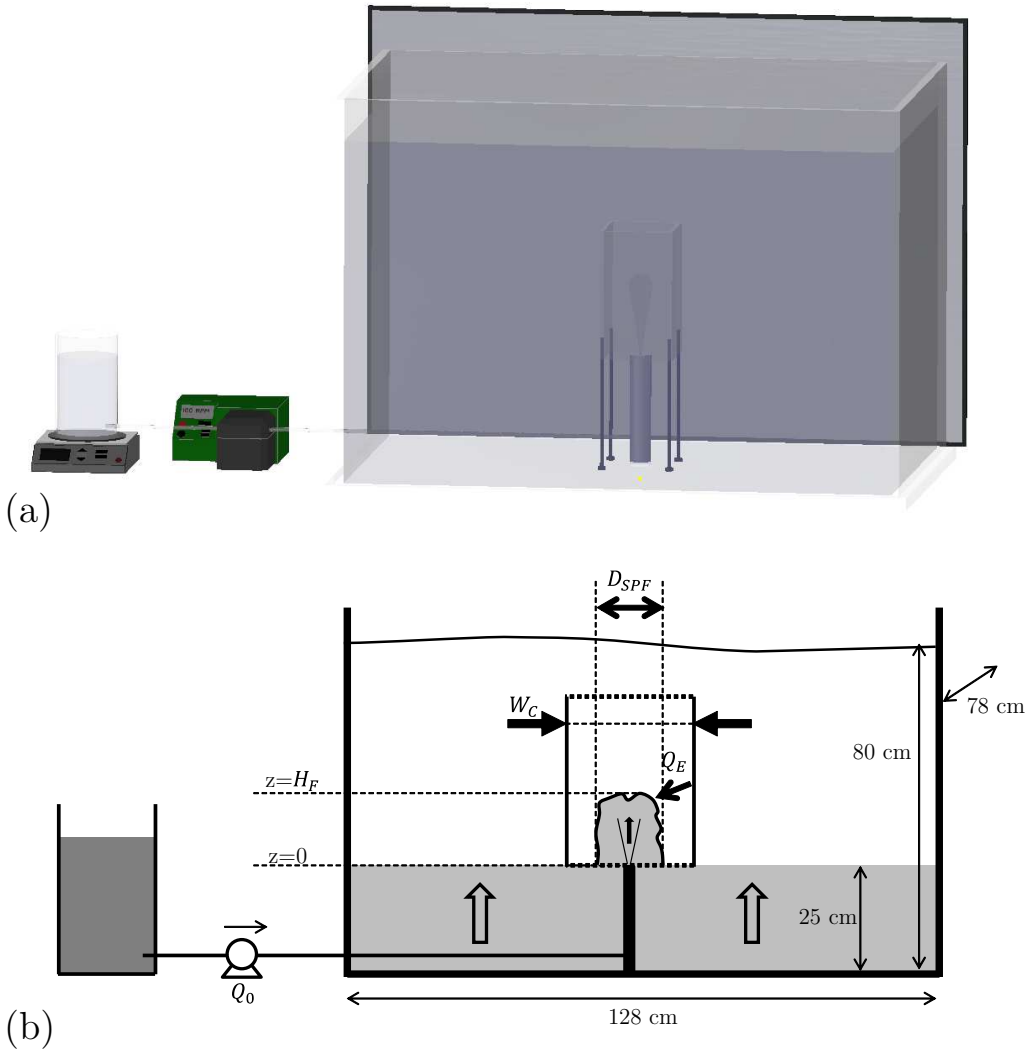

Fig. 5.1 (a) CAD drawing of the experimental apparatus. The peristaltic pump (green) pumps dense liquid from a source bucket (to the left) through a nozzle into a large tank (to the right), illuminated by a light sheet. (b) Schematic of the experimental set-up. The dense fountain liquid collapses and accumulates at the bottom of the tank and forms a dense filling-box layer, which gradually grows into the tank. The relevant dimensions and labels are given in the figure. D_{SPF} is the width of an unconfined fountain and W_C is the width of the confining tank.

$Exp.$ [−]	Q_0 $[ml/s]$	Fr_0 [−]	Re_0 [−]	H_{SPF} $[cm]$	D_{SPF} $[cm]$	Q_{SPF} $[ml/s]$	W_C $[cm]$	$\frac{W_C}{D_{SPF}}$ [−]	H_{Exp} $[cm]$	Q_{Exp} $[ml/s]$
1	4.13	15	1429	6.9	2.4	47.6	79	33.5	6.76	54.6
2	4.13	15	1429	6.9	2.4	47.6	7.5	3.2	7.46	56.6
3	8.11	29	2805	13.6	4.6	176	79	17.1	12.0	169
4	8.11	29	2805	13.6	4.6	176	7.5	1.6	12.1	92.6
5	6.14	22	2123	10.3	3.5	102	79	22.5	10.2	125
6	6.14	22	2123	10.3	3.5	102	7.5	2.1	9.61	67.0
7	4.13	15	1429	6.9	2.4	47.6	3	1.3	5.23	170
8	6.14	22	2123	10.3	3.5	102	3	0.9	6.53	18.2
9	8.11	29	2805	13.6	4.6	176	3	0.6	7.21	18.0
10	4.13	15	1429	6.9	2.4	47.6	4.4	1.9	6.13	31.1
11	6.14	22	2123	10.3	3.5	102	4.4	1.3	8.28	35.0
12	8.11	29	2805	13.6	4.6	176	4.4	1.0	8.76	40.0
13	4.13	15	1429	6.9	2.4	47.6	12.5	5.3	6.51	47.5
14	6.14	22	2123	10.3	3.5	102	12.5	3.6	11.7	142
15	8.11	29	2805	13.6	4.6	176	12.5	2.7	13.9	184
16	4.13	15	1429	6.9	2.4	4.76	10	4.2	6.46	50.5
17	6.14	22	2123	10.3	3.5	102	10	2.9	11.1	110
18	8.11	29	2805	13.6	4.6	176	10	2.2	13.1	138
19	4.13	15	1429	6.9	2.4	47.6	15	6.4	6.57	43.2
20	6.14	22	2123	10.3	3.5	102	15	4.3	10.2	112
21	8.11	29	2805	13.6	4.6	176	15	3.2	13.1	207

Table 5.1 Table with source conditions: Number of the experiment (Exp.), source volume flux (Q_0), source Froude number (Fr_0), source Reynolds number (Re_0), height of an unconfined fountain (H_{SPF}), diameter of an unconfined fountain (D_{SPF}), total volume flux entrained by an unconfined fountain (Q_{SPF}), width of the confining tank (W_C), ratio of the width of the confinement and the diameter of an unconfined fountain (W_C/D_{SPF}), measured height of the confined fountain (H_{Exp}), and measured total entrainment into the confined fountain (Q_{Exp}). In all experiments the nozzle diameter was 3.8 mm and the reduced gravitational acceleration of the dense liquid issuing upwards through the nozzle has a value of $g'_0 = 0.32\ m/s^2$. The nozzle was located 25 cm above the base of the tank.

5.4 Experimental observations

The schematic of the experimental apparatus in figure 5.1 (b) illustrates a fountain located inside a confinement of width W_C. Without the confinement, the fountain would reach a steady-state rise height H_{SPF}. The presence of the confinement, however, may affect this rise height, so that the new rise height inside the confinement is H_F.

The fountain liquid issuing through the nozzle decelerates owing to (i) the negative buoyancy of the fluid, and (ii) the entrainment of ambient liquid, so that the fountain flow runs out of momentum at some overshoot height before the fountain collapses. After this collapse, the fountain no longer entrains uncontaminated ambient fluid, but instead entrains the more dense return flow. This leads to a reduction in fountain height to the quasi-steady fountain height (Hunt and Burridge, 2015; Turner, 1966).

In the present experiments, the fountain return flow accumulates at the bottom of the tank with a horizontal cross-sectional area of 1 m^2. This fluid forms a well-defined dense layer at the bottom of the tank, which subsequently grows upwards as a filling-box flow, fed by the fountain return flow. Figure 5.2 contains 7 panels, each with a cartoon of the fountain flow to the left and an image of the tank to the right. The fountain fluid in these images was dyed red, and the image was extracted at the exact time when the background filling-box flow reached the height of the nozzle. At this point, the fountain height is still unaffected by the filling-box flow, and the volume flux of the filling-box flow corresponds exactly to the total return flow of the fountain at the height of the nozzle. This total return flow, Q_{Exp}, is the sum of the source volume flux, Q_0, and the total entrained volume flux, Q_E.

In all experiments listed in table 5.1, the dyed dense layer, fed by the fountain return flow, remained confined to the region in the tank below the nozzle height for at least the first 11 minutes of each experiment. At the start of a new experiment, it took less than 1 minute for the fountains to adjust to the quasi-steady rise height, H_F. This fountain height, averaged over 10 minutes from minute 1 to minute 11, therefore remained unaffected by the filling-box flow and was extracted automatically from time-series images constructed from a vertical line of pixels through the fountain centre. Such a time-series image is shown in false-colour for experiment 13 in figure 5.3. Blue colour denotes the absence of dyed fountain fluid, red colour denotes a high concentration of this

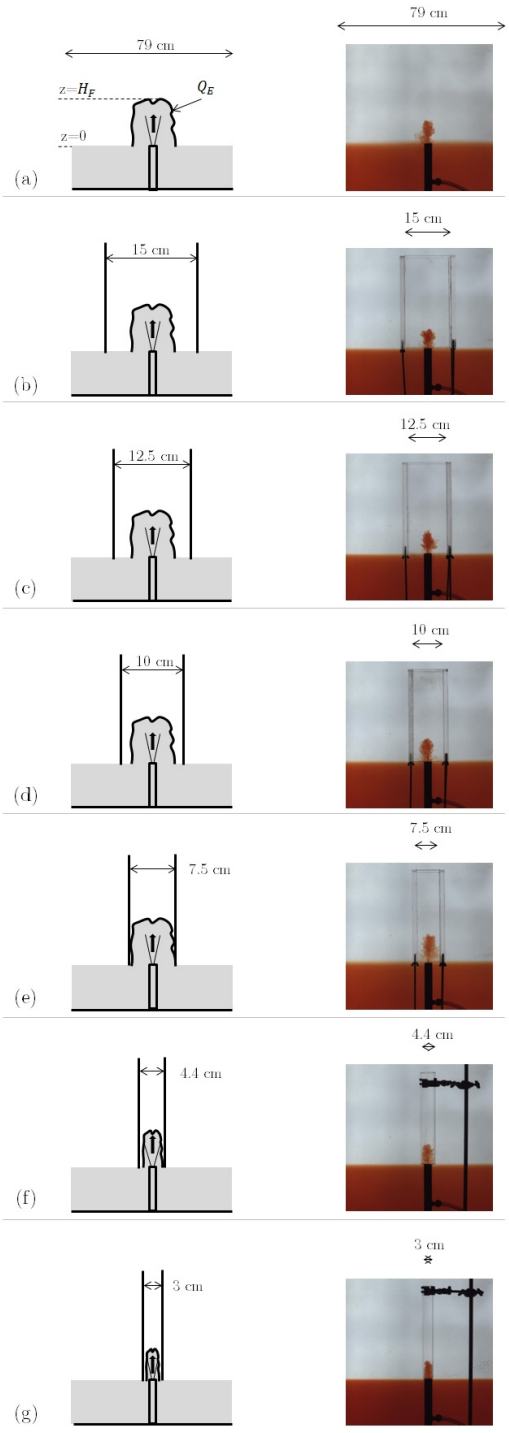

Fig. 5.2 A schematic with 7 panels. Each panel contains a cartoon to the left and a frame from the experiment to the right. This frame is extracted from the experimental video at the exact point in time when the dense filling-box layer (red) grows upwards past the height of the fountain nozzle. In panel (a), the fountain is unconfined. In panel (b), a perspex confining tank of width 15 cm is placed around the fountain. The width of the confining tank decreases from panel (b) to (g).

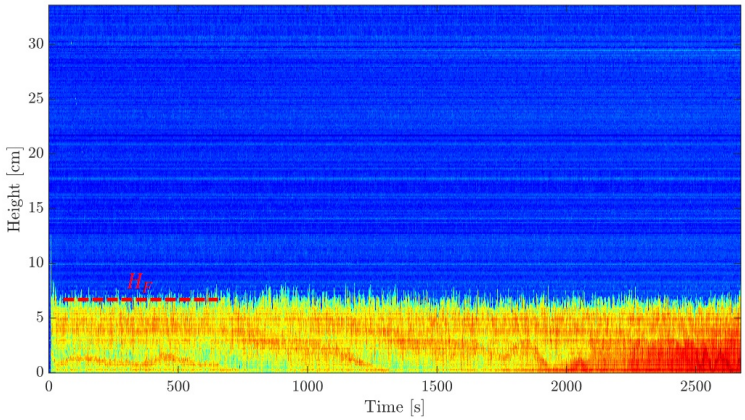

Fig. 5.3 Time-series image of a vertical line through the fountain centre for experiment 13 listed in table 5.1, presented in false-colour. The point of Height = 0 cm corresponds to the nozzle outlet. In this particular experiment, the fountain occupied the region up to a height of approximately 7 cm. The fountain height oscillates around this mean fountain height, H_F. The colour-coding is a measure of the light-intensity recorded by the camera. Blue colour represents an absence of fountain fluid, red colour represents a high concentration of dense fountain fluid.

more dense liquid. The extracted averaged fountain height is illustrated as a dashed red line at a height of approximately 7 cm from minute 1 to minute 11.

The steady-state fountain height was extracted from the experimental videos for all experiments listed in table 5.1 and the measured heights are presented in column H_{Exp}. To investigate if this measured height is affected by the presence of the horizontal confinement, we compute the ratio of the experimental height and the unconfined steady-state height, H_{Exp}/H_{SPF}. In figure 5.4 we plot this height ratio as a function of the confinement ratio, W_C/D_{SPF}. We note that for $W_C/D_{SPF} > 2$, the experimental heights of the fountains are in good agreement with the empirical fit for analogous unconfined fountains, highlighted by the dashed line at a dimensionless height of one. For $W_C/D_{SPF} < 2$, however, we observe a monotonic decrease of the height ratio for smaller values of the confinement ratio. The data points in figure 5.4 correspond to a threshold value in light intensity of 0.5, and the error bars describe the heights obtained for light intensity thresholds of 0.25 and 0.75 (cf. figure 5.3).

The volume flux in the down-flow of the fountain exiting the base of the confining tank can be measured by tracking the velocity of the filling-box flow growing upwards from the base of the reservoir. When this filling-box flow

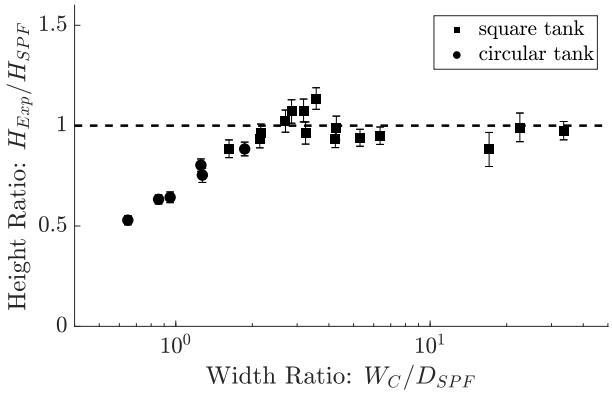

Fig. 5.4 Ratio of experimentally measured fountain height and the fountain height reached by an equivalent unconfined single-phase fountain, H_{Exp}/H_{SPF}, plotted as a function of the ratio of the width of the confinement and the diameter of an unconfined single-phase fountain for the given source fluxes of buoyancy and momentum, W_C/D_{SPF}. The dashed line, at a dimensionless height of one, illustrates the line of exact agreement. The error bars account for different light intensity thresholds (cf. figure 5.3).

reaches the height of the nozzle, the upward filling-box flow exactly matches the downward return flow (cf. figure 5.1 (b)). The propagation of the filling-box flow may be tracked by constructing a time-series image of a horizontally-averaged section outside of the fountain confinement. In our investigation we average the background flow over a horizontal distance of 20 cm to the left of the fountain confinement. A time-series image of the filling-box flow, recorded for experiment 9, is shown in figure 5.5. Blue colour denotes the absence of the layer and red denotes a high concentration of the dyed dense fountain fluid.

In figure 5.5, the height of the nozzle is illustrated by a dashed white line. We note that this line is not located at a height of 25 cm as the images were cropped. The slope of the colour contours in figure 5.5 corresponds to the velocity of the filling-box front. The product of this velocity at the height of the nozzle and the cross-sectional area of the tank gives an experimental estimate of the fountain down-flow, Q_{Exp}. The slope of the light intensity contour of 0.5 at the height of the nozzle is shown as a dashed red line in figure 5.5.

To investigate if the volume of fluid entrained by the fountain is affected by the presence of the confinement, we compute the ratio of our experimental measurement of the return flow and the empirical estimate for an analogous unconfined fountain, Q_{Exp}/Q_{SPF}. This entrainment ratio is plotted as a function of the confinement ratio, W_C/D_{SPF}, in figure 5.6. Our experimental

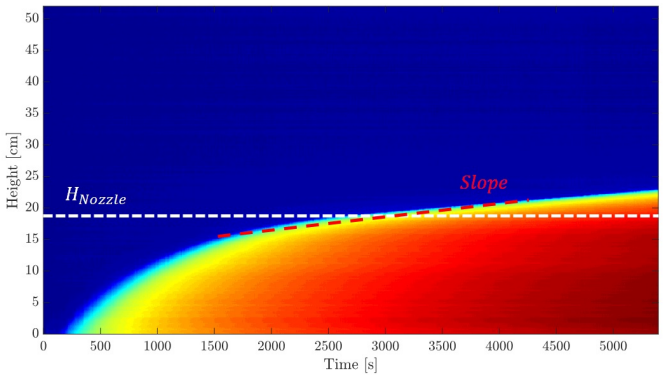

Fig. 5.5 Time-series image of the evolution of the filling-box layer growing upwards from the base of the reservoir, presented in false-colour, for experiment 9. The colour-coding is a measure of the light intensity recorded by the camera. Red colour represents a high concentration of dense fluid. Initially, the ambient is clear, as indicated by the dark blue region from Time = 0 s to Time = 200 s. Subsequently, a filling-box flow develops, which grows past the nozzle height (dashed white line) after approximately 3000 s. The slope of the contour between the neutrally buoyant ambient liquid (blue) and the dense liquid (yellow-red) corresponds to the filling-box velocity of the ascending front.

data suggests that the fountain entrainment remains unaffected by the presence of the confinement for $W_C/D_{SPF} > 2$. As for the height ratio, we observe a monotonic decrease if the entrainment ratio, W_C/D_{SPF}, decreases below the threshold value of 2. The dashed line in figure 5.6 has a dimensionless height of one and illustrates the entrainment expected for an unconfined fountain. The data points in figure 5.6 were obtained by considering the slope of the light intensity contour extracted at a light intensity value of 0.5. Similarly, the error bars correspond to light intensity thresholds of 0.25 and 0.75 (cf. figure 5.5).

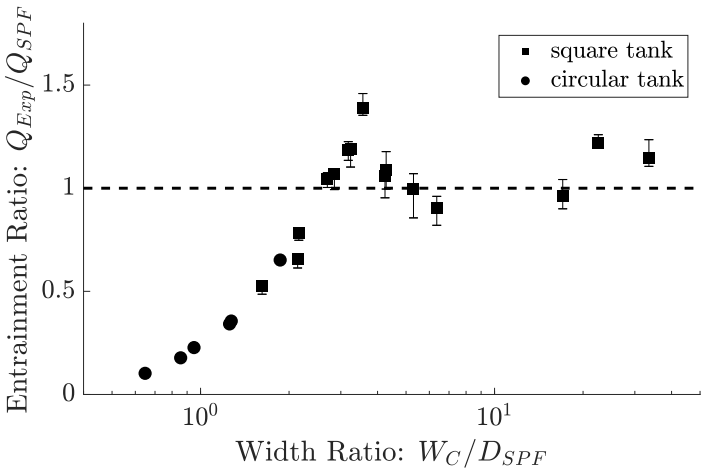

Fig. 5.6 Ratio of experimentally measured fountain entrainment and the empirical estimate of the entrainment into an equivalent unconfined single-phase fountain, Q_{Exp}/Q_{SPF}, plotted as a function of the ratio of the width of the confining tank and the diameter of an unconfined single-phase fountain with the given source fluxes of buoyancy and momentum, W_C/D_{SPF}. The dashed line, at a dimensionless height of one, illustrates the line of exact agreement. The error bars account for different light intensity thresholds (cf. figure 5.5).

5.5 Scaling for confined fountain

The volume flux entrained by unconfined turbulent fountains depends on the source fluxes of buoyancy and momentum, according to equation 5.4. This equation, however, is only appropriate if the confinement ratio (cf. equation 5.5) exceeds a value of 2. For smaller values of the confinement ratio we observe a decrease in total entrainment, as illustrated by figure 5.6. We now proceed by investigating the controls on the entrainment ratio for these confined fountains ($W_C/D_{SPF} < 2$).

The radius of a circular confinement corresponds to half the width of the confinement, $R_C = W_C/2$, so that the cross-sectional area of the confinement is $A_C = \pi R_C^2$. The confinement is filled with dense fluid up to the measured rise height of the fountain, H_{Exp}. The fluid surrounding the fountain is well-mixed and the velocity of the outflow at the bottom of the tube scales as $\sqrt{g'_C H_{Exp}}$. Hence, the volume flux leaving the confinement through the open base is

$$Q_C = \pi R_C^2 \gamma \sqrt{g'_C H_{Exp}} \tag{5.6}$$

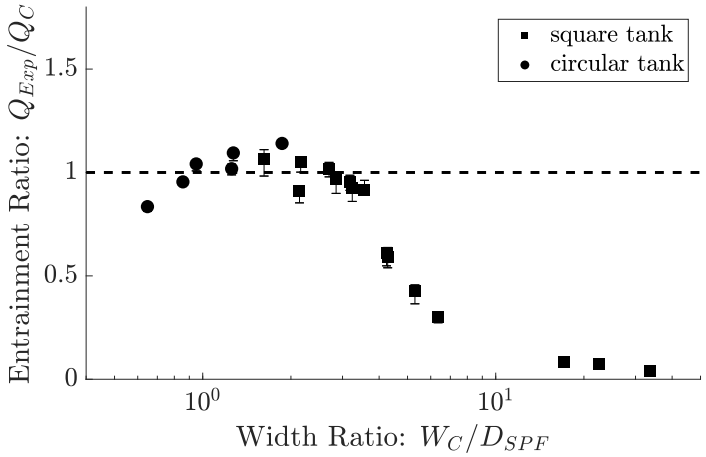

Fig. 5.7 Ratio of experimentally measured fountain entrainment and the estimate of the entrainment into an extremely confined fountain, Q_{Exp}/Q_C, plotted as a function of the ratio of the width of the confinement and the diameter of an unconfined single-phase fountain, W_C/D_{SPF}. The dashed line, at a dimensionless height of one, illustrates the line of exact agreement. The error bars account for different light intensity thresholds (cf. figure 5.5).

where γ is a constant. Similarly, the buoyancy flux through the base of the confining tank is

$$B_C = B_0 = \pi R_C^2 g'_C \gamma \sqrt{g'_C H_{Exp}}, \tag{5.7}$$

which corresponds to the source buoyancy flux B_0. Equation 5.7 can be solved for g'_C so that equation 5.6 can be written as

$$Q_C = \pi^{2/3} \gamma^{2/3} R_C^{4/3} B_0^{1/3} H_{Exp}^{1/3}. \tag{5.8}$$

In figure 5.7 we compare this estimate of the total fountain volume flux with our experimental data by plotting the ratio of Q_{Exp} and Q_C as a function of the confinement ratio, W_C/D_{SPF}. For values of this entrainment ratio smaller than 4, the experimental data is in good agreement with the estimate of equation 5.8 for a value of $\gamma = 0.33 \pm 0.05$.This suggests that this scaling, based on the geometry of the confinement and conservation of buoyancy, captures the physics controlling the entrainment of extremely confined turbulent fountains.

The Reynolds number of the down-flow exiting the base of the confining tank, based on the velocity of the down-flow, u_C, and the radius of the confining tank, R_C, is

$$Re_C = \frac{u_C R_C}{\nu}, \tag{5.9}$$

where ν is the kinematic viscosity of the fluid. In the present experiments, this Reynolds number ranges from 300 to 1000, indicating that the drag exerted by the walls of the confining tank may act to slow the down-flow. The force balance on this down-flow is between the buoyancy force, F_B, and the drag force exerted by the confining walls, F_D. For a circular cross-sectional area with radius R_C, and a height of the dense fluid inside the tube H, these two forces are

$$F_B = \Delta\rho g \pi R_C^2 H \quad \text{and} \quad F_D = C_D \frac{1}{2} \rho u_C^2 2\pi R_C H, \tag{5.10}$$

where C_D is a drag coefficient. Equation 5.10 can be re-arranged for the velocity of the down-flow of the fountain exiting through the base of the confining tank,

$$u_C = \sqrt{\frac{1}{C_D}\frac{R_C}{H}}\sqrt{g'_C H} = \gamma\sqrt{g'_C H}, \tag{5.11}$$

suggesting that $\gamma = \sqrt{\frac{1}{C_D}\frac{R_C}{H}} \approx 0.33$. The description of the drag force in equation 5.10 only accounts for the drag exerted by the walls of the confining tank. There is an additional drag force exerted on the down-flow by the jet-like up-flow in the fountain core. The presence of this counter-flow also reduces the area available for the down-flow. This is not included in this model. The presence of the drag force, providing resistance to the fountain down-flow, rationalises why the velocity of the down-flow, exiting through the base of the confining tank, is smaller than expected from a Bernoulli argument.

5.6 Summary

In this chapter we presented an experimental investigation of the effects of horizontal confinement on the rise height and the total entrainment of turbulent single-phase fountains. Our experimental data suggests that both the rise height and the entrainment into the fountain remain unaffected by the presence of the confinement if the width of the confinement exceeds the diameter of the fountain by a factor of 2 or more. For smaller values of the ratio of confinement width and fountain diameter, we observe that both the fountain height and the

fountain entrainment decrease monotonically. We developed a scaling argument for the entrainment of extremely confined fountains.

Chapter 6

Particle-driven gravity currents

6.1 Abstract

We present an experimental investigation of steady particle-driven gravity currents with Reynolds numbers in the range 500 to 1600, and with the ratio of the initial current speed to the fall speed of the particles, $S = u_0/u_{fall}$, in the range $5 < S < 160$. We identify three regimes:

(i) For $S < 10$, the particles settle close to the source at a velocity corresponding to their fall speed, consistent with the observation of sedimenting fronts in classical settling column experiments.

(ii) In the range $10 < S < 40$, a steady gravity current develops within the tank. The experiments show that the depth of the gravity current gradually decreases away from the source and dye added to the source liquid appears above the gravity current along its entire length, suggesting that there is a sedimentation front, so that the volume and momentum fluxes of the current gradually decrease with distance from the source. We find that as S increases, the descent speed of the sedimentation front decreases relative to the fall speed of the particles, and the run-out length of the gravity current increases. We note that the density of the interstitial fluid corresponds to the density of the ambient fluid, so that any reduction in buoyancy of the gravity current is attributed to the sedimentation of particles on the floor of the tank and we do not observe lofting of the interstitial fluid.

(iii) For $40 < S < 160$, the gravity currents reach the end of our experimental tank and we no longer observe a sedimentation front. For these experiments, it appears that the entrainment at the top of the current begins to match the

sedimentation and so the current depth does not change significantly over the scale of the tank, but a larger scale experimental system would be needed to explore the full run-out behaviour for these larger values of S.

For the intermediate case, $10 < S < 40$, we develop a model for the conservation of volume, momentum and buoyancy fluxes in the current, accounting for the sedimentation front and the release of fluid at the top surface of the gravity current, and we compare this with our new experimental data.

6.2 Introduction

Continuous particle-driven gravity currents frequently occur in nature and industry. In nature, examples include pyroclastic flows issuing from volcanoes, sustained turbidity currents and the continuous discharge of particles into lakes and oceans by sediment-laden rivers (Bonnecaze et al., 1993; Middleton, 1993; Simpson, 1999; Steel et al., 2016; Ungarish, 2009). In the oil and gas industry, the process industry, and in water treatment facilities, separators are employed to split continuous streams of multiphase mixtures into their single-phase components (DeRooij, 1999). Understanding the run-out distance and sedimentation from these flows, as well as the fate of the host fluid, is important to optimise industrial equipment and to assess the hazards posed by naturally occurring particle-driven currents, especially since contaminants on the particles may become dissolved in the host fluid.

In the sedimentology literature, there is a wealth of papers exploring the sedimentation of particles in settling columns (Davis and Acrivos, 1985; Kynch, 1952), and often the effects of hindered settling lead to dispersal of the sedimentation front (Blanchette and Bush, 2005; Guazzelli and Hinch, 2011).

There is also significant literature exploring the dynamics of particle-laden gravity currents, arising from the original work of Von Karman (1940) and Benjamin (1968). Many authors have explored the dynamics of finite-volume gravity currents produced by the release of a fixed volume of fluid from a lock gate. Models of these flows often assume that the flow maintains a constant volume (Bonnecaze et al., 1993; Huppert, 1998, 2006; Simpson, 1999; Ungarish, 2009). For such particle-laden gravity currents, the concentration is then assumed to decrease through sedimentation from the base of the flow, while the current is often assumed to remain well-mixed at each position along the flow and the effects of any sedimentation front are ignored (Bonnecaze

et al., 1993). These simplifications have been successful in developing models to describe the position of the nose of the current as a function of time in the case that the current speed far exceeds the particle settling velocity, $u(x) >> u_{fall}$. Given that sedimentation fronts do develop in settling columns, it is of interest to explore if there are conditions under which a sedimentation front develops in gravity-driven flows, and to explore the fate of the host fluid as the particles sediment. In our investigation, the density of the interstitial host fluid corresponds to the density of the ambient fluid, so that any reduction in buoyancy of the gravity current is attributed to the sedimentation of particles on the floor. We note that if the density of the host fluid exceeds the density of the ambient fluid, the overall density and thus the velocity of the gravity current would increase. The host fluid would continue to travel as a single-phase gravity current after the particles have sedimented. Conversely, if the interstitial host fluid is less dense than the ambient fluid, the overall buoyancy of the gravity current would be reduced and the gravity current would lose buoyancy through the sedimentation of particles as well as through the escape of host liquid at the top of the gravity current. Depending on the magnitude of the density difference between host fluid and ambient fluid, and the size and density of the particles, the lofting interstitial fluid may lift particles up from the gravity current (Steel et al., 2017). This complication is beyond the scope of the present study.

We have chosen to study the dynamics of steady particle-driven gravity currents, which are sustained by a maintained source of particle-laden fluid. We explore the conditions under which a sedimentation front develops on the upper surface of the gravity current, and we assess the impact of this on the evolution of the mass and momentum flux of the flow. In our investigation, we assume that the Shields parameter of the flow, $\Theta = \frac{\rho_c u^2}{(\rho_p - \rho_c) g d}$, is sufficiently small, so that the re-suspension of particles from the bed can be neglected (cf. Eames et al. (2001)). ρ_c is the bulk density of the flow, ρ_p is the particle density and d is the particle diameter. u is the velocity of the flow and g is the gravitational acceleration.

First, we present a series of experiments in which steady, particle-driven gravity currents develop from the collapse of turbulent multiphase fountains. This source condition allows for the supply of a continuous volume flux without imposing an initial horizontal momentum to the flow. We measure the depth of the current as a function of position and we use finite pulses of dye in the source

fluid to determine the fate of the fluid as it moves through the current. We also develop a quantitative model for the conservation of the fluxes of volume, momentum and buoyancy. This model accounts for a possible sedimentation front, and, by comparison with our experimental data, we propose that the effective speed of this front decreases as the ratio of the current speed to the fall speed of the particles, S, increases. We consider the implications of our model for the dynamics of particle-laden gravity currents in industry and nature.

6.3 Experimental method

Particle-driven gravity currents were generated by issuing a mixture of fresh water and mono-dispersed Silicon-Carbide particles through a nozzle upwards 10 cm from the end of a Perspex tank with length $L_{tank} = 3$ m long, 40 cm high and 15 cm wide, initially filled with fresh water. The dense, particle-laden jet exiting through the nozzle decelerates owing to its negative buoyancy and the entrainment of ambient liquid. The jet eventually comes to rest and collapses, thereby forming a turbulent multiphase fountain with a source Reynolds number of approximately 2500. This source Reynolds number is based on the density of the injected fluid, ρ_S, and the nozzle diameter, $d_S = 8.6$ mm, as a length scale,

$$Re_S = \frac{\rho_S \, u_S \, d_S}{\mu_W}, \tag{6.1}$$

where $\mu_W \approx 1$ mPa s is the dynamic viscosity of water at room temperature and u_S is the nozzle exit velocity. The density of the source fluid, ρ_S, is proportional to the source concentration of particles, C_S.

A schematic of the experimental set-up is shown in figure 6.1. After an initial transient, the current reaches a steady-state. In this chapter we present a set of 35 experiments, 24 of which were run with a single fountain source. The corresponding experimental set-up is shown in panel (a) of figure 6.1. The second schematic in this panel is a top view of the tank, focusing on the nozzle section to illustrate the positioning of the nozzle. A further set of 8 experiments was run with two fountain sources distributed evenly in the spanwise direction of the tank to double the volume flux. The corresponding experimental set-up is shown in figure 6.1 (b). These experiments are marked with an asterisk (*) in table 6.1. Three additional experiments were run with a plume source, directed downwards and placed 12.5 cm above the base of the tank. Figure

6.1 (c) contains a schematic of this experimental set-up. These experiments are marked with two asterisks (**). In three experiments, the gravity current did not sediment the particle load prior to reaching the end of the tank, and so a steady-state was not reached. These experiments are marked with three asterisks (***). The source liquid, a mixture of fresh water and *Carborex* Silicon-Carbide particles produced by *Washington Mills*, was pumped with a *Watson Marlow* peristaltic pump. The particles have diameters between 13 and 63 μm. The concentration at the source of the fountain was kept between 20 and 80 grams of particles per litre of water. This concentration was further reduced by dilution in the fountain, resulting in gravity currents with initial Reynolds numbers between 500 and 1600. The initial Reynolds number of the gravity current is based on the density of the fluid at the onset of the gravity current, ρ_0, and the initial current height, h_0, as a length scale,

$$Re_0 = \frac{\rho_0 \, u_0 \, h_0}{\mu_W}, \tag{6.2}$$

where u_0 is the initial velocity of the gravity current. Please refer to section 6.5 for a detailed discussion of the initial values of current height, density and velocity. The source Reynolds number, Re_S (equation 6.1), is calculated per nozzle. For the double fountain source, however, the initial Reynolds number of the current, Re_0 (equation 6.2), is calculated based on the added flow rates from the two sources forming the gravity current.

An electroluminescent light sheet was placed behind the tank to provide uniform illumination. Images were recorded with a *JAI 5000-C* camera. The videos, 6.25 minutes in length, have a frame rate of 4 Hz. The steady-state shape of the gravity currents was extracted by time-averaging over the last 2 minutes of the experiments.

In the experiments marked with a subscript b in table 6.1 a burst of red dye was added to the source liquid. The density difference between this water-based dye and the ambient fresh water is much smaller than the density difference between the particle-laden water and the fresh water, so that the effects of the dye on the flow are negligible.

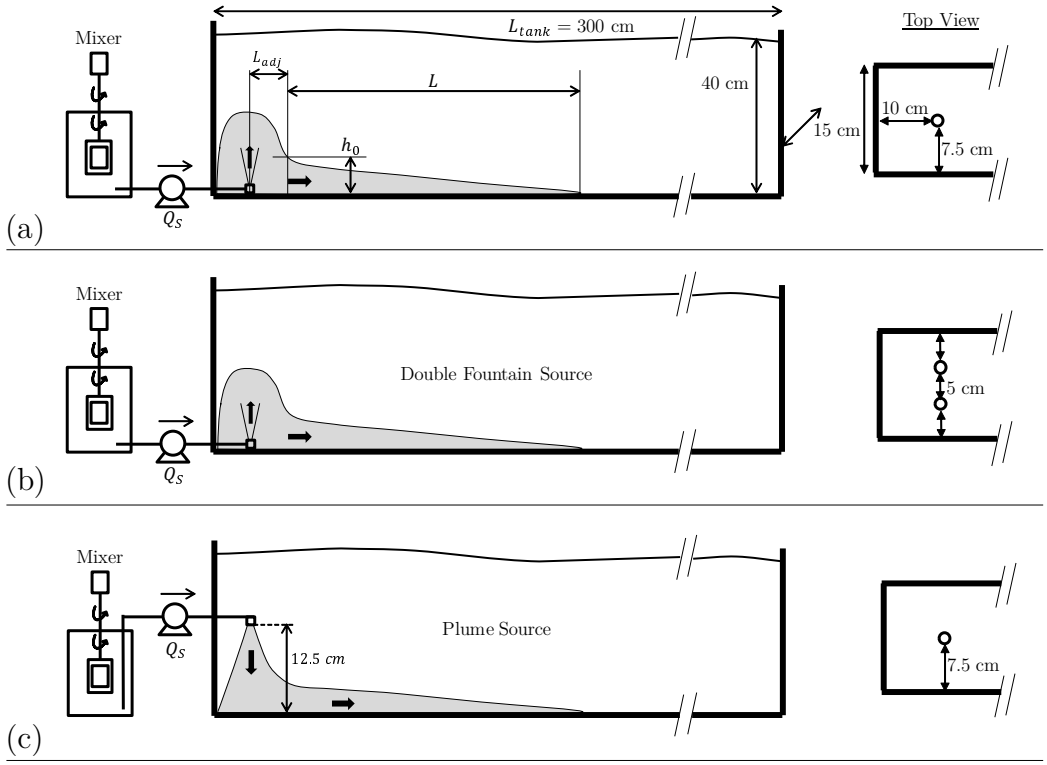

Fig. 6.1 Two-dimensional schematic of the experimental apparatus and cartoon of the transition of the flow from a turbulent fountain or plume into a particle-driven gravity current. The second cartoon in each panel is a top-view of the tank, focussing on the nozzle section to illustrate the nozzle arrangement on a horizontal plane. (a) Single fountain source, (b) double fountain source, and (c) single plume source.

Exp. [−]	d_P [μm]	u_{fall} [mm/s]	$C_{S,SiC}$ [g/L_W]	Q_S [ml/s]	Fr_S [−]	Q_0 [ml/s]	L [cm]	h_0 [cm]	S [−]	Re_0 [−]
1	63	4.78	20	17.0	12	163	13.2	4.4	5	1087
2	63	4.78	40	17.0	9	121	17.5	2.6	7	804
3	45	2.39	20	17.0	12	163	35.6	4.4	10	1087
4	45	2.39	40	17.0	9	121	36.1	2.6	13	804
5	45	2.39	80	17.0	6	90.7	35.7	1.5	16	605
6	37	1.60	20	17.0	12	163	76.7	4.4	15	1087
7	37	1.60	40	17.0	9	121	81.5	2.6	19	804
8	37	1.60	80	17.0	6	90.7	120	1.5	24	605
9	29	1.03	20	17.0	12	163	208	4.4	24	1087
10	29	1.03	40	17.0	9	121	216	2.6	30	804
11***	29	1.03	80	17.0	6	90.7	(253)	1.5	38	605
12*	63	4.78	20	10.5	8	133	15.5	3.3	6	887
13*	63	4.78	40	10.5	5	101	22.8	2.0	7	670
14*	45	2.39	20	10.5	8	133	37.4	3.3	11	887
15*	45	2.39	40	10.5	5	101	40.7	2.0	14	670
16*	37	1.60	20	10.5	8	133	64.3	3.3	17	887
17*	37	1.60	40	10.5	5	101	75.3	2.0	21	670
18*	63	4.73	40	16.9	9	240	61.2	4.1	8	1600
19*	45	2.39	40	16.9	9	240	95.9	4.1	16	1600
20	37	1.60	30	17.0	10	136	59.7	3.2	18	910
21	37	1.60	50	17.0	8	110	65.5	2.2	21	732
22	37	1.60	60	17.0	7	102	70.2	1.9	22	679
23	29	1.03	30	17.0	10	136	139	3.2	28	910
24	29	1.03	50	17.0	8	110	155	2.2	33	732
25	29	1.03	60	17.0	7	102	217	1.9	35	679
26**	45	2.39	60	17.0	7	96.6	45.9	1.8	15	644
27**	37	1.60	50	17.0	8	91.0	73.8	1.8	21	606
28**	29	1.03	30	17.0	10	76.9	123	1.8	28	513
29***	23	0.63	40	17.0	9	121	-	2.6	50	804
30***	13	0.20	40	17.0	9	121	-	2.6	158	804
31_b	63	4.78	20	11.4	8	77.9	-	3.1	5	779
32_b	53	3.38	20	11.4	8	77.9	-	3.1	7	779
33_b	45	2.39	20	11.4	8	77.9	-	3.1	10	779
34_b	37	1.60	20	11.4	8	77.9	-	3.1	15	779
35_b***	13	0.2	20	11.4	8	77.9	-	3.1	126	779

Table 6.1 Table with source conditions: Number of the experiment (Exp.), particle diameter (d_P), particle fall speed (u_{fall}), particle concentration supplied through nozzle (C_S), volume flux supplied through nozzle (Q_S), source Froude number of the fountain (Fr_S), initial volume flux feeding the gravity current (Q_0), run-out length of the gravity current (L), initial height of the gravity current (h_0), ratio of fluid velocity to particle settling velocity, S, and initial Reynolds number of the current (Re_0). In experiments marked with (*) the source was comprised of two nozzles. In experiments marked with (**) the mixture was issued into the tank as a plume (directed downwards), positioned 12.5 cm above the floor. In experiments marked with (***), the currents reached the end of the 3 m flume tank. In experiments with subscript b a burst of red dye was added to the source liquid in steady-state. These experiments were run in a tank 150 cm long and 10 cm deep. The value for Q_0 was computed from equation 6.9 and the initial velocity was obtained via the relation $u_0 = \sqrt{g_0' h_0}$.

6.4 Experimental observations

In the experiments we have systematically varied the size and concentration of the particles, the source fluid volume flux, and the orientation of the source (single fountain source, double fountain source, plume source).

Panel (a) of figure 6.2 shows an instantaneous image of a gravity current (exp. 6) in steady-state. A dark colour indicates a high concentration of particles. The image shows the multiphase fountain to the left. This feeds the gravity current, which gradually thins out over approximately 150 cm. Panel (b) of figure 6.2 shows a two minute time-averaged shape of the gravity current in false-colour. Dark blue indicates a high concentration of particles, red denotes the absence of particles. This time-averaged shape smooths the fluctuations in depth of the current and corresponds to the steady mean shape of the gravity current. The fluctuations, visible in panel (a), lead to a diffuse front in the time-averaged image. Panels (c) to (e) of figure 6.2 show time-series images of the three vertical lines shown in (a) and (b). We interpret the oscillations around a mean depth as the result of apparent turbulent fluctuations in the flow. The mean depth and the particle concentration decrease from panel (c) to panel (e) corresponding to the change in the gravity current as it moves downstream.

In experiments 31-35 we added a finite volume of red dye to the source liquid supplied through the nozzle once the steady current had become established. As the fluid moves along the current, it may be seen that in experiments 31-34 some of the dyed liquid separates from the upper surface of the current (see figure 6.3 (a)-(f) for experiment 33). In panel (a) only the time-averaged shape of the fountain and gravity current (in dark grey) is visible. This figure indicates that fluid detrains from the gravity current into the environment as the particles sediment from the flow. Panels (e) and (f) highlight that the dyed fluid continues to travel along the tank, implying that this liquid also carries momentum away from the gravity current. Panel (g) corresponds to panel (d), but the instantaneous outline of the gravity current is shown, rather than the time-averaged profile.

In figure 6.4 (a) we show the thickness versus distance of 27 experiments. We do not include the three experiments which reach the end of the flume tank. The colour-coding indicates the value of the dimensionless settling parameter,

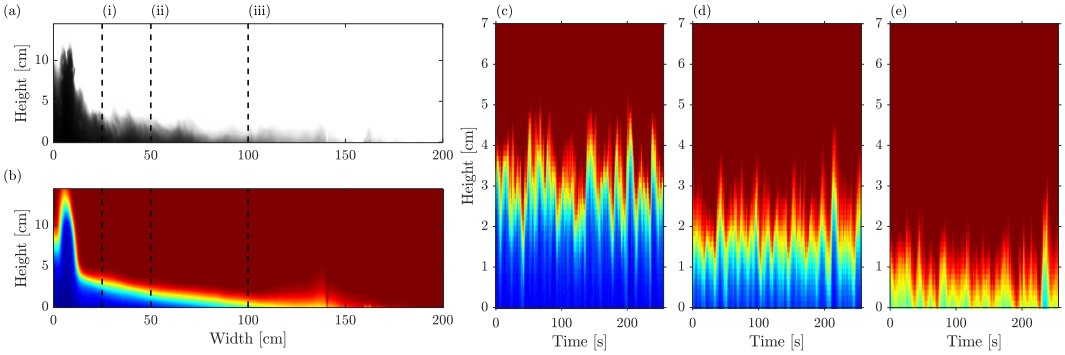

Fig. 6.2 (a) Instantaneous image of the gravity current (exp. 6 in table 6.1). (b) False-colour image of the time-averaged, steady-state shape of the current. Blue colour denotes a high concentration of particles, red colour denotes the absence of particles. (c-e) False-colour time-series images at the locations marked by columns (i), (ii) and (iii) in (a) and (b).

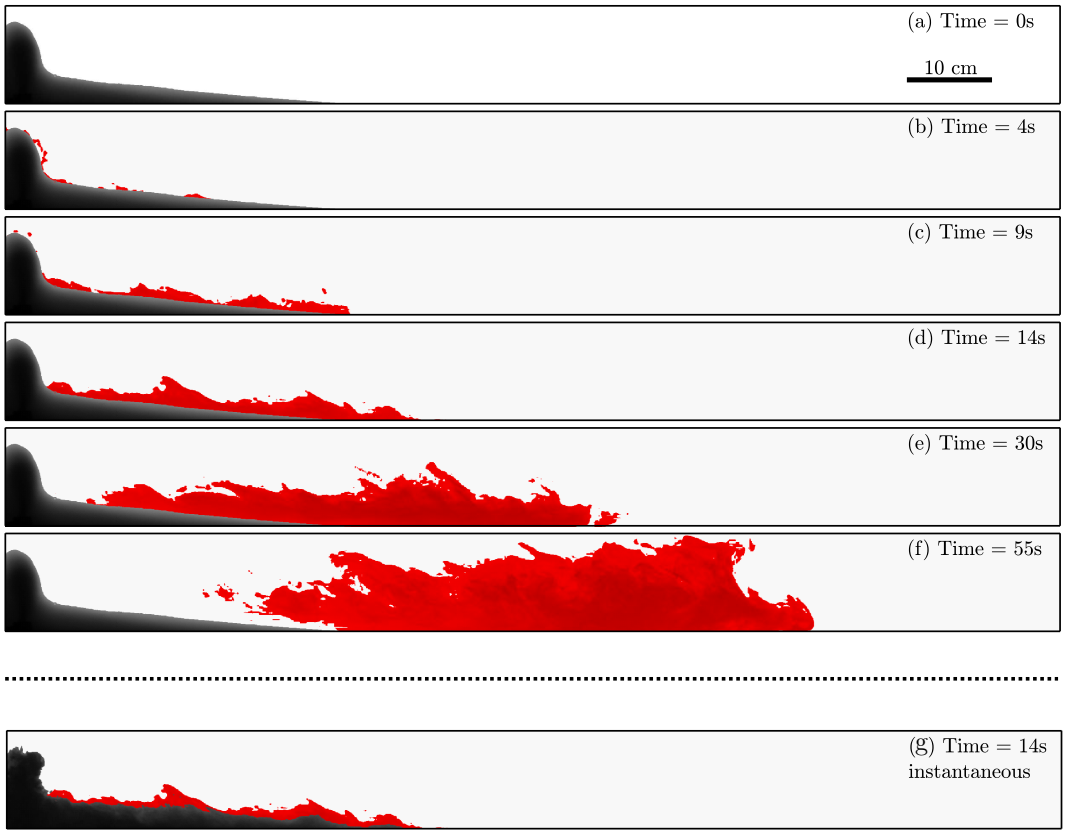

Fig. 6.3 (a) Visualisation of the time-averaged steady-state shape of the gravity current in grey. (b)-(f) A burst of red dye was added to the source liquid to investigate the separation of the source liquid from the gravity current. Red dye emerges above the current, along the entire length of the current. This dyed liquid continues to propagate owing to its residual momentum. (g) Instantaneous shape of the gravity current corresponding to panel (d).

S,

$$S = \frac{u_0}{u_{fall}}, \tag{6.3}$$

where u_0 is the initial velocity of the gravity current and u_{fall} is the terminal fall speed of the particles. Please refer to equation 6.10 for the exact definition of u_{fall}. Dark blue corresponds to $S \approx 5$, and dark red corresponds to $S \approx 30$. This plot shows that the run-out distance and the total area occupied by the gravity current increase for larger values of S. It has previously been shown that the parameter S is crucial for describing the dynamics of transient particle-laden gravity currents produced by a finite release of fluid (Bonnecaze et al., 1993). The depth on the y-axis and the distance travelled on the x-axis are both normalised by the initial depth, h_0. In section 6.5 we give a detailed description of the initial velocity u_0 and depth h_0.

We note that in experiment 35, obtained for $S = 126$, we did not observe a reduction in height of the gravity current along the entire length of the tank and the dye remained confined to the gravity current.

Panel (b) of figure 6.4 shows a cartoon describing the processes within the gravity current. The current is fed by the fountain, which supplies an initial volume flux per unit width, $q_0 = u_0 h_0$, as well as an initial particle volume fraction, C_0. As particles settle there is a reduction in depth of the current, and some deposition of particles at the base of the tank. The reduction in depth releases some of the fluid from the upper surface of the current. However, the apparent turbulent fluctuations (figure 6.2) lead to some mixing near this interface so that the rate of decrease of depth of the current is smaller than the fall speed of the particles. These turbulent fluctuations are likely to arise owing to the small density gradient between the top of the propagating gravity current and the ambient as the particles begin to settle from the top of the gravity current. This shear-driven mixing, in turn, leads to a reduction in the speed of the sedimentation front to values smaller than the fall speed of the particles. Owing to the low concentration of particles ($C_0 < 0.5\%$ by volume) it is likely that convective mixing, caused by convective particle settling, is negligible (Hoyal et al., 1999). Owing to the change in density of the upper parts of the current associated with the sedimentation, the entrainment process is different to the mixing of ambient fluid into continuous single-phase gravity currents. In a single-phase gravity current, mixing occurs predominantly near the head of the current, while the density gradient between the tail of the

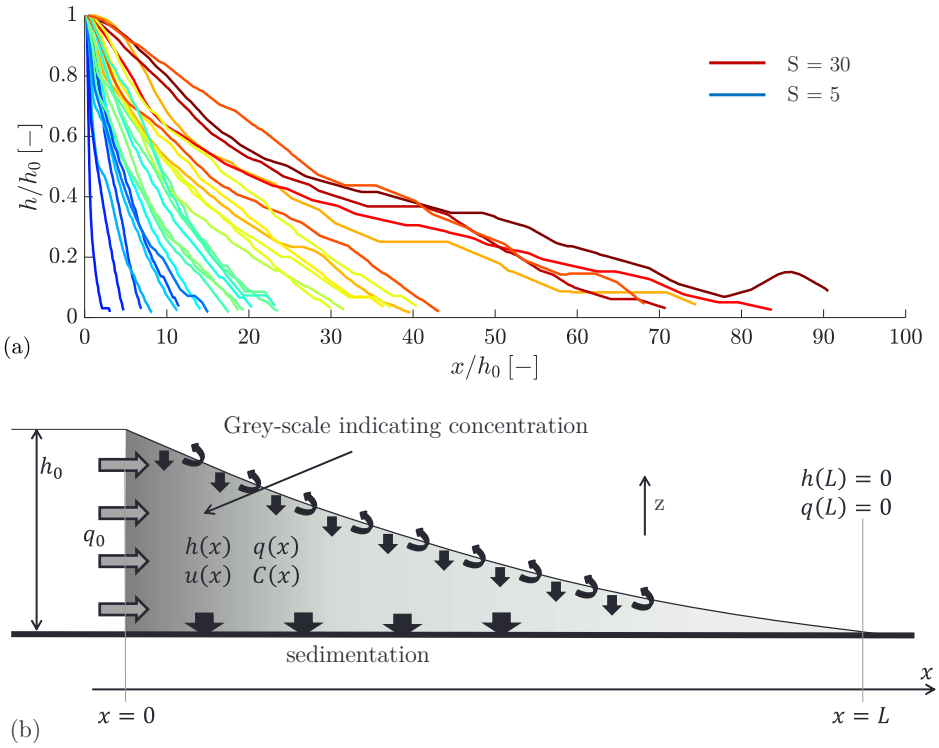

Fig. 6.4 (a) Plot of dimensionless depth as a function of dimensionless distance from the source for 27 experiments (experiments marked with (***) were excluded). The depth and the horizontal distance are normalised by h_0. (b) Cartoon of a particle-laden gravity current in steady-state. The particle concentration, $C(x)$, the volume flux, $q(x)$, and the depth of the current, $h(x)$, decreases with distance from the source.

gravity current and the ambient limits the mixing behind the head (Sher and Woods, 2017).

From the contours of the gravity currents displayed in figure 6.4 (a) one can extract the run-out distance of the gravity current, L, defined as the horizontal distance from the source, at which $h = h_0$, to the point where $h = 0$. These contours were obtained from the time-averaged gravity current profiles (cf. figure 6.2 (b)). In estimating the run-out distance, there is some variability in the exact distance owing to the fluctuations in the flow; we have included some estimate of this variability by comparing the location of the run-out lengths estimated from the time-averaged images of the flow, using the light-intensity contour of 0.4, with error bars representing the distances reached by light intensity contours of 0.3 and 0.5 (see figure 6.2). The run-out distance, L, normalised by the initial height, h_0, is shown as a function of S in figure 6.5 (a), demonstrating that the run-out length increases as either the initial current speed increases or the particle fall speed decreases. The dash-dotted line in this figure corresponds to a power-law best-fit of our experimental data in the form

$$\frac{L}{h_0} = a\, S^b \tag{6.4}$$

with a = 0.048 and b = 2.2. The coefficient of determination, R^2, of this fit is 0.92.

For simple settling, the time required for a particle to fall from the top of the gravity current to the floor is $\tau_{fall} = h_0/u_{fall}$, while we expect the travel time of the particle from the source to the end of the gravity current to scale as $\tau_{travel} = L/u_0$. In figure 6.5 (b) we plot the ratio of τ_{fall} and τ_{travel}, measured in our experiments, as a function of S, and we observe that this ratio decreases for larger values of S. We note that for $S > 40$, we do not in fact observe a reduction in depth over the entire length of the 3 metre flume tank (experiments marked with (***)). These data suggest that the effective descent speed of the sedimentation front, u_{front}, decreases relative to the fall speed of individual particles, u_{fall}, as S increases. We hypothesise that the reduction of the apparent fall speed of the sedimentation front results from the increasing importance of the mixing near the top surface of the current as the current speed increases to values far in excess of the settling speed of the particles (cf. Cardoso & Woods (1995)). The dash-dotted line corresponds to the power-law best-fit shown in panel (a). On this plot, this best-fit has the form

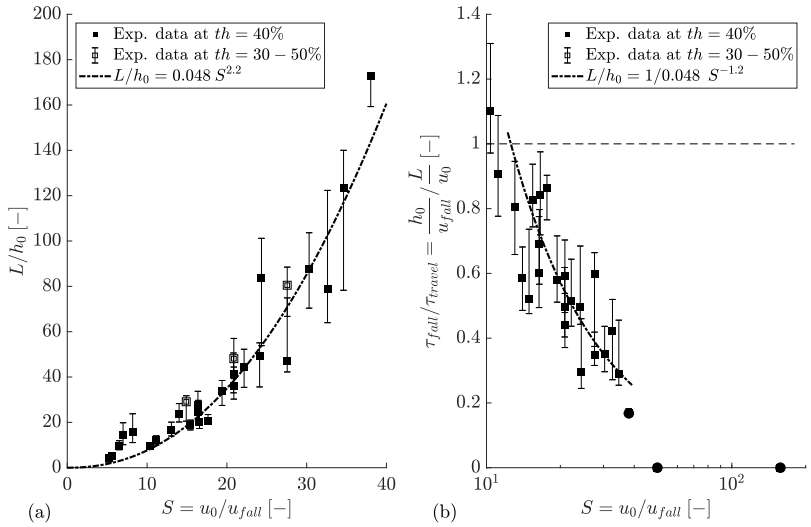

Fig. 6.5 (a) Plot of experimental run-out length of the gravity current, L, normalised by the initial height of the gravity current, h_0, as a function of $S = u_0/u_{fall}$. (b) Plot of the ratio of fall-time, $\tau_{fall} = h_0/u_{fall}$ and travel-time, $\tau_{travel} = L/u_0$ as a function of S. Circles correspond to experiments marked with (***). The dash-dotted line in both panels describes a power-law best-fit, defined in the legend.

$$\frac{\tau_{fall}}{\tau_{travel}} = \frac{S\, h_0}{L} = \frac{1}{a}\, S^{1-b}. \tag{6.5}$$

This best-fit has only been plotted over the range for which it has been validated experimentally (see panel (a)) and it is in good agreement with the experimental data.

6.5 Theoretical model

6.5.1 Initial conditions

The source fluxes of volume, momentum and buoyancy, Q_S, M_S and B_S issuing through the nozzle can be used to construct a source Froude number for the fountain,

$$Fr_s = \frac{(M_S/\pi)^{5/4}}{(Q_S/\pi)(B_S/\pi)^{1/2}} = \frac{u_S}{\sqrt{b_S g'_S}} \tag{6.6}$$

where u_S is the nozzle exit velocity of the mixture, $b_S = 4.3\,mm$ is the nozzle radius, and g'_S is the reduced gravity at the source (Hunt and Burridge, 2015). The source momentum flux is

$$M_s = Q_S u_S = \pi b_S^2 u_S^2 \tag{6.7}$$

and the source buoyancy flux is

$$B_s = Q_S g'_S = \pi b_S^2 u_S g'_S. \tag{6.8}$$

In our experiments, the terminal particle fall speed, u_{fall}, is small compared to the characteristic velocity of the fountain (cf. appendix of this chapter), so that the fountain behaves as an analogous single-phase fountain (Mingotti and Woods, 2016). We employ an empirical correlation developed through careful experiments by Burridge & Hunt (2016) to estimate the entrainment into the fountain based on the Froude number, leading to the estimate for the volume flux feeding the gravity current

$$Q_0 = Q_s(1 + 0.71 Fr_s). \tag{6.9}$$

In the appendix, we present a further set of experiments in which we measure the entrainment into the turbulent fountains analogous to those generated in our experiments. These additional experiments are conducted first in an unconfined environment, and second in a confined tank of width and depth 17 cm. These experiments confirm that the entrainment into the fountain is not hindered by the presence of the walls of the flume tank in the present experimental set-up, so that equation 6.9 serves as a good approximation for the initial volume flux of the gravity current. In the three experiments run with plume sources (marked with (**) in table 6.1), the classical solutions for turbulent plumes were employed to estimate the analogous flux (Morton et al., 1956). We assume that there is no particle settling within the area occupied by the fountain, owing to the much higher flow speed of the fountain as compared to the particle settling speed, so the buoyancy flux supplied to the gravity current from the fountain is assumed to equal the buoyancy flux supplied to the tank by the pump. The initial reduced gravity of the current is thus $g'_0 = g'_s Q_s / Q_0$, which is proportional to the volume fraction of particles. The reduced gravity of the current can be written as a function of the horizontal coordinate, x, in the form

$g'(x) = gC(x)(\rho_p - \rho_w)/\rho_w$, where $\rho_w = 1\,\mathrm{g/cm^3}$ and $\rho_p = 3.21\,\mathrm{g/cm^3}$ are the density of the water and the particles and g is the gravitational acceleration. With the initial volume flux given by equation 6.9, and the initial velocity taken as $u_0 = \sqrt{g'_0 h_0}$, the initial height of the current follows as $h_0 = q_0/u_0$. At this point, the Froude number of the flow, $Fr_0 = u_0/\sqrt{g'_0 h_0}$ has value 1 (Simpson, 1999; Ungarish, 2009). The initial fluxes of momentum and buoyancy per unit width are $q_0 u_0$ and $q_0 g'_0$. The particle fall speed, u_{fall}, corresponds to the Stokes' settling velocity,

$$u_{fall} = \frac{2}{9} g \frac{\rho_p - \rho_w}{\mu_W} \frac{d_P^2}{4} \tag{6.10}$$

where μ_W is the dynamic viscosity of water and d_P is the particle diameter, as listed in table 6.1.

6.5.2 Model of the steady particle-driven gravity current

Models for single-phase gravity currents, based on the original work of Von Karman (1940) and Benjamin (1968) usually consider vertically-averaged fluxes of volume, buoyancy and momentum and describe how these fluxes change in the along-flow direction (Huppert, 1998; Simpson, 1999; Ungarish, 2009). Following this approach, models for particle-driven gravity currents have been proposed by including a term for the reduction in buoyancy owing to the sedimentation of particles from the base of the flow (Bonnecaze et al., 1993; DeRooij, 1999; Huppert, 2006). We now build on this work to include the possibility of a sedimentation front on the upper surface of the current as suggested by our experimental observations (cf. figure 6.3). We assume the flow is well mixed and has depth h, speed u and buoyancy, g' (cf. Sher and Woods (2015); Ungarish (2009)).

In our experiments, the volume flux within the gravity current, $q = uh$, reduces from its initial value, q_0, to zero as the gravity current runs to the maximum distance $x = L$. The experimental data presented in figure 6.3 and 6.5 (b) suggest that this fluid is released as particles sediment from the top of the current. As $S = u_0/u_{fall}$ increases, our data suggests that the effective sedimentation speed at the top of the current, u_{front}, is reduced. We interpret this to be a result of the mixing near the interface between the current and

the ambient fluid, which suppresses the descent of the sedimentation front of particles. If we write $u_{front} = u_{fall} f(u(x)/u_{fall})$, then the change of volume flux in the horizontal direction is given by

$$\frac{d(h(x)u(x))}{dx} = -u_{fall}\, f\left(\frac{u(x)}{u_{fall}}\right). \tag{6.11}$$

For simplicity in this chapter we assume that

$$f\left(\frac{u(x)}{u_{fall}}\right) = 1 - \epsilon u(x)/u_{fall} \qquad for \qquad u_{fall} > \epsilon u(x), \tag{6.12}$$

and aim to determine the constant ϵ from our data. We note that in our experimental study we have not observed gravity currents in which the volume flux increases from the source, so the above expression has only been validated for $u_{fall} > \epsilon u(x)$. However, we note that as u/u_{fall} increases, a further complication emerges because the Shields number of the flow increases and eventually reaches the threshold at which particles in the bed may become resuspended (cf. Eames et al. (2001)), a process which is beyond the scope of the present study.

The particle flux continually decreases as particles sediment. The sedimentation of particles occurs in a viscous boundary layer close to the base of the tank and is proportional to the local particle concentration (cf. Bonnecaze et al. (1993)),

$$\frac{d(C(x)h(x)u(x))}{dx} = -u_{fall}C(x). \tag{6.13}$$

Combining this with equation 6.11, we find that the particle concentration decreases with distance according to the relation

$$\frac{dC(x)}{dx} = -\frac{\epsilon C(x)}{h(x)}. \tag{6.14}$$

The rate of change of momentum flux in the longitudinal direction is due to both the change in depth of the gravity current and the reduction in particle load

$$\frac{d(u^2h)}{dx} = -g'h\frac{dh}{dx} - h^2\frac{dg'}{dx} + u\frac{d(uh)}{dx}. \tag{6.15}$$

The term $u\frac{d(uh)}{dx}$ corresponds to the momentum carried by the liquid leaving the gravity current as particles sediment from the upper surface of the gravity

current. We can combine the above equations to determine the rate of change of velocity in the current,

$$\frac{du(x)}{dx} = \frac{g'(x)u_{fall}}{u(x)^2 - g'(x)h(x)}. \tag{6.16}$$

For $u_0^2 > g_0'h_0$, the flow is super-critical and equation 6.11 suggests that the liquid in the gravity current accelerates and the depth of the flow reduces with distance from the source. For $u_0^2 < g_0'h_0$, the flow is sub-critical and in that case, the liquid in the gravity current decelerates, leading to an increase in depth with distance from the source. Our experimental findings (cf. figure 6.2 - 6.5) suggest that the flow is critical at the fountain and follows the super-critical branch, as expected from classical hydraulics (Long, 1954). For evaluating the model predictions we choose the initial velocity to be just supercritical, $u_0 = 1.001\sqrt{g_0'h_0}$. We have found that the model predictions are insensitive to the exact magnitude of the positive perturbation as long as it is much smaller than 1. We can write the above equations in dimensionless form by normalising with q_0 and g_0', resulting in the dimensionless variables and initial conditions

$$\hat{q} = \frac{q}{q_0} \qquad \hat{g'} = \frac{g'}{g_0'} \qquad \hat{x} = \frac{x}{q_0^{2/3} g_0'^{-1/3}} \qquad \hat{u} = \frac{u}{(q_0 g_0')^{1/3}} \qquad \hat{u}(0) = 1.001. \tag{6.17}$$

This leads to the set of dimensionless equations

$$\frac{d\hat{q}}{d\hat{x}} = -\frac{1}{S} + \epsilon\hat{u}, \qquad \frac{d\hat{g'}}{d\hat{x}} = -\frac{\epsilon\hat{g'}}{\hat{h}}, \qquad \frac{d\hat{u}}{d\hat{x}} = \frac{\hat{g'}/S}{\hat{u^2} - \hat{g'}\hat{h}}. \tag{6.18}$$

It is worth repeating that the equations in equation 6.18 are only valid for $S < 1/\epsilon$. In figure 6.6 (a) - (d) we show the predictions of the dimensionless model for the volume flux, depth, reduced gravity and velocity as a function of dimensionless distance from the source. The four lines in each panel correspond to the four values for S given in panel (d). We note that the run-out length increases for larger values of S. Owing to a short run-out length, the plots for $S = 1$ are barely visible in this figure. For a more detailed view of this, please refer to figure 6.7 in which the horizontal distances are normalised by the total run-out length. In figure 6.6 (a) we see that the volume flux decreases approximately linearly with distance from the source. The profiles of gravity current height as a function of distance from the source, shown in panel (b),

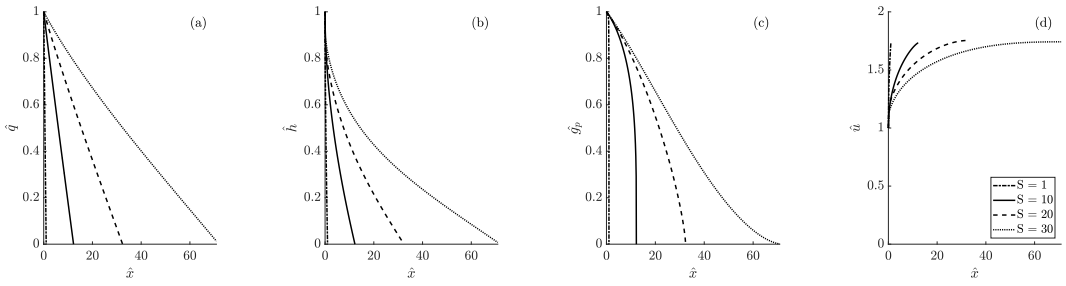

Fig. 6.6 Variation of the dimensionless volume flux (a), depth (b), reduced gravity (c), and velocity (d) of the current as a function of dimensionless distance from the source. The dot-dashed line was obtained for $S = 1$, the solid line for $S = 10$, the dashed line for $S = 20$, and the dotted line for $S = 30$. These model predictions were obtained for the best-fit mixing parameter $\epsilon = 0.012$.

highlight that the height of the gravity current decreases rapidly close to the origin of the current. The plot of reduced gravitational acceleration within the current, as a function of distance from the source (panel (c)), shows that the particle load within the current transitions towards an asymptotic shape as the parameter S increases. For small values of S, the particle load reduces more abruptly towards the end of the gravity current. The velocity within the gravity current is plotted as a function of horizontal distance in panel (d). The model prediction presented in this panel indicates that the flow accelerates close to the origin of the gravity current and then converges to a more uniform speed.

The four panels in figure 6.7 correspond to the four panels shown in figure 6.6, with the horizontal axis normalised by the total run-out distance, x/L, to allow for a qualitative comparison of the four quantities. We note that with this choice of normalisation, the profiles of volume flux (a), current height (b), and velocity (d) are similar over the entire range $1 < S < 30$. The reduced gravity of the current, plotted as a function of the dimensionless distance from the source in panel (c), however, depends strongly on the value of S. For small values of S, corresponding to small fall speeds, the particle load remains high over most of the length of the gravity current, before abruptly decreasing as the current reaches the final run-out distance. We note, however, that this rapid reduction in height occurs in a region where the height of the gravity current has become vanishingly small. At this stage, the dynamics of the current may be much more strongly affected by the bottom boundary layer, although such effects are not captured by the present model. As S increases, the particle load

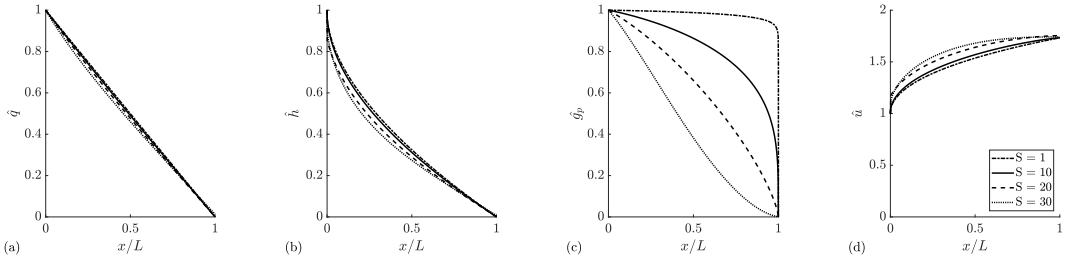

Fig. 6.7 Variation of the dimensionless volume flux (a), depth (b), reduced gravity (c), and velocity (d) of the current as a function of the dimensionless distance x/L from the source. The dot-dashed line was obtained for $S = 1$, the solid line for $S = 10$, the dashed line for $S = 20$, and the dotted line for $S = 30$. These model predictions were obtained for the best-fit mixing parameter $\epsilon = 0.012$.

decreases more rapidly near the origin of the gravity current. This is consistent with our previous observation that the entrainment of ambient fluid becomes increasingly important for larger values of S (cf. figure 6.5 (b)). We note that the reduced gravitational acceleration of the current decreases approximately linearly for $S = 26$.

We compared the experimental data for all the currents with the model predictions to determine the best-fit value for the settling coefficient, $\epsilon = 0.012 \pm 0.002$ (equation 6.11, 6.12). This investigation is shown in figure 6.8. In panel (a) we compare the model prediction for the area occupied by the gravity current on the x-axis as a function of the experimentally measured area on the y-axis. The dashed line with unit slope illustrates the ideal line of exact agreement. We find that the model predictions are in good agreement with the experimental data. Panel (b) shows a plot of dimensionless run-out length, L/h_0, as a function of S. The three black lines were obtained for $\epsilon = 0.012 \pm 0.002$. We note that the model predictions are insensitive to the choice of ϵ for small values of S. This corresponds to the experiments in which the ratio of initial current velocity, u_0, and particle fall speed, u_{fall}, is less than 20. The red line illustrates that the predicted run-out lengths of the gravity currents decrease well below the experimental observations if we do not account for the reduced effective settling speed ($\epsilon = 0$). Again, we find a good agreement between experimental data and model prediction for $\epsilon = 0.012$.

In the present experimental investigation we did not observe gravity currents for which the height of the gravity current increases with distance from the source. However, our model, especially equation 6.12, predicts an increase

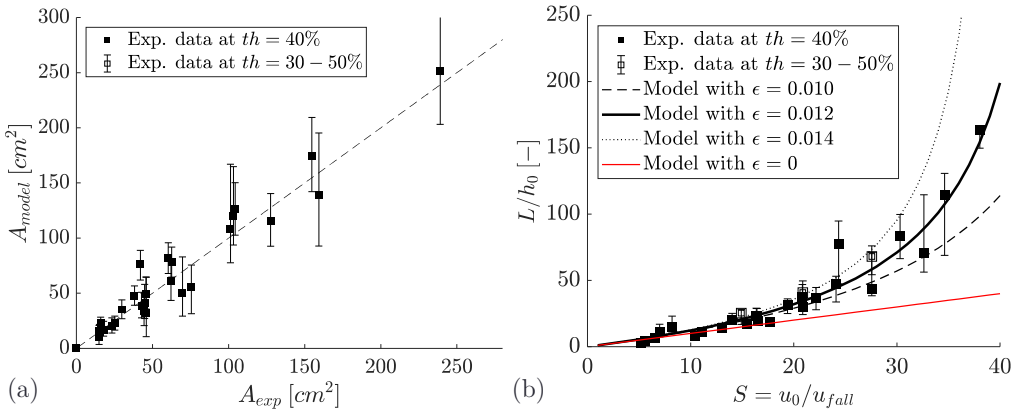

Fig. 6.8 (a) Area occupied by the gravity current plotted as a function of the model prediction of the occupied area. (b) Plot of dimensionless run-out length of the particle-laden gravity current as a function of S. The lines illustrate the model prediction for $\epsilon = 0.012 \pm 0.002$. Squares represent fountain sources, circles represent plume sources. The red line denotes the model predictions for $\epsilon = 0$.

in volume flux for $u_{fall} < \epsilon u(x)$. Since we cannot confirm such an increase in volume flux experimentally, we can only confirm the validity of our model for the regime $u_{fall} > \epsilon u(x)$. This condition is met for $S < 1/\epsilon \approx 83$ with $\epsilon = 0.012$. It is worth noting that, for $S > 80$, the large difference between current velocity and particle fall speed is likely to lead to a resuspension of particles and this additional effect would also need to be built into the model (Eames et al., 2001). Owing to the reflection of the flow from the rear wall of the tank, however, it is not possible to investigate any resuspension effects with the present experimental set-up.

The above model is based on the experimental observation that the release of source liquid into the environment is controlled by a balance of particle settling owing to the particle fall speed, u_{fall}, and some re-entrainment of this released fluid, quantified by the parameter ϵ (equation 6.12). For this mixing to occur we require the local Richardson number,

$$Ri(x) = \frac{g'(x)h(x)}{u(x)^2}, \tag{6.19}$$

to be small. We can compute this ratio as predicted by our model and we find that the local Richardson number in the gravity current does decrease from the initial value of one. Within the first 10% of the total length of the gravity

currents presented in the current study, the Richardson number falls below 0.5, and within the first 30% percent of the total length of the gravity currents the Richardson number falls below 0.25, indicating that the currents are capable of re-entraining some of the released fluid.

6.6 Summary

We have studied the dynamics of steady particle-laden gravity currents. We presented a new set of experiments, complemented by a model for the conservation of volume, momentum and buoyancy fluxes. Our findings bridge the gap between settling columns experiments ($S < 10$), in which sedimentation fronts are observed, and studies of particle-driven gravity currents ($S > 40$) with no sedimentation fronts. In our intermediate regime, we observe particle-driven gravity currents which reduce in height with distance from the source and we observe a release of liquid from the current into the ambient, revealing the presence of a sedimentation front in particle-driven gravity currents for $10 < S < 40$. Mixing near the top of the current reduces the speed of the sedimentation front to values below that of the fall speed of the particles. We model this reduction in fall speed with the relation $f(u/u_{fall}) = 1 - \epsilon u/u_{fall}$, where $\epsilon = 0.012 \pm 0.002$.

As S increases, we expect the Shields parameter of the current to increase beyond a critical value for which we suspect that the re-suspension of particles from the bed becomes increasingly important, thereby changing the dynamics of the flow (cf. Eames et al. (2001)), and it would be interesting to include such effects in future work as well as to investigate the effects of multiple particle sizes.

A regime diagram of our experimental investigation is shown in figure 6.9. The range of $5 < S < 40$ is characteristic for flows in separators and water

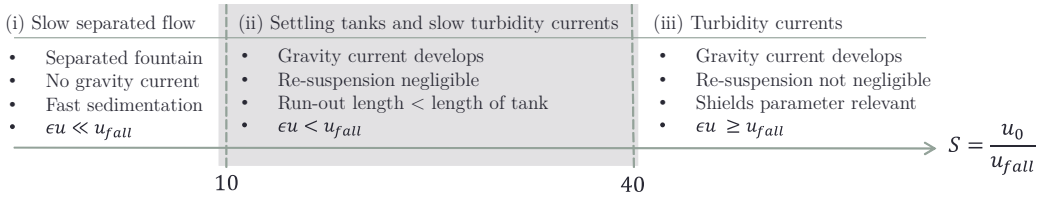

Fig. 6.9 Regime diagram: The grey area illustrates the range in S for which our model has been validated against experimental data.

treatment facilities and some slow turbidity currents, in which sedimentation fronts develop (DeRooij, 1999). Particle sizes in these applications range from 10 to 100 μm and flow speeds are of the order of cm/s. For turbidity currents, flow speeds can be substantially larger, leading to much larger values of S. Previous studies modelling the dynamics of turbidity currents have reported observations that the height of such currents remains constant with distance from the source (Bonnecaze et al., 1993; Huppert, 2006). We interpret this to be a result of the mixing within the flow suppressing the development of a sedimentation front.

6.7 Appendix: investigation of the source condition

In the present experimental investigation, the particle-driven gravity current is fed by a continuous particle-laden fountain. A top-view of the transition of the flow from a particle-laden fountain to a particle-driven gravity current is shown in figure 6.10 for exp. 6 as an example. The fountain is shown to the left, illuminated by the light sheet at the bottom of the image. The dashed line marks the position of the onset of the gravity current where $Fr_0 = 1$. The flow appears to transition rapidly from the axisymmetric fountain flow to a near parallel channel flow as it spreads downstream. The distance from the centre of the fountain to the onset of the gravity current where $Fr_0 = 1$ is the adjustment length, L_{adj} (cf. schematic in figure 6.1).

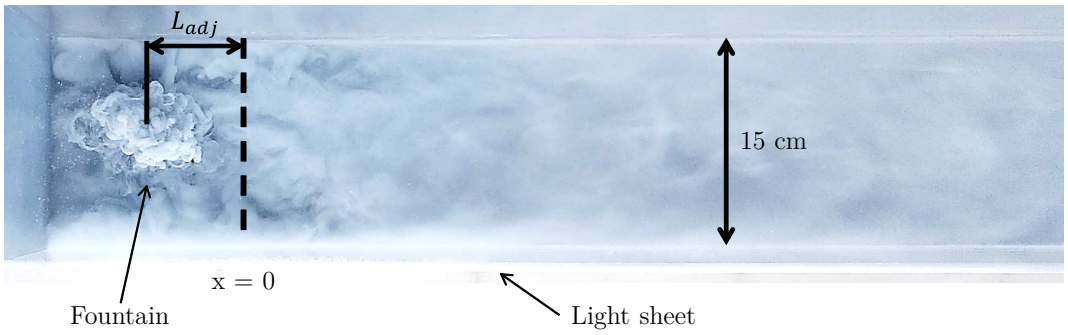

Fig. 6.10 Top view of the transition of the flow from a turbulent particle-laden fountain to a particle-driven gravity current. The image was taken for exp. 6 in table 6.1. The dashed line marks the onset of the gravity current.

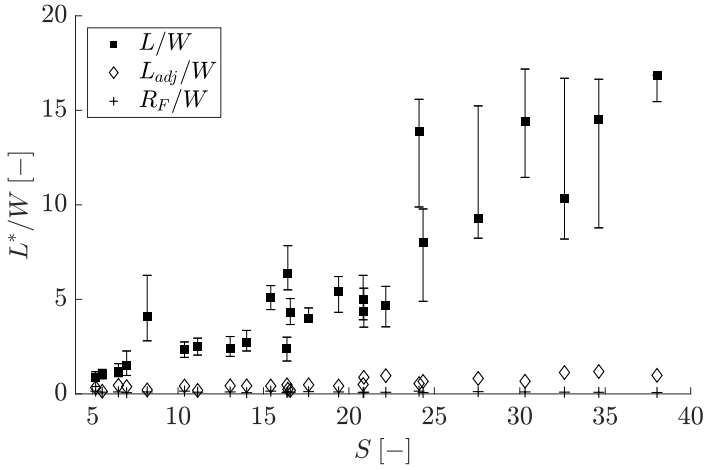

Fig. 6.11 Comparison of gravity current run-out length, L (black squares), adjustment length, L_{adj} (diamonds), and fountain radius, R_F (crosses), all non-dimensionalised by the width of the tank, W, plotted as a function of the settling parameter S. The length scale over which the particles sediment from the gravity current far exceeds the length scale of the adjustment zone of the gravity current for $S > 10$.

In figure 6.11 we show a comparison of the gravity current run-out length, L, the adjustment length over which the flow transitions from a fountain to a gravity current, L_{adj}, and the fountain radius, R_F, based on the source Froude number, Fr_S (cf. Mizushina et al. (1982)). All three lengths are normalised by the width of the tank, W. The ratio of fountain radius and tank width, R_F/W, shown as crosses, is always less than one. The ratio of the adjustment length and tank width, L_{adj}/W, shown as diamonds, is of order one. The dimensionless run-out length, shown as black squares, far exceeds both these length scales for $S > 10$, indicating that the distance over which particles sediment from the gravity current far exceeds the distance required for the flow to transition from a turbulent fountain to a gravity current. This suggests that the investigation presented in the main body is insensitive to the exact value of the adjustment length.

Mingotti & Woods (2016) have shown that particle-laden fountains behave like analogous single-phase fountain with the same source fluxes of buoyancy and momentum if the particle fall speed, u_{fall}, is small compared to the characteristic fountain velocity,

$$u_F = B_S^{1/2} M_S^{-1/4}. \tag{6.20}$$

For the present experiments, this ratio is in the range $0.006 < u_{fall}/u_F < 0.2$.

Mizushina et al. (1982) have shown that the diameter of a turbulent fountain corresponds to

$$d_F = 0.34 H_{SPF} \tag{6.21}$$

where H_{SPF}, the steady-state height reached by a single-phase fountain with a source momentum flux M_S and a source buoyancy flux B_S, is

$$H_{SPF} = 1.84\, M_S^{3/4} |B_S^{-1/2}|. \tag{6.22}$$

From this empirical relation we can estimate that the ratio of the fountain diameter, d_F, to the width of the tank (15 cm), ranges between 12.8% and 29.1%, indicating that the fountain is likely to behave like an equivalent fountain in an unrestricted environment. In the experiments run with a double fountain source the maximum fountain radius does not exceed 2 cm so that both the wall effects and the presence of the adjacent fountain are negligible.

To further test the validity of equation 6.9 for the present investigation, we directly measured the volume flux entrained by a fountain in a large environment, and then again in a restricted environment of width and depth 17 cm. A schematic of this experimental investigation is shown in figure 6.12. In panel (a) we show how the total volume flux entrained into a single-phase fountain is measured in a large tank of width and depth 45 cm. This investigation follows the process employed by Burridge & Hunt (2016). The fountain source is elevated and the dense fountain liquid accumulates at the bottom of the tank. In the absence of any ventilation, this dense layer would increase in height as a filling-box. By removing fluid from this dense bottom layer, we can control the position of the interface. When adjusting this extraction flow rate such that the interface is fixed at the exact height of the nozzle, the extraction flow rate corresponds to the sum of source volume flux injected through the nozzle, Q_S, and the total entrained volume flux above the interface, Q_E. The 45 by 45 cm tank is placed inside a much larger tank of dimensions 150 by 80 by 100 cm, in which the water level is kept fixed, so that fresh water is continuously supplied to the fountain. In panel (b) we show how we measure the volume flux entrained into the fountain in a confined environment. We repeat the exact process outlined above, only this time we place a 17 by 17 cm square Perspex section around the fountain before measuring the ventilation flow rate, $Q_S + Q_E$. We ran these experiments for 6 combinations of source fluxes of

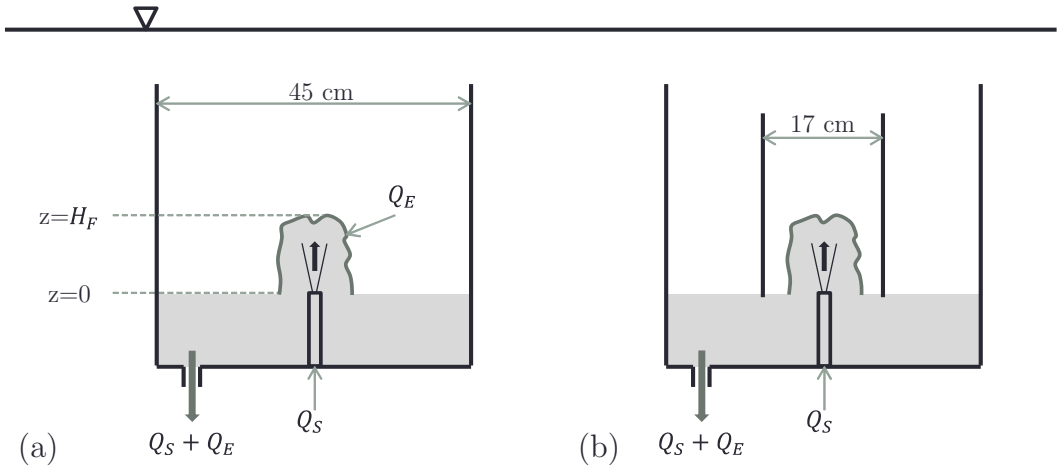

Fig. 6.12 Schematic of the experimental set-up to measure the total entrainment into a turbulent single-phase fountain. First (a), we measure the entrainment into such a fountain in a large environment of width and depth 45 cm. Second (b), we place a square perspex section of width and depth 17 cm around the fountain and repeat the entrainment measurement.

buoyancy and momentum, listed in table 6.2. These source fluxes correspond to the source fluxes in table 6.1 and the nozzle is the same nozzle with internal radius of 4.3 mm as employed in the investigations detailed in the main body of the chapter.

In figure 6.13 we plot the sum of the measured entrained volume flux into the fountain and the source flux through the nozzle, $Q_E + Q_S$, normalised by the prediction of the empirical relation for single-phase fountains in an unrestricted environment (equation 6.9), as a function of the source Froude

Exp.	Q_S $[ml/s]$	g'_S $[m/s^2]$	M_S $[m^4/s^2]$	B_S $[m^4/s^3]$	Fr_S $[-]$	H_{SPF} $[cm]$	Q_{SPF} $[ml/s]$	Q_{45} $[ml/s]$	Q_{17} $[ml/s]$
Q1	17	0.134	4.9e-6	2.3e-6	12	12.8	163	185	185
Q2	17	0.201	4.9e-6	3.4e-6	10	10.5	136	143	134
Q3	17	0.267	4.9e-6	4.5e-6	9	9.1	121	118	116
Q4	17	0.333	4.9e-6	5.6e-6	8	8.2	110	115	111
Q5	17	0.398	4.9e-6	6.7e-6	7	7.5	102	117	127
Q6	17	0.527	4.9e-6	8.9e-6	6	6.5	91	112	112

Table 6.2 Table with source conditions: Number of the experiment (Exp.), source volume flux (Q_S), reduced gravitational acceleration at the source ($g_S{}'$), source momentum flux (M_S), source buoyancy flux (B_S), source Froude number (Fr_S), single-phase fountain height (H_{SPF}), expected total flux according to equation 6.9 (Q_{SPF}), measured total volume flux in the 45 by 45 cm tank (Q_{45}), and measured total volume flux in the 17 by 17 cm section (Q_{17}).

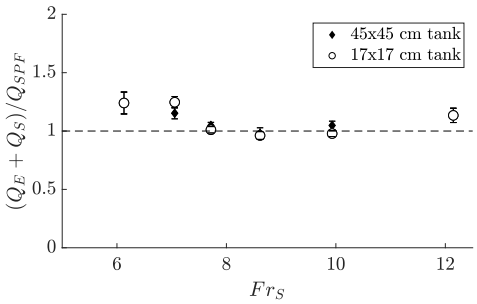

Fig. 6.13 Plot of the ratio of measured total volume flux of the down-flow from a turbulent fountain and the expected volume flux of a single-phase fountain in an unrestricted environment (see equation 6.9), as a function of the source Froude number, Fr_S.

number, Fr_S. The black diamonds correspond to the volume flux measurements in the unrestricted environment (45 by 45 cm tank) and the circles correspond to the volume flux measurements recorded for a fountain in the 17 by 17 cm confinement (cf. figure 6.12 (b)). The experimental data are in good agreement with the empirical relation of equation 6.9, represented as the dashed horizontal line. This indicates that equation 6.9 is likely to be a reasonable approximation of the volume flux from the fountain into the gravity current.

Chapter 7

Conclusion, discussion and further work

7.1 Summary and discussion

In this thesis we presented five chapters containing experimental studies on bubble-laden and particle-laden axisymmetric fountains, complemented by theoretical models.

In chapters 2 and 3, we considered unconfined bubble fountains. In chapters 4 and 5 we focused our attention on turbulent fountains in confined environments, and in chapter 6 we investigated the dynamics of particle-driven gravity currents, fed by a particle-laden fountain.

Chapter 2 considered unconfined turbulent bubble fountains in water. We investigated the maximum penetration depth of bubbles carried into a reservoir by submerged and plunging water jets. We found that the maximum depth reached by turbulent bubble fountains depends on the source Froude number of the fountain, as well as the ratio of terminal bubble rise speed and characteristic fountain velocity. This dependency is correctly captured by a novel theoretical model, based on a single entrainment coefficient. We showed that our model can be used to estimate the gas flux entrained by plunging liquid jets.

Chapters 3 contains an experimental study on the depth reached by bubbles in unconfined low Reynolds number bubble fountains. The viscosity of the working fluid, oil, was 55 times larger compared to water, resulting in laminar flow. We presented a qualitative comparison of unconfined high and low

Reynolds number bubble fountains. We found that the experimental data for the rise height of the laminar oil-air fountains agrees with scalings developed for single-phase fountains with low source Reynolds numbers and high source Froude numbers.

Our experimental videos revealed that some of the small bubbles accumulate at the free surface and form a bubble-rich layer growing downwards into the tank. Light attenuation techniques and time-series images allowed us to measure the velocities of these fronts and hypothesize that the filling-box speed of these layers depends on the background flow velocity and the terminal rise speed of the bubbles. This observation motivated a detailed investigation of the transport of mono-dispersed contaminants carried by multiphase fountains into confined environments, presented in chapter 4.

In chapter 4 we investigated the transport of particles carried into a confined space by a turbulent particle fountain. Owing to the confinement, a background volume flux developed in the area around and above the fountain. By comparing the terminal particle fall speed with the three characteristic velocities in the system, we identified four distinct regimes which determine the fate of the particles: (i) The particles separate from the fountain liquid at some fraction of the total fountain height and quickly settle on the base of the tank. (ii) The multiphase fountain behaves like an analogous single-phase fountain, but all particles settle on the base of the tank. (iii) The background flux is strong enough to suspend a layer of particles up to some fraction of the total fountain height. (iv) The background flux is strong enough to lift particles above the top of the fountain and the particles contaminate the entire tank.

In chapter 5 we investigated extremely confined turbulent single-phase fountains by systematically varying the confinement ratio, i.e. the ratio of the width of the confinement and the diameter of an equivalent unconfined fountain. We found that both the rise height and the entrainment of the fountain remain unaffected by the presence of the wall if the value of the confinement ratio is greater than 2. For smaller values of the confinement ratio we presented a scaling argument for the total fountain entrainment, which is in accord with the experimental data.

In chapter 6 we investigated particle-driven gravity currents, fed by a continuous particle-laden fountain. We identified the ratio of terminal particle settling velocity and initial current velocity as a critical parameter controlling

the dynamics of the multiphase current. Dye experiments revealed the presence of a sedimentation front such that source fluid emerged above the top of the gravity current as particles sedimented on the base of the tank. Our model, based on a single re-entrainment parameter, describes the shape and run-out distance of these particle-driven gravity currents. With this investigation we bridge the gap between settling column experiments, in which settling fronts have been observed, and experiments on turbidity currents, which maintain a constant height until they lose their particle load.

7.2 Conclusion

In this thesis we presented results advancing our understanding of the rise height and entrainment of axisymmetric multiphase fountains with large source Froude numbers ($Fr_0 > 1$). We considered fountains with high and low source Reynolds numbers in confined and unconfined environments. Five experimental studies employing light attenuation, dye visualisation, and time-series imaging techniques allowed for insights into the motion of fluid and contaminants. The theoretical models presented in this thesis quantify our improved understanding of these fundamental flows.

The research presented in this thesis is of industrial relevance as it contributes to increasing the efficiency and effectiveness of ventilation systems, aeration systems, water treatment plants and process equipments such as separators, particle filters and fluidised bed reactors.

The work presented in this thesis further allows for novel insights into multiphase flows occurring in nature, such as particle transport in volcanic eruptions and turbidity currents.

7.3 Opportunities for further work

In the experimental study on low Reynolds number bubbles fountains in chapter 3 we observed a large range of bubble sizes with very different rise speeds. It would be of interest to expand the theoretical models presented in chapters 2, 4 and 6 to account for multiple particle or bubble sizes, as most practical applications would feature contaminants with a range of sizes or weights.

In many applications such as separators or fluidised bed reactors, multiple fountains are placed in close proximity to each other. Experimental studies on the interaction of multiple multiphase fountains in confined and unconfined spaces present promising avenues of further research.

Low Reynolds number bubble fountains are frequently observed in the oil sumps of internal combustion engines. We have conducted initial experiments on the motion of bubbles in model engine sumps. These sumps typically have a shallow and a deep section. In the shallow section, the fountain impinges on the floor of the tank and feeds a gravity current contaminating the oil reservoir. Owing to the circulation of oil, the background flow field in these tanks is very strong, drawing bubbles towards the extraction vent. It would be of interest to model the flow in such systems, both for individual fountains, as well as for multiple fountains.

Multiphase fountains are featured in a wide range of commercial applications. Experimental studies and the development of scalings and theoretical models on both high and low Reynolds number multiphase fountains present a whole suite of further scientific challenges of industrial relevance.

References

Ansong, J. K., Kyba, P. J., and Sutherland, B. R. (2008). Fountains impinging on a density interface. *Journal of Fluid Mechanics*, 595:115–139.

Baines, W. D., Corriveau, A. F., and Reedman, T. J. (1993). Turbulent fountains in a closed chamber. *Journal of Fluid Mechanics*, 255:621–646.

Baines, W. D. and Turner, J. S. (1969). Turbulent buoyant convection from a source in a confined region. *Journal of Fluid mechanics*, 37:51–80.

Baines, W. D., Turner, J. S., and Campbell, I. H. (1990). Turbulent fountains in an open chamber. *Journal of Fluid Mechanics*, 212:557–592.

Baran, B. A. (2007). *Engine lubrication oil aeration*. PhD thesis, Massachusetts Institute of Technology.

Benjamin, T. B. (1968). Gravity currents and related phenomena. *Journal of Fluid Mechanics*, 31:209–248.

Biń, A. (1993). Gas entrainment by plunging liquid jets. *Chemical Engineering Science*, 48:3585–3630.

Blanchette, F. and Bush, J. W. M. (2005). Particle concentration evolution and sedimentation-induced instabilities in a stably stratified environment. *Physics of Fluids*, 17:073302.

Bloomfield, L. J. and Kerr, R. C. (1999). Turbulent fountains in a confined stratified environment. *Journal of Fluid Mechanics*, 389:27–54.

Bloomfield, L. J. and Kerr, R. C. (2000). A theoretical model of a turbulent fountain. *Journal of Fluid Mechanics*, 424:197–216.

Bonnecaze, R. T., Huppert, H. E., and Lister, J. R. (1993). Particle-driven gravity currents. *Journal of Fluid Mechanics*, 250:339–369.

Burridge, H. C. and Hunt, G. R. (2012). The rise heights of low- and high-Froude-number turbulent axisymmetric fountains. *Journal of fluid mechanics*, 691:392–416.

Burridge, H. C. and Hunt, G. R. (2013). The rhythm of fountains: the length and time scales of rise height fluctuations at low and high Froude numbers. *Journal of Fluid Mechanics*, 728:91–119.

Burridge, H. C. and Hunt, G. R. (2016). Entrainment by turbulent fountains. *Journal of Fluid Mechanics*, 790:407–418.

Burridge, H. C., Mistry, A., and Hunt, G. R. (2015). The effect of source Reynolds number on the rise height of a fountain. *Physics of Fluids*, 27:047101.

Carazzo, G., Kaminski, E., and Tait, S. (2010). The rise and fall of turbulent fountains: a new model for improved quantitative predictions. *Journal of Fluid Mechanics*, 657:265–284.

Cardoso, S. S. S. and Woods, A. W. (1995). On convection and mixing driven by sedimentation. *Journal of Fluid Mechanics*, 285:165–180.

Clanet, C. and Lasheras, J. C. (1997). Depth of penetration of bubbles entrained by a plunging water jet. *Physics of Fluids*, 9:1864–1866.

Clift, R., Grace, J. R., and Weber, M. E. (2005). *Bubbles, drops, and particles*. Courier Corporation.

Davis, R. H. and Acrivos, A. (1985). Sedimentation of noncolloidal particles at low Reynolds numbers. *Annual Review of Fluid Mechanics*, 17:91–118.

DeRooij, F. (1999). *Sedimenting particle-laden flows in confined geometries*. PhD thesis, University of Cambridge.

Eames, I., Hogg, A. J., Gething, S., and Dalziel, S. B. (2001). Resuspension by saline and particle-driven gravity currents. *Journal of Geophysical Research: Oceans*, 106:14095–14111.

Guazzelli, E. and Hinch, J. (2011). Fluctuations and instability in sedimentation. *Annual review of fluid mechanics*, 43:97–116.

Haberman, W. L. and Morton, R. K. (1953). An experimental investigation of the drag and shape of air bubbles rising in various liquids. *Defense Technical Information Center*.

Hoyal, D. C. J. D., Bursik, M. I., and Atkinson, J. F. (1999). The influence of diffusive convection on sedimentation from buoyant plumes. *Marine Geology*, 159:205–220.

Hunt, G. R. and Burridge, H. C. (2015). Fountains in industry and nature. *Annual Review of Fluid Mechanics*, 47:195–220.

Huppert, H. E. (1998). Quantitative modelling of granular suspension flows. *Philosophical Transactions of the Royal Society of London*, 356:2471–2496.

Huppert, H. E. (2006). Gravity currents: a personal perspective. *Journal of Fluid Mechanics*, 554:299–322.

Kaminski, E., Tait, S., and Carazzo, G. (2005). Turbulent entrainment in jets with arbitrary buoyancy. *Journal of Fluid Mechanics*, 526:361–376.

Kynch, G. J. (1952). A theory of sedimentation. *Transactions of the Faraday society*, 48:166–176.

Lin, Y. P. and Linden, P. F. (2005). A model for an under floor air distribution system. *Energy and Buildings*, 37:399–409.

Linden, P. F. (1999). The fluid mechanics of natural ventilation. *Annual review of fluid mechanics*, 31:201–238.

List, E. J. (1982). Turbulent jets and plumes. *Annual review of fluid mechanics*, 14:189–212.

Long, R. R. (1954). Some aspects of the flow of stratified fluids: II. experiments with a two-fluid system. *Tellus*, 6:97–115.

McDougall, T. J. (1978). Bubble plumes in stratified environments. *Journal of Fluid Mechanics*, 85:655–672.

McDougall, T. J. (1981). Negatively buoyant vertical jets. *Tellus*, 33:313–320.

Middleton, G. V. (1993). Sediment deposition from turbidity currents. *Annual review of earth and planetary sciences*, 21:89–114.

Mingotti, N. and Woods, A. W. (2015a). On the transport of heavy particles through a downward displacement-ventilated space. *Journal of Fluid Mechanics*, 774:192–223.

Mingotti, N. and Woods, A. W. (2015b). On the transport of heavy particles through an upward displacement-ventilated space. *Journal of Fluid Mechanics*, 772:478–507.

Mingotti, N. and Woods, A. W. (2016). On turbulent particle fountains. *Journal of Fluid Mechanics*, 793:R1.

Mizushina, T., Ogino, F., Takeuchi, H., and Ikawa, H. (1982). An experimental study of vertical turbulent jet with negative buoyancy. *Wärme- und Stoffübertragung*, 16:15–21.

Morton, B. R., Taylor, G., and Turner, J. S. (1956). Turbulent gravitational convection from maintained and instantaneous sources. *Proceedings of the Royal Society of London. Series A. Mathematical and Physical Sciences*, 234:1–23.

Nemoto, S., Kawata, K., Kuribayashii, T., Akiyama, K., Kawai, H., and Murakawai, H. (1997). A study of engine oil aeration. *JSAE review*, 18:271–276.

Neto, I. E. L., Cardoso, S. S. S., and Woods, A. W. (2016). On mixing a density interface by a bubble plume. *Journal of Fluid Mechanics*, 802:R3.

Ohkawa, A., Kusabiraki, D., Kawai, Y., Sakai, N., and Endoh, K. (1986). Some flow characteristics of a vertical liquid jet system having downcomers. *Chemical Engineering Science*, 41:2347–2361.

Rowe, P. N. and Nienow, A. W. (1976). Particle mixing and segregation in gas fluidised beds. A review. *Powder Technology*, 15:141–147.

Schlichting, H. (1979). *Boundary-layer theory*. McGraw-Hill.

Sher, D. and Woods, A. W. (2015). Gravity currents: entrainment, stratification and self-similarity. *Journal of Fluid Mechanics*, 784:130–162.

Sher, D. and Woods, A. W. (2017). Mixing in continuous gravity currents. *Journal of Fluid Mechanics*, 818.

Simpson, J. E. (1999). *Gravity currents: In the environment and the laboratory*. Cambridge University Press.

Steel, E., Buttles, J., Simms, A. R., Mohrig, D., and Meiburg, E. (2017). The role of buoyancy reversal in turbidite deposition and submarine fan geometry. *Geology*, 45:35–38.

Steel, E., Simms, A. R., Warrick, J., and Yokoyama, Y. (2016). Highstand shelf fans: The role of buoyancy reversal in the deposition of a new type of shelf sand body. *Bulletin*, 128:1717–1724.

Turner, J. S. (1966). Jets and plumes with negative or reversing buoyancy. *Journal of Fluid Mechanics*, 26:779–792.

Turton, R. and Levenspiel, O. (1986). A short note on the drag correlation for spheres. *Powder Technology*, 47:83–86.

Ungarish, M. (2009). *An introduction to gravity currents and intrusions*. Chapman and Hall.

Van de Donk, J. A. C. (1981). *Water aeration with plunging jets*. Delft University of Technology.

Von Karman, T. et al. (1940). The engineer grapples with nonlinear problems. *Bulletin of the American Mathematical Society*, 46:615–683.

Williamson, N., Srinarayana, N., Armfield, S. W., McBain, G. D., and Lin, W. (2008). Low-Reynolds-number fountain behaviour. *Journal of Fluid Mechanics*, 608:297–317.

Woods, A. W. (1995). The dynamics of explosive volcanic eruptions. *Reviews of Geophysics*, 33:495–530.

Woods, A. W. (2010). Turbulent plumes in nature. *Annual Review of Fluid Mechanics*, 42:391–412.